

Design and Characterization of Resonant Cavity Light-Emitting Diode

THESIS

Thomas M. Fitzgerald  
Captain, USAF

AFIT/GEQ/ENG/94D-02

**WORKING PAPER SERIES**  
**DEPARTMENT OF OPERATIONAL SCIENCES**

DEPARTMENT OF THE AIR FORCE  
**AIR UNIVERSITY**

**AIR FORCE INSTITUTE OF TECHNOLOGY**

SCHOOL OF ENGINEERING  
Wright-Patterson Air Force Base, Ohio

**DISTRIBUTION STATEMENT 4**

Approved for public release  
Distribution Unlimited

19941228 085

AFIT/GEO/ENG/94D-02

<b>Accession For</b>	
NTIS GRA&I	<input checked="checked" type="checkbox"/>
DTIC TAB	<input type="checkbox"/>
Unannounced	<input type="checkbox"/>
Justification	
By	
Distribution/	
Availability Codes	
Dist	Avail and/or Special
A-1	

Design and Characterization of Resonant Cavity Light-Emitting Diodes

THESIS

Thomas M. Fitzgerald  
Captain, USAF

AFIT/GEO/ENG/94D-02

DTIC QUALITY INSPECTED 2

Approved for public release; distribution unlimited

AFIT/GEO/ENG/94D-02

Design and Characterization of Resonant Cavity Light-Emitting Diodes

THESIS

Presented to the Faculty of the School of Engineering  
of the Air Force Institute of Technology

Air University

In Partial Fulfillment of the  
Requirements for the Degree of  
Master of Science in Electrical Engineering

Thomas M. Fitzgerald, B.E.E.E.

Captain, USAF

December 1994

Approved for public release; distribution unlimited

REPORT DOCUMENTATION PAGE			Form Approved OMB No. 0704-0188	
<small>Public reporting burden for this collection of information is estimated to average 1 hour per response, including the time for reviewing instructions, searching existing data sources, gathering and maintaining the data needed, and completing and reviewing the collection of information. Send comments regarding this burden estimate or any other aspect of this collection of information, including suggestions for reducing this burden, to Washington Headquarters Services, Directorate for Information Operations and Reports, 1215 Jefferson Davis Highway, Suite 1204, Arlington, VA 22202-4302, and to the Office of Management and Budget, Paperwork Reduction Project (0704-0188), Washington, DC 20503.</small>				
1. AGENCY USE ONLY (Leave blank)	2. REPORT DATE December 1994	3. REPORT TYPE AND DATES COVERED Master's Thesis		
4. TITLE AND SUBTITLE Design and Characterization of Resonant Cavity Light-Emitting Diodes		5. FUNDING NUMBERS		
6. AUTHOR(S) Thomas M. Fitzgerald				
7. PERFORMING ORGANIZATION NAME(S) AND ADDRESS(ES) Air Force Institute of Technology, WPAFB OH 45433-6583		8. PERFORMING ORGANIZATION REPORT NUMBER AFIT/GEO/ENP/94D-02		
9. SPONSORING / MONITORING AGENCY NAME(S) AND ADDRESS(ES)		10. SPONSORING / MONITORING AGENCY REPORT NUMBER		
11. SUPPLEMENTARY NOTES				
12a. DISTRIBUTION / AVAILABILITY STATEMENT  Distribution Unlimited		12b. DISTRIBUTION CODE		
13. ABSTRACT (Maximum 200 words) <p style="text-align: center;"><b>Abstract</b></p> <p>This thesis describes an investigation into the emission properties of Resonant Cavity Light Emitting Diodes (RCLED). RCLEDs are a new photonic device that promise laser-like properties of narrow output frequency spread and high output power, without the usual laser disadvantages of shorter lifetime and increased maintenance and lifetime costs. Specifically, this thesis examines the functional dependence between emitted wavelength and the RCLED microcavity, and attempts to correlate theory with experimental data. This thesis introduces a classical wave interference model that calculates the Spontaneous Emission Enhancement Factor (<math>\Xi</math>) with angular dependence.</p>				
14. SUBJECT TERMS Resonant Cavity, Quantum Well, Spontaneous Enhancement			15. NUMBER OF PAGES 135	
			16. PRICE CODE	
17. SECURITY CLASSIFICATION OF REPORT UNCLASSIFIED	18. SECURITY CLASSIFICATION OF THIS PAGE UNCLASSIFIED	19. SECURITY CLASSIFICATION OF ABSTRACT UNCLASSIFIED	20. LIMITATION OF ABSTRACT UL	

## *Preface*

This thesis is a study of the spectral emission properties of Resonant Cavity Light-Emitting Diodes (RCLEDs), a member of the class of surface-emitting semiconductor devices. The RCLED promises laser-like qualities of narrow beam width without sacrificing the reliability of the conventional LED. The following people have supported my efforts and I owe them my gratitude.

Thanks to Jim Lott for developing my interest in Photonics and then supporting me all the way to a finished product.

Thanks to Prof. S. D. Hersee and Prof. K. J. Malloy at the Center for High Technology Materials, The University of New Mexico, Albuquerque NM, for growing and fabricating the devices. They made this thesis possible with their selfless assistance.

Thanks to Captain Jeff W. Grantham, Major Paul H. Ostdiek, and Dr. Victor M. Bright for helping polish this into a final product, by taking the time to form my committee.

Thanks to the Dayton Rugby Club for allowing me to work off some AFIT frustrations.

Thanks to Lisa, my wife and best friend.

Tom Fitzgerald

## Table of Contents

	Page
Preface .....	ii
Abstract .....	x
1. Introduction.....	1-1
1.1 Background.....	1-1
1.1.1 Distributed Bragg Reflectors .....	1-2
1.1.2 Fabry-Perot Cavity .....	1-3
1.1.3 Quantum Wells .....	1-5
1.1.4 Theory of Operation.....	1-6
1.1.5 Performance Characteristics .....	1-7
1.2 Problem Statement.....	1-8
1.3 Scope .....	1-9
1.4 Approach/Methodology .....	1-10
1.4.1 Design .....	1-10
1.5 Sequence of Presentation .....	1-11
2. Design Theory .....	2-1
2.1 Distributed Bragg Reflectors (DBRs).....	2-1
2.1.1 Compositional Grading of DBRs .....	2-6
2.1.2 Complex Refractive Index .....	2-10
2.2 Fabry-Perot Cavities .....	2-12
2.2.1 RCLED Microcavity.....	2-14
2.2.2 RCLED Microcavity Parameters.....	2-17
2.3 Reflectance Calculations for RCLED .....	2-17
2.3.1 Example Calculation .....	2-19
2.4 Quantum Well Layers .....	2-21
2.4.1 Ternary and Quaternary Compound Materials.....	2-21
2.4.2 Allowed Energy Levels .....	2-22
2.4.3 Quantum Well Gain Spectrum.....	2-27
2.4.4 Quantum Well Rate of Spontaneous Emission.....	2-29
2.5 The RCLED Structure .....	2-31
2.5.1 Spontaneous Emission Enhancement Factor .....	2-31
2.5.2 Electric Field Confinement Factor .....	2-33
2.5.3 RCLED Losses .....	2-34
2.6 Summary .....	2-35

	Page
3. Designing The RCLED.....	3-1
3.1 Introduction .....	3-1
3.2 Structure 1: The Cavity.....	3-1
3.3 Structure 2: The Cavity with Upper and Lower DBRs (RCLED) .....	3-5
3.4 The Spontaneous Emission Enhancement Factor: $\Xi$ .....	3-9
3.4.1 Derivation of $\Xi$ .....	3-10
3.4.2 Applying $\Xi$ .....	3-13
3.4.3 Examining the Effects of $\Xi$ .....	3-14
3.5 Summary .....	3-18
4. Experimental Method .....	4-1
4.1 Laboratory Configuration.....	4-1
4.2 Photo-Luminescence Experimental Setup .....	4-2
4.3 Electro-Luminescence Experimental Setup .....	4-4
4.4 Angular Measurements Using Fiber Optic Probe .....	4-5
4.5 Aligning The Fiber Optic Probe .....	4-8
5. Experimental Results.....	5-1
5.1 Introduction .....	5-1
5.2 Device Parameters.....	5-2
5.3 Experimental Data Presentation .....	5-3
5.4 Comparison of Calculated and Experimental Results.....	5-12
5.5 Results Summary .....	5-15
6. Conclusion .....	6-1
Appendix A : Reflectance Calculations .....	A-1
Appendix B : Mathcad Reflectance Calculation Document.....	B-1
Appendix C : Quantum Well Energy Level and Gain Calculations.....	C-1
Bibliography .....	1
Vita .....	1

## List of Figures

Figure	Page
Figure 1. Simplified structure of LED and RCLED architectures showing photon emission patterns .....	1-4
Figure 2. Comparison of RCLED and conventional LED emission spectra .....	1-4
Figure 3. DBR stack containing high-low index quarter wave layers .....	1-5
Figure 4. Typical Fabry-Perot Cavity .....	1-5
Figure 5. Simplified energy band diagram of a quantum well heterostructure showing allowed discrete energy transitions between electron-hole levels .....	1-6
Figure 6 Schematic diagram of RCLED test structure .....	1-7
Figure 7. The two structures examined .....	1-10
Figure 8. Two boundary problem .....	2-3
Figure 9. Calculated reflectance vs. number of HL layers for $\text{Al}_{x_H}\text{Ga}_{1-x_H}\text{As} / \text{Al}_{x_L}\text{Ga}_{1-x_L}\text{As}$ DBR on GaAs substrate. $\lambda_0 = 850\text{nm}$ . $\Delta n = n_H - n_L$ .....	2-5
Figure 10. Sample calculated reflectance spectra for $\text{Al}_{0.15}\text{Ga}_{0.85}\text{As} / \text{AlAs}$ DBR with 38 HL periods on GaAs substrate (absorption effects included) $\lambda_0 = 850\text{nm}$ .....	2-5
Figure 11. As the number of HL half wave periods of Figure 10 are increased the bandstop region of the DBR is narrowed to the limit of Equation 10 .....	2-6
Figure 12. Index profile for periodically graded layers of $(\text{Al}_{x_H}\text{Ga}_{1-x_H})_{0.5}\text{In}_{0.5}\text{P} / (\text{Al}_{x_L}\text{Ga}_{1-x_L})_{0.5}\text{In}_{0.5}\text{P}$ with $x_H = 0.1$ , $x_L = 0.9$ and $n_H(\lambda_0) = 3.429$ , $n_L(\lambda_0) = 3.171$ where $\lambda_0 = 680\text{nm}$ .....	2-7
Figure 13. Calculated reflectance spectra from 50 graded $(\text{Al}_x\text{Ga}_{1-x})_{0.5}\text{InP}$ HL periods with a GaAs substrate ( $n \sim 3.7$ ). $x_H = 0.1$ , $x_L = 0.9$ and $n_H(\lambda_0) = 3.429$ , $n_L(\lambda_0) = 3.171$ where $\lambda_0 = 680\text{nm}$ .....	2-9
Figure 14. Energy bandgap vs. lattice constant .....	2-9
Figure 15. Real refractive index of $\text{Al}_x\text{Ga}_{1-x}\text{As}$ .....	2-11
Figure 16. Imaginary refractive index of $\text{Al}_x\text{Ga}_{1-x}\text{As}$ .....	2-12
Figure 17. Transmittance characteristics of Fabry-Perot cavity .....	2-13
Figure 18. RCLED structure showing microcavity, DBRs, and devices (not to scale) .....	2-15
Figure 19. Penetration depth in distributed mirrors .....	2-15



Figure	Page
Figure 20. Scheme for dividing HL layers into sublayers in reflectance program .....	2-19
Figure 21. Reflectance spectrum of RCLED with 6 HL periods of $\text{Al}_{0.15}\text{Ga}_{0.85}\text{As}/\text{AlAs}$ in the upper DBR, 38 HL periods of $\text{Al}_{0.15}\text{Ga}_{0.85}\text{As}/\text{AlAs}$ in the lower DBR and a $1\lambda$ , at $\lambda_0 = 850\text{nm}$ , cavity (Calculated for TE polarization) .....	2-20
Figure 22. Range of possible emission wavelengths for selected compound semiconductors .....	2-22
Figure 23. (a) Geometry of quantum well. (b) Energy level diagram for electrons and holes in quantum well. (c) Cross section of E-k relation .....	2-23
Figure 24. Dependence of emission wavelength on $\text{Al}_x\text{Ga}_{1-x}\text{As}$ well width and aluminum content $x$ with an $\text{Al}_{0.15}\text{Ga}_{0.85}\text{As}$ barrier region .....	2-25
Figure 25. Wavefunctions of energy levels in conduction band calculated for a $15\text{nm}$ GaAs quantum well with $\text{Al}_{0.3}\text{Ga}_{0.7}\text{As}$ barrier layers .....	2-26
Figure 26. Wavefunctions of heavy hole energy levels in valence band calculated for a $15\text{nm}$ GaAs quantum well with $\text{Al}_{0.3}\text{Ga}_{0.7}\text{As}$ barrier layers .....	2-26
Figure 27. Gain for $8\text{nm}$ GaAs quantum well with a $\text{Al}_{0.15}\text{Ga}_{0.85}\text{As}$ barrier layers for various well carrier concentrations showing both calculated (sharp) and convolved (smoothed) spectra at $T=300\text{K}$ .....	2-30
Figure 28. Spontaneous emission rates for a $8\text{nm}$ GaAs quantum well with $\text{Al}_{0.15}\text{Ga}_{0.85}\text{As}$ barrier layers for various well carrier concentrations showing both calculated (sharp) and convolved (smoothed) spectra at $T=300\text{K}$ .....	2-31
Figure 29. Graphic representation of architecture for $\Xi$ in Equation 47, only normal propagation is considered here .....	2-32
Figure 30. Normalized electric field intensity inside RCLED plotted against distance from substrate for $\lambda = 841\text{nm}$ .....	2-33
Figure 31. Normalized electric field intensity inside RCLED plotted for against distance from substrate $\lambda = 825\text{nm}$ .....	2-34
Figure 32. Schematic of RCLED structures .....	3-2
Figure 33. Composition diagram of Structure 1 .....	3-3
Figure 34. Calculated allowed energy levels for quantum wells of Structure 1 at $T=300\text{K}$ .....	3-3
Figure 35. Calculated gain of an $8\text{nm}$ GaAs quantum well surrounded by $10\text{nm}$ $\text{Al}_{0.15}\text{Ga}_{0.85}\text{As}$ barrier layers .....	3-4

Figure	Page
Figure 36. Calculated rate of spontaneous emission of an 8nm GaAs quantum well surrounded by 10nm	
Al <sub>0.15</sub> Ga <sub>0.85</sub> As barrier layers .....	3-5
Figure 37. Composition diagram for Structure 2.....	3-6
Figure 38. Calculated reflectance and phase spectra for Structure 2, including absorption. ( $\kappa \neq 0$ ) .....	3-7
Figure 39. Calculated reflectance and phase spectra for Structure 2, not including absorption. ( $\kappa = 0$ ) .....	3-7
Figure 40. Example periodic grading schemes of high-low index layers .....	3-8
Figure 41. Actual refractive index profile of Structure 2 at $\lambda_o = 850nm$ used in reflectance program .....	3-8
Figure 42. Calculated reflectance spectra for upper and lower DBRs of Structure 2 at 0° incidence angle.....	3-9
Figure 43. Graphic representation of architecture for $\Xi$ .....	3-10
Figure 44. $\Xi$ for Structure 2 with quantum well located at the center of the cavity (TE polarized) .....	3-15
Figure 45. Normalized $\Xi$ for Structure 2 at 0° and 40° with calculated reflectance spectrum(TE polarized) .....	3-15
Figure 46. $\Xi$ calculated for quantum well layer located $\lambda/4$ away from the center of the microcavity toward $R_2$ .	3-16
Figure 47. $\Xi$ calculated for quantum well layer located $\lambda/4$ away from the center of the microcavity toward $R_1$ .	3-16
Figure 48. Calculated spontaneous emission from Structure 2 for carrier injection levels of $1.5 \times 10^{18} \text{ cm}^{-3}$ and $2.5 \times 10^{18} \text{ cm}^{-3}$ . T = 300K.....	3-18
Figure 49. Location of samples E236 and E231 on 2'' GaAs wafer .....	4-1
Figure 50. Device layout on processed samples (the size of the aperture is indicated) .....	4-2
Figure 51. Experimental setup for photo-luminescence and reflectance measurements on RCLEDs.....	4-3
Figure 52. Experimental setup for electro-luminescence and reflectance measurements of RCLEDs.....	4-4
Figure 53. Fiber-optic probe with angular translation used in experiments. ....	4-7
Figure 54. Fiber being rotated around sample RCLED, the dashed lines represent the numerical aperture of the fiber.....	4-7
Figure 55. Diagram of E236 and E231 orientation used in PL (left) and EL (right).....	5-1
Figure 56. Measured electro-luminescence spectrum of E231 (Structure 2) versus angular deviation from normal	5-4
Figure 57. Normalized calculated E231 (Structure 2) emission (solid) using measured E236(Structure 1) emission.	5-4
Figure 58. Measured reflectance from various locations on unprocessed E231 sample (Structure 2) .....	5-6

Figure	Page
Figure 59. Measured (solid) and calculated (dashed) reflectance from device E231 at location 3 (unprocessed) in	
Figure 55 .....	5-6
Figure 60. Electro-luminescence of sample E236 versus angle .....	5-7
Figure 61. Measured electro-luminescence spectrum from sample E236 (Structure 1) for various injection currents	5-8
Figure 62. Measured electro-luminescence of sample E231 (Structure 2) for various injection currents .....	5-9
Figure 63. Measured electro-luminescence and reflectance spectra from same location on sample E231 (Structure 2).....	5-10
Figure 64. Photo-luminescence of sample E236 (Structure 1) at various input optical power densities.....	5-11
Figure 65. Photo-luminescence from sample E231 (Structure 2).....	5-11
Figure 66. Measured FWHM and Q for sample E231 (Structure 2) under electro-luminescence (Figure 62) showing linear correlation coefficients for the data (dotted) .....	5-13
Figure 67. Calculated and experimental peak $\lambda$ for E231 (Structure 2).....	5-13
Figure 68. Calculated and experimental FWHM for E231 (Structure 2).....	5-14
Figure 69. Plane wave incident on a set of thin films.....	A-1

## *List of Tables*

Table	Page
Table 1. Fresnel Phase Change Upon Reflection.....	2-3
Table 2. Comparison of Selected Cavity Parameters.....	2-20
Table 3. Material parameters for Figure 34.....	3-4
Table 4. Calculated Parameters of Figure 48.....	3-18
Table 5. Equipment Listing for Photo-Luminescence.....	4-3
Table 6. Growth Table for E231 and E236.....	5-3
Table 7. Measured Parameters for Figure 56.....	5-5
Table 8. Measured Parameters for Figure 61.....	5-9
Table 9. Measured Parameters for Figure 62.....	5-9

## *Abstract*

This thesis describes an investigation into the emission properties of Resonant Cavity Light Emitting Diodes (RCLED). RCLEDs are a new photonic device that promise laser-like properties of narrow output frequency spread and high output power, without the usual laser disadvantages of shorter lifetime and increased maintenance and lifetime costs. Specifically, this thesis examines the functional dependence between emitted wavelength and the RCLED microcavity, and attempts to correlate theory with experimental data. This thesis introduces a classical wave interference model that calculates the Spontaneous Emission Enhancement Factor ( $\Xi$ ) with angular dependence.

# Design and Characterization of Resonant Cavity Light Emitting Diodes

## 1. Introduction

### 1.1 Background

Light-emitting diodes (LEDs) have long been a trusty workhorse of the scientific and industrial communities. Though relegated to display and short distance communications applications, they have nevertheless performed well and faithfully. The simplest LEDs are composed of semiconductor material, such as GaAs, with a p-n homojunction. When an applied forward bias exceeds the energy bandgap of the material, injected electrons and holes recombine at the p-n junction to form photons resulting in emitted light. The wavelength of the emitted light ( $\lambda_0$ ) is related to the energy bandgap by  $E = hc / \lambda_0$ , where  $E$  is the energy bandgap in electron-volts,  $h$  is Planck's constant, and  $c$  is the speed of light in a vacuum. The failings of LEDs had always been low intensity, short coherence time, and omni-directional output. Thanks to recent advances in the epitaxial growth of compound semiconductors, LEDs are now poised to enter a new era. Newer LEDs have the potential to replace incandescent bulbs, and even laser diodes, in a host of new applications such as: automobile brakelights, flat-panel high-definition displays, holographic illumination, barcode scanning, and as light sources for optical interconnects, fiber-optic communications networks, and optical data storage systems [1; 2; 3]. The useful lifetime of LEDs (> 1 million hours) also promises low replacement costs in these applications [4].

The topic of this thesis is a new architecture that promises LEDs with comparable coherence time, wavelength spread, and beam characteristics to lasers. This architecture is known as the Resonant Cavity (or Vertical Cavity) Light-Emitting Diode [5].

The Resonant Cavity Light-Emitting Diode (RCLED; pronounced rik-led) has many advantages compared to conventional LEDs. Architecturally it is very similar to the Vertical Cavity Surface Emitting Laser (VCSEL pronounced vik-sell) in that it consists of a quantum well active region in a Fabry-Perot microcavity of width  $d = q\lambda / 2$ , where  $q$  is a positive integer (Figure 1). Purcell predicted that the spontaneous emission from a medium within a microcavity (mirror separation  $d$  is comparable to the emission wavelength) would experience a change in lifetime [6]. Schubert et al. predicted that the spontaneous lifetime is shortened (enhanced) for on-resonance optical transitions, but is lengthened (inhibited) for off-resonance optical transitions [5]. The RCLED is designed so that the spontaneous emission lifetime is shortened and photons are emitted at an increased rate with smaller wavelength spread at the design wavelength,  $\lambda_0$  [7; 8; 9]. Light emission occurs through both top and bottom surfaces, but is predominantly through the mirror with the lesser reflectance; this is usually designed to be the upper mirror ( $R_{upper} < R_{lower}$ ). Figure 1 shows the differences in architecture and photon emission between the conventional LED and the RCLED. Figure 1 also shows the angular dependence of the emitted intensity. The RCLED's emission spectrum changes with increasing angle from the surface normal. This is not the case for the conventional LED. Figure 2 shows representative emission spectra vs. relative intensity for Figure 1. The emission wavelength and full-width at half maximum (FWHM) of a RCLED are variable and are controlled by the cavity width and reflectances of the upper and lower mirrors.

**1.1.1 Distributed Bragg Reflectors.** A DBR consists of alternating layers of high and low refractive index semiconductor epitaxial layers. Each DBR interface reflects a fraction of the incident light. For the DBR to be strongly reflective the light must add up in phase,

and therefore each layer should be a quarter wavelength ( $\lambda/4$ )<sup>1</sup> thick. Figure 3 shows the alternating high-low (HL) index periods of the DBR. The design wavelength ( $\lambda_0$ ) of the DBR is referred to as the Bragg Wavelength. The DBR Reflectance is a function of wavelength, and is a maximum at the design wavelength at zero degrees incident angle. Maximum reflectance increases with increasing number of HL periods and also increases for larger differences between the refractive indices of the high and low index layers.

**1.1.2 Fabry-Perot Cavity.** A Fabry-Perot cavity is formed by placing two mirrors a known distance,  $d$ , apart and ensuring they are parallel with a high degree of accuracy [10: 159]. The cavity supports longitudinal modes where  $d = q\lambda/2$ , where  $q$  is a positive integer and  $\lambda$  is the mode wavelength. The design wavelength of the RCLED must be a mode of the cavity. The Fabry-Perot cavity of the RCLED contains a photon emitting active region, for example a quantum well (QW). The quantum well must be designed to emit photons of the proper wavelength to couple with the transmission modes of the Fabry-Perot cavity. The cavity is designed so that transmission modes are sufficiently far apart in wavelength such that the medium can only couple (and therefore emit) to a single mode within the QW spectral gain. Figure 4 shows a Fabry-Perot cavity with incoming ( $i$ ), reflected( $r$ ) and transmitted( $t$ ) electric fields. The cavity transmits those wavelengths that correspond to it's longitudinal modes.

---

<sup>1</sup> Note that  $\lambda = \lambda_0 / n$ , where  $n$  = refractive index.



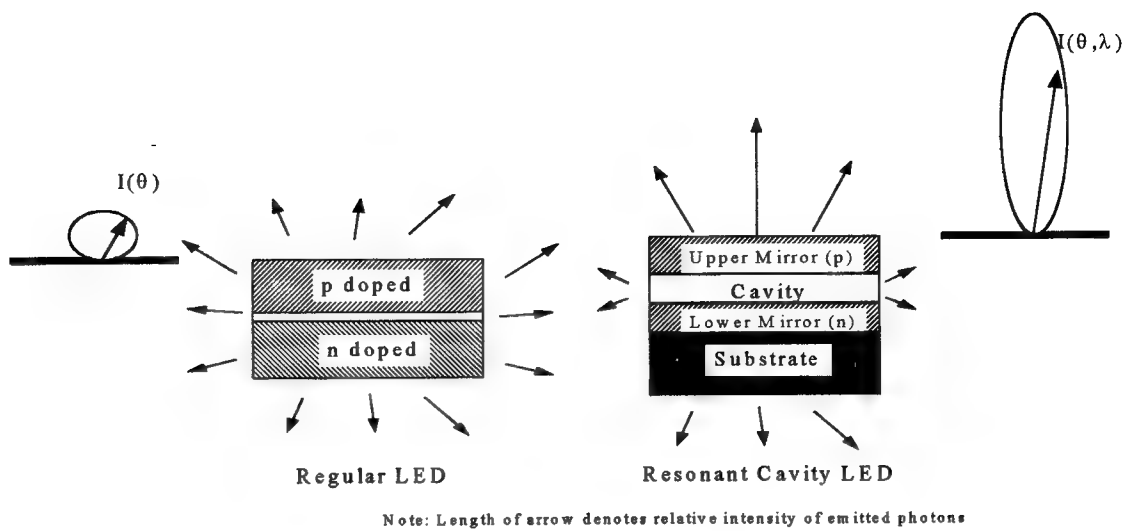


Figure 1. Simplified structure of LED and RCLED architectures showing photon emission patterns

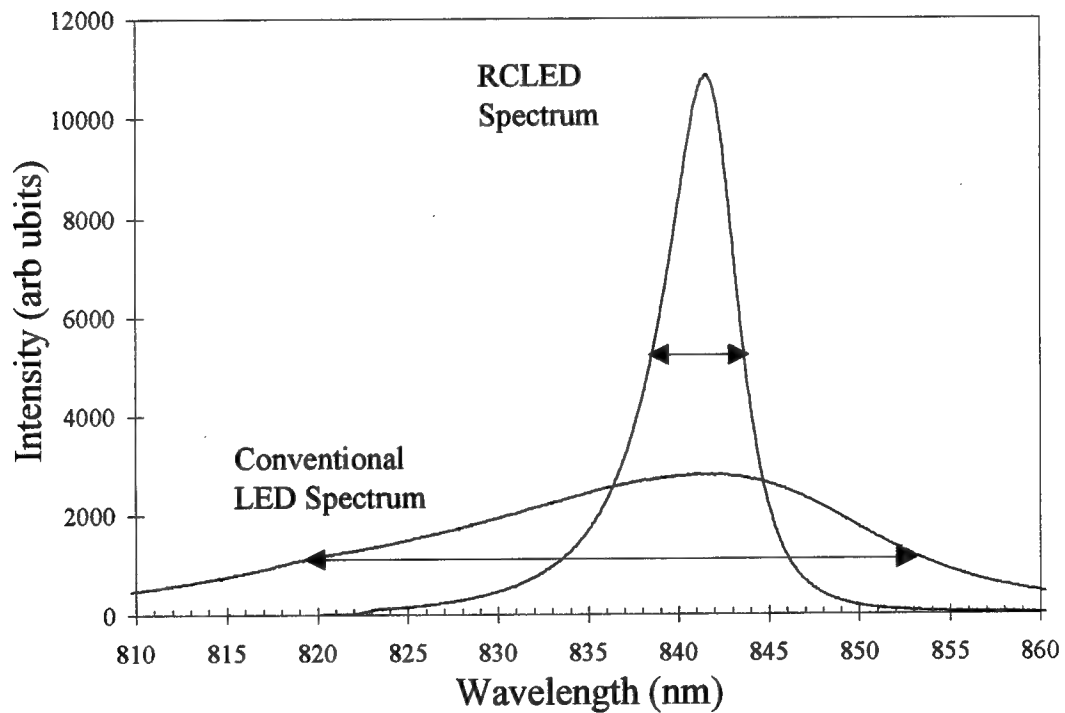


Figure 2. Comparison of RCLED and conventional LED emission spectra

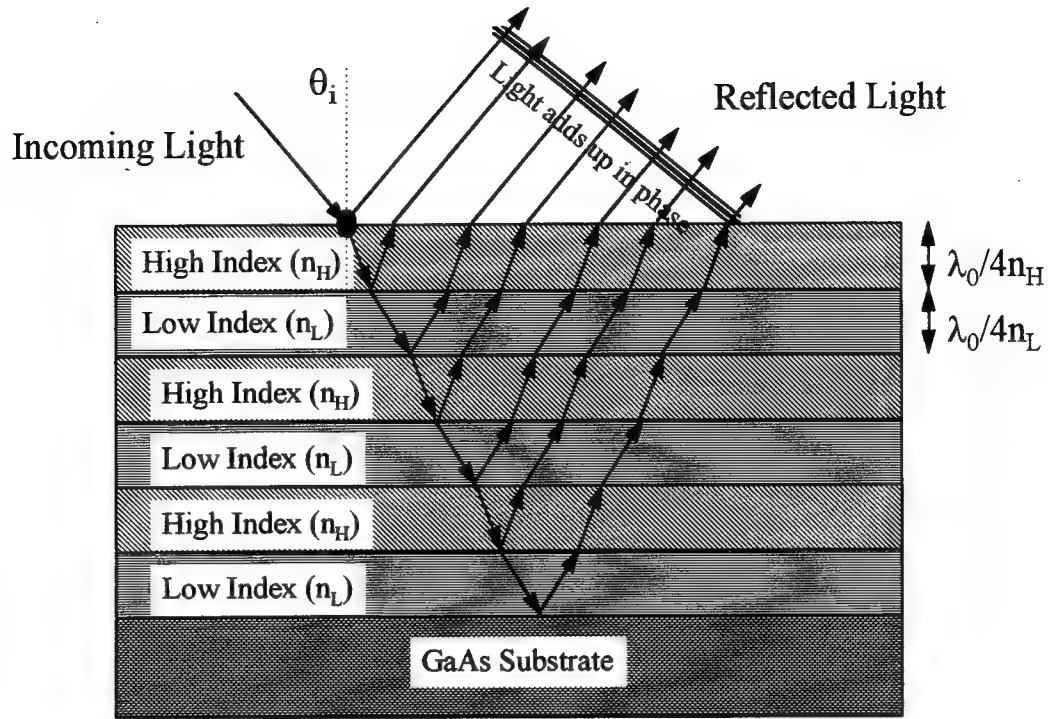


Figure 3. DBR stack containing high-low index quarter wave layers

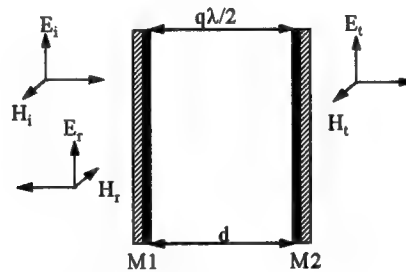


Figure 4. Typical Fabry-Perot Cavity

**1.1.3 Quantum Wells.** Quantum well (QW) active regions lower threshold current and simplify wavelength selection in laser diodes [11]. In contrast, LEDs are thresholdless but can also use QWs for more efficient photon generation. Figure 5 shows the conduction and valence bands for a single QW, along with the variables that define the quantized energy levels within the QW. These are  $L_{QW}$ : the width of the well,  $\Delta E_c$ : the conduction band offset, and  $\Delta E_v$ : the valence band offset.

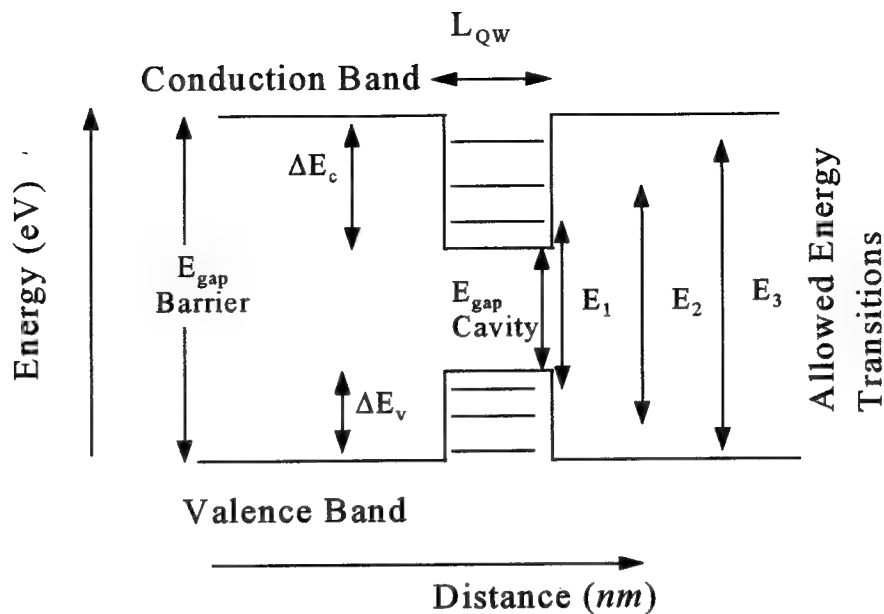


Figure 5. Simplified energy band diagram of a quantum well heterostructure showing allowed discrete energy transitions between electron-hole levels

**1.1.4 Theory of Operation.** Figure 6 shows a schematic of an example fabricated infrared (IR) RCLLED [15: 124]. The upper and lower mirror structures are composed of AlAs/ $\text{Al}_{0.15}\text{Ga}_{0.85}\text{As}$  distributed Bragg reflectors (DBRs). The applied voltage,  $V_{in}$ , causes the carriers to migrate toward, and recombine in, the quantum well. The Fabry-Perot cavity is resonant for recombination wavelengths that correspond to cavity transmission modes. The spontaneous emission is enhanced for those modes, given that the QW layer has been located at an anti-node of the electric field in the cavity.

Band offsets are barriers to current flow and increase device series resistance. Schemes to lower the series resistance include compositional grading of the  $\lambda/4$  layer interfaces,  $\delta$ -doping the  $\lambda/4$  heterolayers, using non- $\text{Al}_x\text{Ga}_{1-x}\text{As}$  materials for the DBRs such as ZnSe/ $\text{CaF}_2$ , and straining the DBR by mismatching the lattice constants of the  $\lambda/4$  layers.

[12; 13; 15]. This thesis deals exclusively with compositionally graded  $\text{Al}_x\text{Ga}_{1-x}\text{As}$  DBR designs.

To sum up, designing the RCLED requires matching the allowed QW energy transitions with the transition modes of the Fabry-Perot cavity, and placing the QW at an anti-node of the cavity electric field [9; 15].

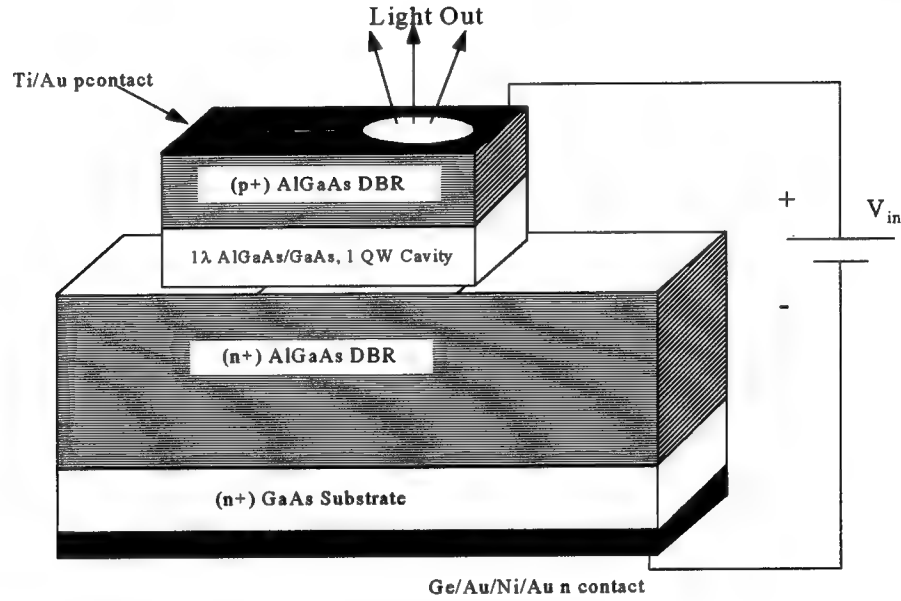


Figure 6 Schematic diagram of RCLED test structure

**1.1.5 Performance Characteristics.** The performance advantages of an RCLED compared to conventional LEDs are that the RCLED combines the thresholdless operation of an LED with laser-like coherence-time and beam properties. A conventional, bulk homojunction, LED's full-width at half-maximum (FWHM) may be approximated by  $\Delta\lambda = 1.45(\lambda_p^2 k_B T)$ , where  $k_B$  is Boltzmann's constant and  $T$  is the temperature in Kelvin [28: 584; 5]. Thus an LED emitting at  $850\text{nm}$  at room temperature ( $T = 300\text{K}$ ) will have a wavelength spread ( $\Delta\lambda$ ) of  $\sim 28\text{nm}$ . In contrast, an RCLED emitting at the same wavelength

could have  $4nm \leq \Delta\lambda \leq 28nm$  depending on the mirror reflectances (see experimental results) [5].

The benefits of a smaller  $\Delta\lambda$  may be seen from a fiber-optic communications example [14]. The pulse broadening due to chromatic dispersion (caused by  $\Delta\lambda$ ) is given by:

$$\Delta\tau = \left( \frac{1}{c} \frac{dn(\lambda_0)}{d\lambda_0} \right) l \Delta\lambda \quad (sec) \quad (1)$$

where  $l$  is the fiber length,  $\Delta\lambda$  is the source spectral width, and the bracketed term is the chromatic dispersion, which is constant for a given fiber ( $\sim 100ps/(km \ nm)$  at  $875nm$  for silica). Thus by decreasing  $\Delta\lambda$  by a factor of 7, pulse broadening is reduced, and consequently the length between optical-repeaters in the fiber is increased by a factor of 7.

## 1.2 Problem Statement

This thesis investigates the spectral gain characteristics of RCLEDs. This includes an investigation of the functional dependence between emitted-intensity, wavelength, radiation pattern, and device structure. Achieving this goal required designing, fabricating, and testing RCLEDs.

Designing the RCLED required first choosing a desired emission wavelength,  $\lambda_0$  and then “tuning” the quantum wells, Fabry-Perot cavity and DBRs to that wavelength. Tuning the QW involves selecting the composition of  $Al_xGa_{1-x}As$  for the barrier and well, and the well width necessary for electron-hole recombinations at the design wavelength. Tuning the Fabry-Perot cavity to the design wavelength requires making it an integral number of  $\lambda_0/2$

thick at  $\lambda_0$ . Tuning the DBR requires that each HL period be  $\lambda_0/2$  thick at  $\lambda_0$ . These thickness' are specified only at  $\lambda_0$  due to the wavelength dependence of the refractive index.

The devices were grown and fabricated by the Center for High Technology Materials (CHTM) at The University of New Mexico (UNM) at Albuquerque NM.

Testing the devices involved electro-luminescence (EL) and photo-luminescence (PL) excitation. The resulting emission from the RCLEDs was sampled for relative intensity and wavelength vs. increasing angle from the normal. Reflectance spectra were taken from each sample to verify the reflectances calculated during the design phase and also measure effects of mismatches between gain spectrum and the Fabry-Perot resonance. A model was developed to apply classical wave interference to the cavity.

### 1.3 Scope

The scope of this thesis is to design and characterize the spectral properties of infrared (IR) ( $\lambda_0 \sim 850nm$ )  $Al_xGa_{1-x}As$  RCLEDs. The actual research proceeded in the following steps.

a. Design RCLEDs with numerical software using previously proven techniques [15; 10; 20].

b. Estimate the spectral characteristics of the RCLED with particular emphasis on the functional dependence between emitted intensity, peak wavelength, and the radiation pattern [8]. Calculate the expected spectral characteristics of the RCLED for:

Structure 1: no DBRs around the resonant cavity;

Structure 2: two DBRs, with reflectances  $R_{lower} \sim 90\%$  and  $R_{upper} \sim 80\%$ , below and above the resonant cavity [16; 17].

- c. Construct the two RCLEDs mentioned in b.
- d. Characterize emission radiation of each RCLED using photo-luminescence (PL), and electro-luminescence (EL) [18; 15].

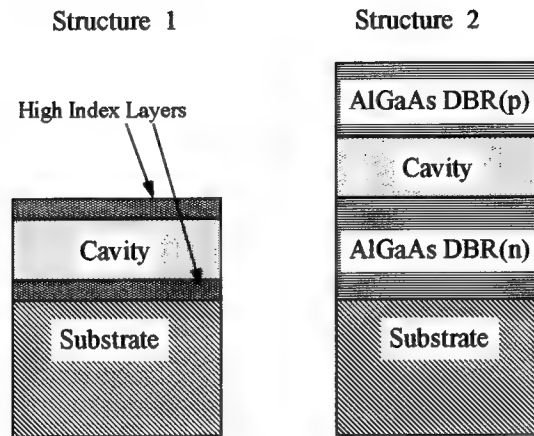


Figure 7. The two structures examined

#### 1.4 Approach/Methodology

The following theoretical basis was used for modeling the RCLED. First, the allowed energy states in the quantum wells were used to calculate a gain spectral model, in order to get the expected EL of Structure 1 (resonant cavity only) [16; 19]. This model gave information about the gain characteristics and peak emission wavelength of Structure 1. Secondly, the Macleod method was used to generate the reflectance values for both a DBR, and a Fabry-Perot cavity formed by two DBRs [10; 20]. This second model included the non-normal propagation of light and absorbing quarter-wave layers

**1.4.1 Design Assumptions.** Three key assumptions are used as a basis to begin work on this proposal. First, that the  $\lambda/4$  thick DBR layers can be built within allowed tolerances. Second, that the composition of the quantum wells will be accurate enough for calculation of material properties using parametric equations. These first two assumptions are based

on previous demonstrations of technical excellence in this field by The University of New Mexico at Albuquerque. Third, the complex refractive index information available for  $\text{Al}_x\text{Ga}_{1-x}\text{As}$  is considered accurate, and no further exploration of that work will be required. The different refractive indices of compound materials are published as a function of the fractional composition variable,  $x$  [21;22].

### **1.5 Sequence of Presentation**

Chapter 2 will familiarize the reader with the physics behind each of the components of the RCLED. That is: the compound semiconductor materials, complex refractive index, distributed Bragg reflectors, Fabry-Perot cavities, and quantum wells. Chapter 2 will conclude by putting these elements together and forming a RCLED. Chapter 3 will present the RCLED designs. This will include complete simulation of the RCLED characteristics for the designed structures. Chapter 4 contains the experimental setups that were used and all of the collected data for each of the RCLED structures. Chapter 5 presents the experimental results and compares them to the theoretical design. Chapter 6 contains a summary of conclusions and suggestions for further research.



## 2. Design Theory

This Chapter contains:

- the physics of the individual components of the Resonant Cavity LED (RCLED).
- design criteria for combining the individual components into an RCLED structure.
- a classical wave interference model for calculating the spectral output of an RCLED.

The basic components of the RCLED are: 1. the distributed Bragg reflectors; 2. the Fabry-Perot optical cavity; and 3. the quantum well active region embedded in the cavity. Each sub-section discusses, in some detail, the nuances behind decision making in RCLED design and how each individual piece of the RCLED must be designed and built to work at the design wavelength. The critical parameter is the design wavelength, or peak emission wavelength.

### 2.1 Distributed Bragg Reflectors (DBRs)

The distributed Bragg reflector consists of periodic, alternating high-low (HL) quarter wave ( $\lambda_0/4$ ) layers of refractive index material. The layers are constrained to have an *optical* thickness of a quarter of the design wavelength:

$$l_H n_H = l_L n_L = \lambda_0 / 4 \quad (nm) \quad (2)$$

- $l_H$  is the physical thickness of the high index layer
- $l_L$  is the physical thickness of the low index layer
- $n_H$  is the refractive index of the high index layer
- $n_L$  is the refractive index of the low index layer
- $\lambda_0$  is the design wavelength of the DBR.

The quarter wave ( $\lambda_0/4$ ) criterion for layer thickness ensures that at normal incidence, and for the design wavelength, each reflection from subsequent layers interferes constructively with the previous layer reflections. This requires that reflections from consecutive layers are in phase with respect to each other ( $2m\pi$ ,  $m=0,1,2..$  phase difference between reflected waves). Interference between reflected waves depends upon the Optical Path Difference ( $\Lambda$ ) in the routes taken between the two interfaces, and the Fresnel phase change upon reflection from an interface. Between two consecutive layers,  $\Lambda$  is given by (from Figure 8):

$$\Lambda = n_2|AB| + n_2|BC| - n_1|AD| \quad (nm) \quad (3)$$

which reduces to

$$\Lambda = 2n_2d \cos(\theta_i) \quad (nm) \quad (4)$$

where (Figure 8)  $\theta$  is the transmitted angle in the layer,  $d$  is the thickness of the layer, and  $n_2$  is the refractive index of the layer. The phase difference,  $\delta_{12}$ , between two rays from consecutive layers is obtained by multiplying  $\Lambda$  by the wavenumber  $k$  and then adding the Fresnel phase change upon reflection from each layer.

$$\delta_{12} = k\Lambda + \varphi_1 + \varphi_2 = \frac{4\pi}{\lambda}n_2d \cos(\theta_i) + \pi \quad (radians) \quad (5)$$

$$2m\pi = \frac{4\pi}{\lambda}n_2d \cos(\theta_i) + \pi \quad (radians) \quad (6)$$

$$2(m-1)\pi = \frac{4\pi}{\lambda}n_2d \cos(\theta_i) \quad (radians) \quad (7)$$

$$n_1 \sin \theta_1 = n_2 \sin \theta_2 \quad (unitless) \quad \text{Snell's Law (8)}$$

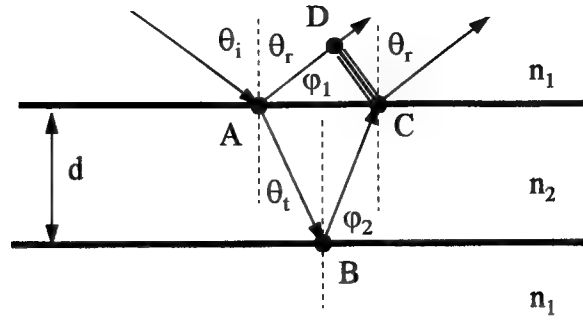


Figure 8. Two boundary problem

Table 1. Fresnel Phase Change Upon Reflection

	S-Polarization	P-Polarization
$n_i > n_t$	0	$\pi$
$n_t > n_i$	$\pi$	0

Table 1 shows the Fresnel phase changes applicable to the RCLED design. A more detailed listing is available in *OPTICS*, by Hecht [23:100]. The Fresnel phase change,  $\Delta\phi = \phi_2 - \phi_1$ , sums to  $\pm\pi$  (from Table 1), so for constructive interference  $kA$  must sum to a constant phase difference of  $\pi$ . Equation 6 shows two criteria for a constant phase difference of  $\pi$  between rays reflected from different layers. First, that the phase difference between two consecutive layers ( $\delta_{12}$ ) is a function only of incident angle (through Snell's law) if the layers have a thickness of  $d = \lambda_0/4n_2$ . Second, that the design wavelength thickness ( $\lambda_0/4$ ) criteria for the thin layers is true only at normal incidence. The peak reflected wavelength (wavelength required for  $2m\pi$  phase shift) decreases with increasing angle  $\theta_i$ . Intuition might suggest that as the pathlength through each layer increases with increasing angle, the design wavelength should also increase.

The maximum DBR reflectance occurs at the design wavelength. A simple formula, neglecting absorption, to determine the maximum reflectance for normal light incidence (0 deg) of a series of N periodic high-low index (HL)  $\lambda/2$  layers deposited on a substrate is given by[24]:

$$R_N = \left( \frac{1 - \left( \frac{n_s}{n_0} \right) \left( \frac{n_H}{n_L} \right)^{2N}}{1 + \left( \frac{n_s}{n_0} \right) \left( \frac{n_H}{n_L} \right)^{2N}} \right)^2 \quad (\text{unitless}) \quad (9)$$

- $n_s$  is the real refractive index of the substrate layer
- $n_0$  is the real refractive index of the incident layer
- $n_H$  is the real refractive index of the high index  $\lambda/4$  layer
- $n_L$  is the real refractive index of the low index  $\lambda/4$  layer
- $N$  is the number of periods of HL repeating  $\lambda/2$  layers

As shown for an example  $\text{Al}_{x_H}\text{Ga}_{1-x_H}\text{As} / \text{Al}_{x_L}\text{Ga}_{1-x_L}\text{As}$  DBR in Figure 9, the reflectance increases asymptotically to 1 for an increasing number of HL layers. The reflectance is also larger, for a given number of layers, for larger HL index difference, i.e.  $\Delta n = n_H - n_L$ . Figure 9 shows that high reflectance ( $R > 0.99$ ) is reached with about 25 HL periodic  $\lambda/2$  layers. The stopband bandwidth of the reflectance spectrum may be calculated from:

$$\Delta\lambda = \lambda_0 \frac{4}{\pi} \arcsin \left( \frac{n_H - n_L}{n_H + n_L} \right) \quad (nm) \quad (10)$$

where  $\lambda_0$  is the design wavelength of the DBR [10]. For the example of Figure 10, the bandwidth should be  $83.15nm$ . It is actually  $\sim 95nm$ . The discrepancy is due to Equation 10 giving an asymptotic limit for an increasing number of HL layers. Figure 11 shows that at 60 HL layers the bandstop has reached the asymptotic limit of Equation 10.

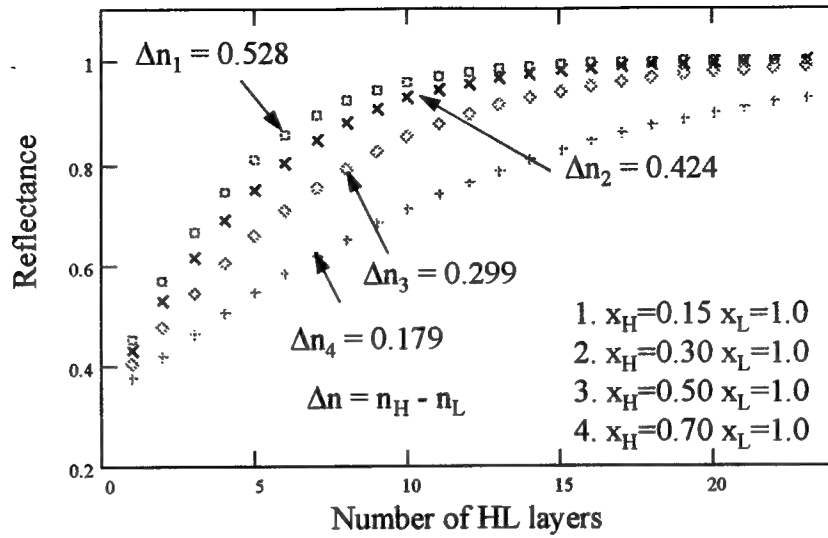


Figure 9. Calculated reflectance vs. number of HL layers for  $\text{Al}_{x_H}\text{Ga}_{1-x_H}\text{As} / \text{Al}_{x_L}\text{Ga}_{1-x_L}\text{As}$  DBR on GaAs substrate.  $\lambda_0 = 850\text{nm}$ .  $\Delta n = n_H - n_L$

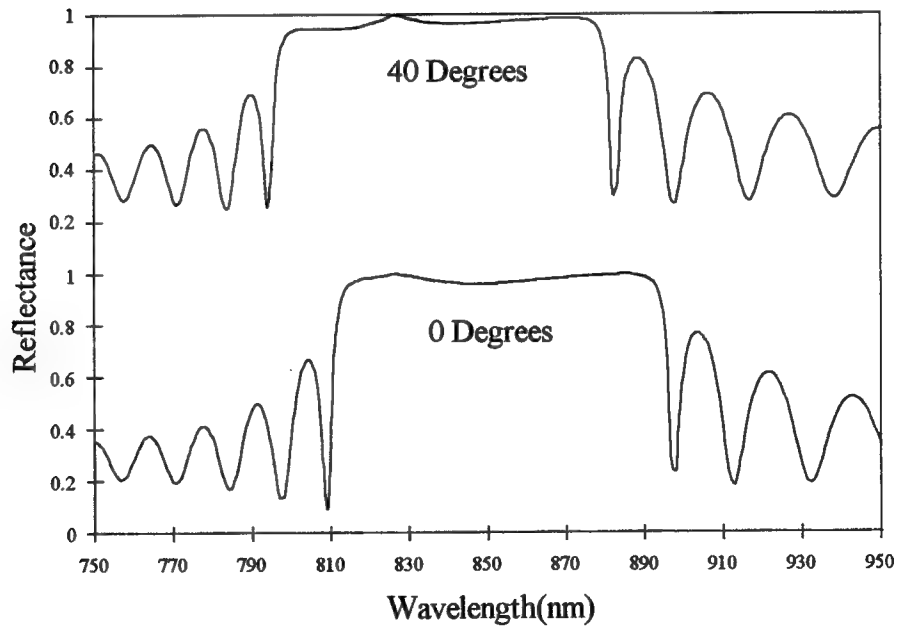


Figure 10. Sample calculated reflectance spectra for  $\text{Al}_{0.15}\text{Ga}_{0.85}\text{As} / \text{AlAs}$  DBR with 38 HL periods on GaAs substrate (absorption effects included)  $\lambda_0 = 850\text{nm}$

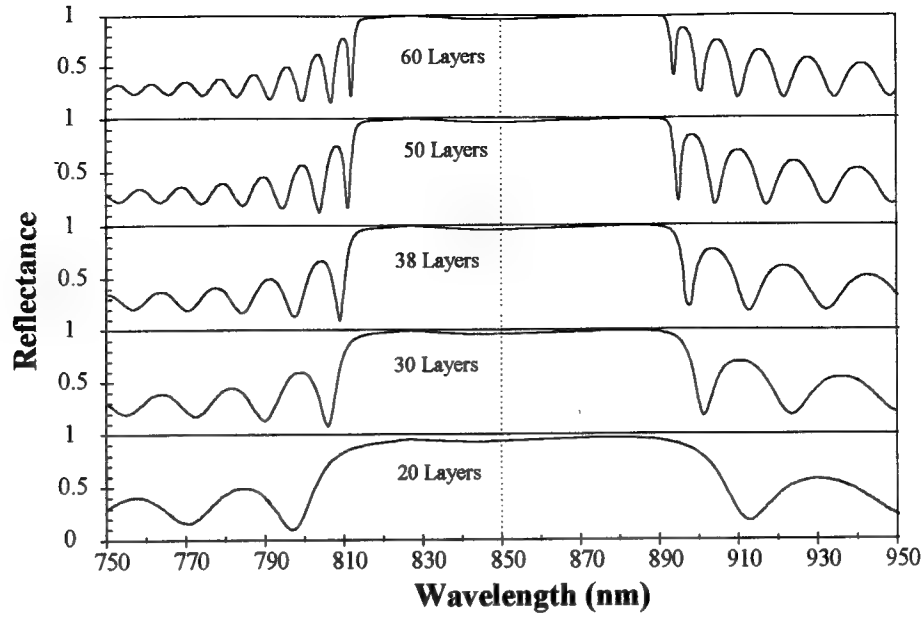


Figure 11. As the number of HL half wave periods of Figure 10 are increased the bandstop region of the DBR is narrowed to the limit of Equation 10

**2.1.1 Compositional Grading of DBRs.** In AlGaAs DBRs most of the resistance comes from the hetero-interfaces (between the HL layers) in p-doped mirrors [13; 15:54-63]. Various methods of decreasing resistance are used. One method of reducing resistance is to heavily dope the p-mirror. However the disadvantage is that free carrier absorption increases, and this decreases quantum efficiency. The method used in this thesis is to compositionally grade the HL interfaces of the DBR. For a compositionally-graded DBR quarter wave layer to meet the Bragg criteria the following equation must be true.

$$\int_{z_1}^{z_2} n(z)_{\lambda_0} dz = \frac{\lambda_0}{4} \quad (nm) \quad (11)$$

where the lower limit,  $z_1$ , is the start of that particular layer of growth and the upper limit,  $z_2$ , is the end. The subscript  $\lambda_0$  denotes that this relationship is true only at the design wavelength.

Compositionally grading the DBR decreases resistance because abrupt conduction and valence band energy offsets at hetero-junctions act as barriers to current flow [15:54-55]. By grading the interfaces the junctions are less abrupt and resistance to current flow is decreased.

Modern deposition systems such as Metal-Organic Vapor Phase Epitaxy (MOVPE), and Molecular Beam Epitaxy (MBE) create semiconductor structures an atomic layer at a time. It is therefore possible to vary the composition of the deposited structure, as it is being built, by varying the relative ratios of the constituent parts. Figure 12 shows example profiles of HL layers for comparison purposes. Each grading type has the same value of maximum high index and minimum low index. The only difference is the grading scheme employed between these index upper and lower limits.

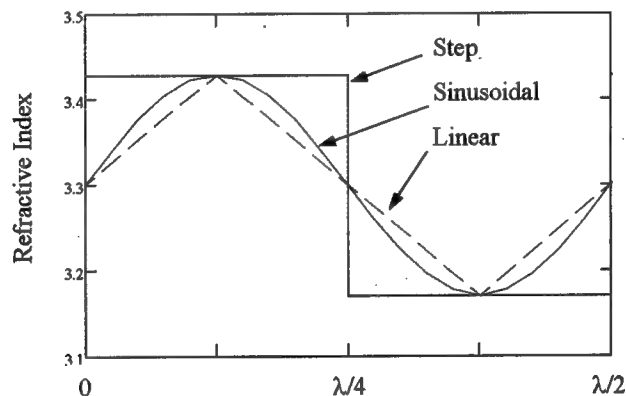


Figure 12. Index profile for periodically graded layers of  $(\text{Al}_{x_H}\text{Ga}_{1-x_H})_{0.5}\text{In}_{0.5}\text{P}/(\text{Al}_{x_L}\text{Ga}_{1-x_L})_{0.5}\text{In}_{0.5}\text{P}$  with  $x_H = 0.1$ ,  $x_L = 0.9$  and  $n_H(\lambda_0) = 3.429$ ,  $n_L(\lambda_0) = 3.171$  where  $\lambda_0 = 680\text{nm}$

Figure 13 shows the spectra of the different compositionally graded DBRs of Figure 12. The material system is  $(\text{Al}_x\text{Ga}_{1-x})_{0.5}\text{In}_{0.5}\text{P}$  with  $x_H = 0.1$  and  $x_L = 0.9$ . The reflectance spectrum of a DBR depends on how wide the high and low index composition “plateaus” in Figure 12 are allowed to be. Wider “plateaus” mean a steeper grade, and higher reflectance

values. Narrower “plateaus” mean a less steep grade and lower reflectance values. In Figure 13 it is easy to see that the sinusoidal and step grading give the higher maximum reflectances because they have wider “plateaus”.

Figure 14 shows the energy bandgaps and lattice constants for both the AlGaAs and AlGaInP families of III-V compound semiconductors. The lines connecting the binary compounds give the energy bandgap and lattice constant for the ternary compounds made from a compositional variation of the elements [15]. For example, for the system  $\text{Al}_x\text{Ga}_{1-x}\text{As}$ , at  $x = 0$ , it has the properties of GaAs, whereas at  $x = 1$ , it has the properties of AlAs. An important feature of the  $\text{Al}_x\text{Ga}_{1-x}\text{As}$  compound family is that its lattice constant,  $a$ , hardly changes as  $x$  varies from 0 to 1. This means that  $\text{Al}_x\text{Ga}_{1-x}\text{As}$  DBRs may be grown with relative impunity with regard to composition. Lattice matching is an important parameter in growing DBRs because growing lattice mismatched layers leads to lower quality epitaxial material with cracks, defects, and dislocations. If growing  $(\text{Al}_x\text{Ga}_{1-x})_y\text{In}_y\text{P}$  compounds on GaAs substrates, for example, more care must be taken as the lattice constant has a large variation with  $x$  and  $y$ . This material is approximately lattice matched to GaAs when  $y \approx 0.5$  and  $0 \leq x \leq 1$ .



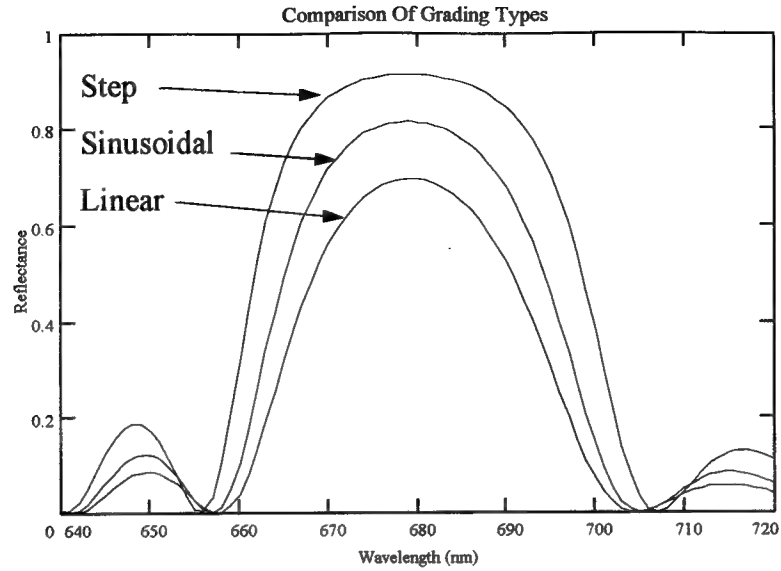


Figure 13. Calculated reflectance spectra from 50 graded  $(\text{Al}_x\text{Ga}_{1-x})_{0.5}\text{InP}$  HL periods with a GaAs substrate ( $n \sim 3.7$ ).  $x_H = 0.1$ ,  $x_L = 0.9$  and  $n_H(\lambda_0) = 3.429$ ,  $n_L(\lambda_0) = 3.171$  where  $\lambda_0 = 680\text{nm}$

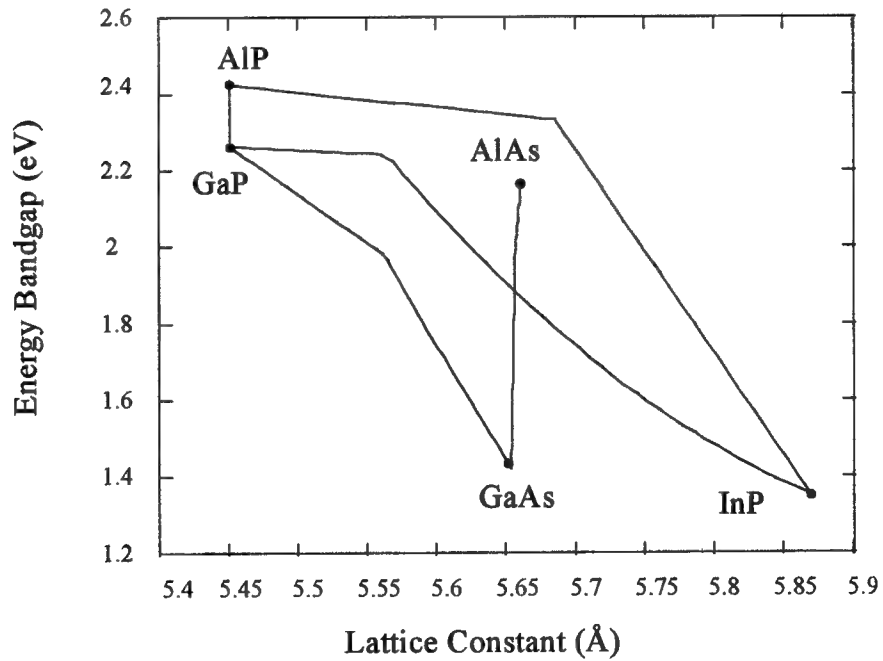


Figure 14. Energy bandgap vs. lattice constant.

**2.1.2 Complex Refractive Index.** Part of the problem of matching the DBR to a design wavelength is ensuring that the DBR does not attenuate the light through absorption. Absorption occurs when the photon energy is greater than the bandgap energy of the DBR layers.<sup>2</sup>

When the photon energy is greater than the DBR bandgap energy, photon absorption must be considered. The complex refractive index  $N$  used in this context consists of the real refractive index  $n$  and the complex extinction coefficient  $\kappa$  ( $N=n-i\kappa$ ). The form of the electric field wave equation, for a wave traveling in the  $x$ -direction is given by:

$$E = E_0 \exp \left\{ i \left( \omega t - \left[ \frac{2\pi(n-i\kappa)}{\lambda} \right] x \right) \right\} \quad (\text{Volts/m}) \quad (12)$$

The imaginary part of the complex refractive index,  $\kappa$ , becomes a real number and denotes an attenuation as seen in Equation 13.

$$E = E_0 \exp \left\{ -\frac{2\pi\kappa}{\lambda} x \right\} \exp \left\{ i \left( \omega t - \left[ \frac{2\pi(n)}{\lambda} \right] x \right) \right\} \quad (\text{Volts/m}) \quad (13)$$

The relationship between the extinction coefficient  $\kappa$  and the Lambert-Beer absorption coefficient  $\alpha$  ( $\text{m}^{-1}$ ) is given by  $\kappa = c\alpha / 2\omega$  where  $c$  represents the speed of light in a vacuum, and  $\omega$  is the angular frequency of the incoming light.

---

<sup>2</sup> Photon energy and wavelength are connected by  $E = hc / \lambda$ . For wavelength given in  $\mu\text{m}$  the numbers simplify to  $E = 1.24 / \lambda$  (eV).

Figure 15 and Figure 16 are derived from work by Adachi and Aspnes. The refractive index values (real) for energies less than  $1.5\text{ eV}$  come from extrapolation equations by Adachi. The complex refractive index plot is based on data presented by Aspnes. Aspnes presented his data numerically for varying compositions and energy values. The compositions varied from  $x = 0.1$  to  $x = 0.8$ . The energy values varied from  $1.5\text{ eV}$  to  $3.4\text{ eV}$  in steps of  $0.1\text{ eV}$ . A cubic spline function was used to interpolate between energy values for the composite Adachi/Aspnes data set. A linear fit was used to interpolate between known compositional values when the composition was one not measured by Aspnes. Figure 16 shows that the extinction coefficient  $\kappa$  is strongly dependent on both the fractional composition of  $\text{Al}_x\text{Ga}_{1-x}\text{As}$  and on the photon energy.

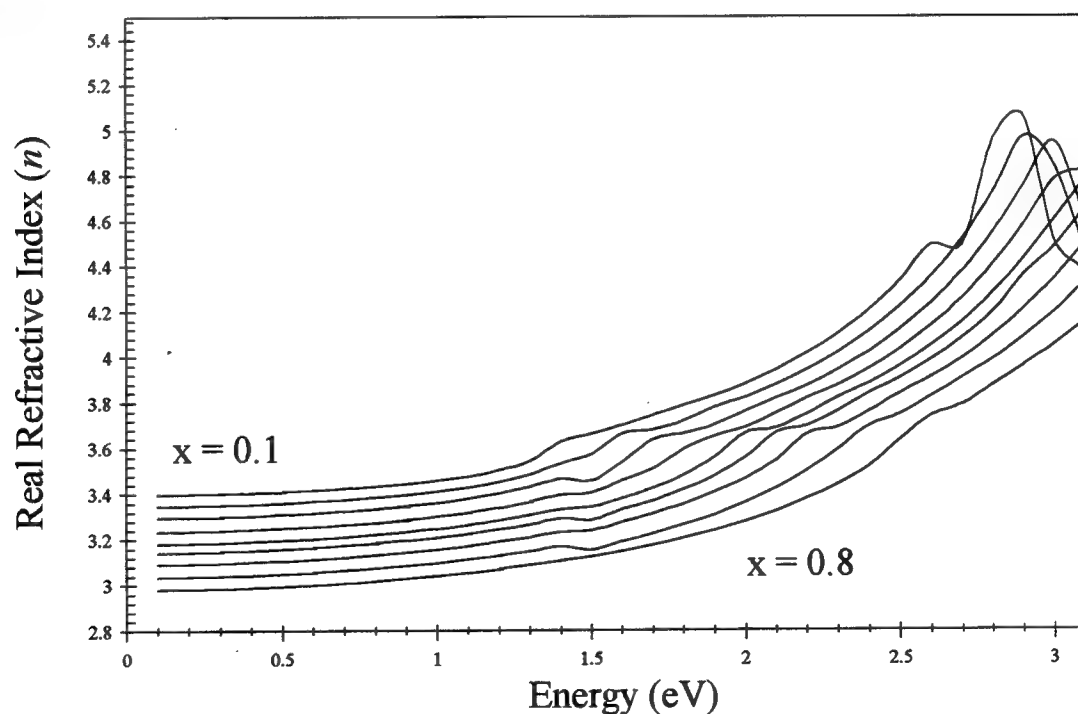


Figure 15. Real refractive index of  $\text{Al}_x\text{Ga}_{1-x}\text{As}$

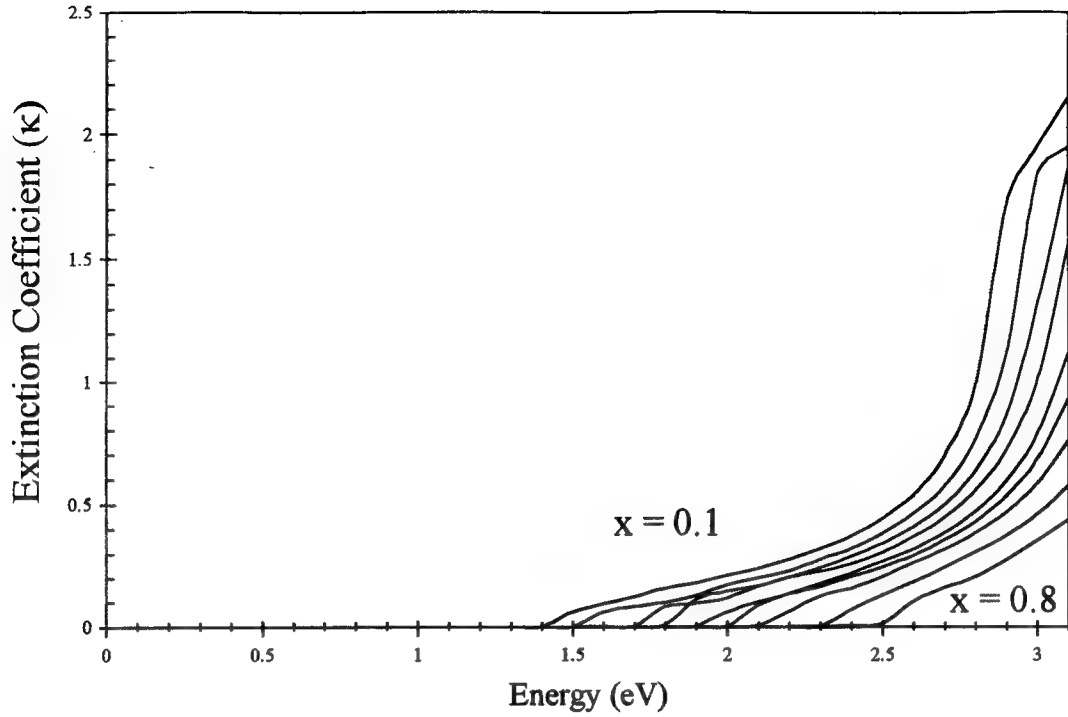


Figure 16. Imaginary refractive index of  $\text{Al}_x\text{Ga}_{1-x}\text{As}$

When absorptance is included, the form of the phase delay changes from Equation 5.

The phase delay with absorptance is given by:

$$\delta_{12} = \frac{2\pi}{\lambda} d_2 (n_2^2 - \kappa_2^2 - n_0^2 \sin^2 \theta_0 - 2in_2\kappa_2)^{1/2} \quad (\text{radians}) \quad (14)$$

where  $n_0$  and  $\theta_0$  are the real refractive index and incidence angle of the incident medium [10;20].

## 2.2 Fabry-Perot Cavities

A Fabry-Perot cavity consists of two parallel planar mirrors, with reflectances  $R_1$  and  $R_2$ . The classic Fabry-Perot cavity transmits wavelengths that are defined by the separation between the plates ( $d_{\text{cav}}$ ). The condition is  $d_{\text{cav}} = m\lambda_0 / (2n_{\text{cav}})$  for transmission through the cavity, where  $m$  is the longitudinal mode number,  $\lambda_0$  is the design wavelength,

and  $n_{cav}$  is the refractive index inside the cavity [25]. The transmissivity for these resonant wavelengths is very high ( $\sim 1$ ) if  $R_1 \approx R_2 \approx 1$ . The resonant condition is shown by Figure 17 where increasing reflectances on the mirrors create a higher Q (quality factor) cavity. The formula that describes the transmittance of a Fabry-Perot cavity with  $R_1 = R_2 = R$  is:

$$T = \frac{(1-R)^2}{(1-R)^2 + 4R \sin^2(\varphi)} \quad (\text{unitless}) \quad (15)$$

where  $\varphi$  as a function of the angle,  $\theta_{cav}$ , inside the cavity is given by

$$\varphi = \frac{2\pi}{\lambda} n_{cav} d_{cav} \cos \theta_{cav} \quad (\text{radians}) \quad (16)$$

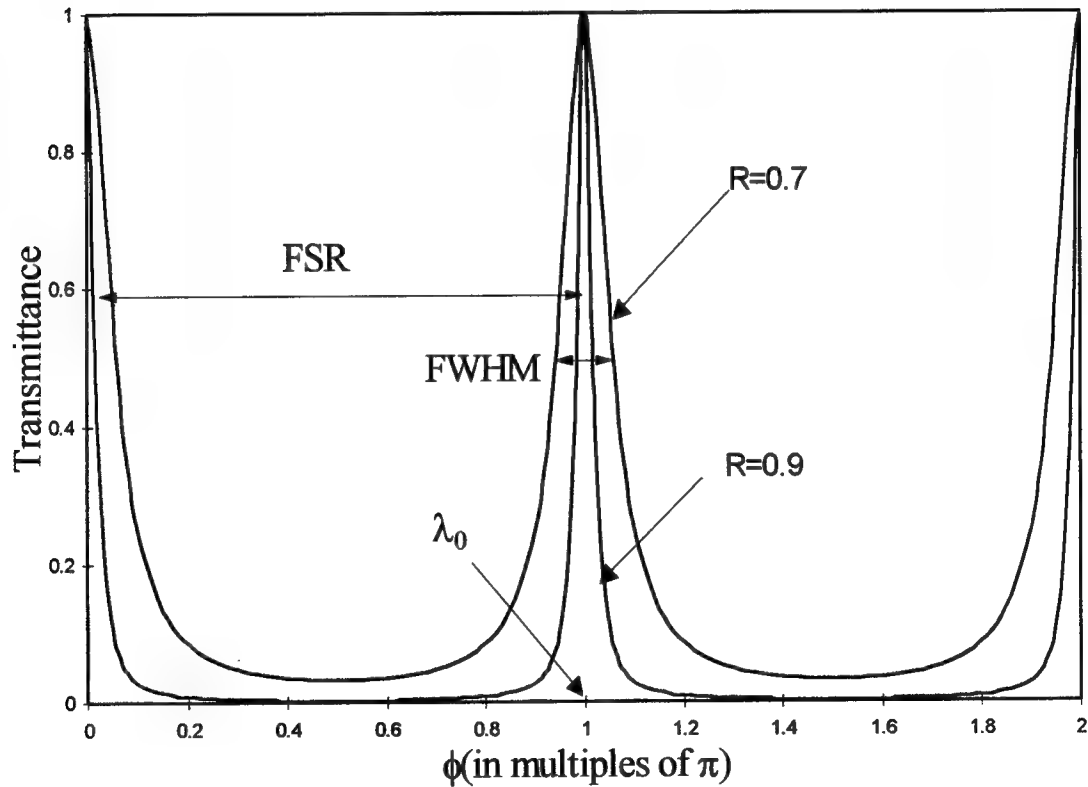


Figure 17. Transmittance characteristics of Fabry-Perot cavity

The free spectral range (FSR) is the distance in  $nm$  between the longitudinally propagating modes. The FSR is only affected by the mirror separation,  $n_{cav} d_{cav}$ . The full-width at half-maximum (FWHM) is defined as the wavelength spread,  $\Delta\lambda$ , about the design wavelength. The FWHM decreases for increasing reflectance of  $R_1$  and  $R_2$ . The cavity  $Q$  is the ratio of the FWHM to the design wavelength  $\lambda_0$ . Higher  $Q$  values mean greater mirror reflectances and narrower Fabry-Perot cavity transmission passbands as seen in Figure 17.

**2.2.1 RCLED Microcavity.** The RCLED Fabry-Perot cavity is formed by growing a DBR on a GaAs substrate, followed by an active optical cavity of an integral number of half Bragg wavelengths, and then another DBR. This is illustrated in Figure 18 where metal contacts with emission apertures have been placed on the upper DBR and a blanket metal has been put on the substrate to form an excitation current path. The cavity of the RCLED is referred to as a microcavity because its small size ( $\sim\lambda_0$ ) changes some of the characteristic Fabry-Perot parameters. [7; 8; 26; 27].

The resonant condition for a microcavity with DBRs is modified by the penetration depth of the electric field intensity into the DBR mirrors. The penetration depth is a parameter used to replace a distributed mirror structure having linear phase variation for changing frequency with a fixed phase mirror (Figure 19).

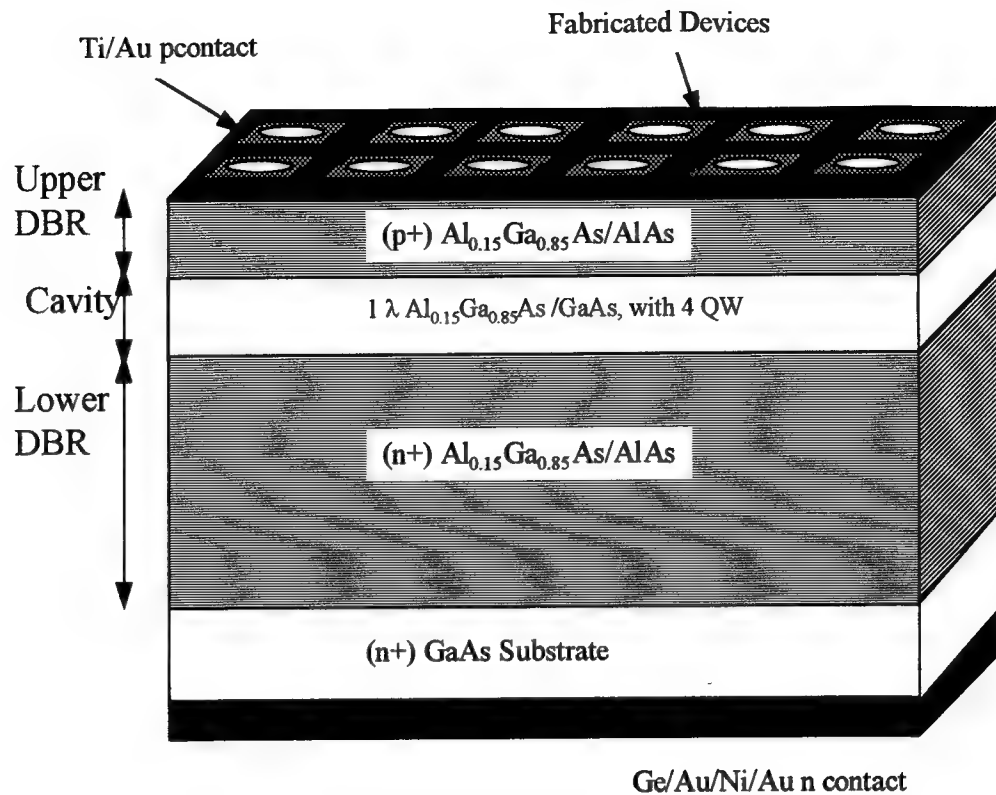


Figure 18. RCLED structure showing microcavity, DBRs, and devices (not to scale)

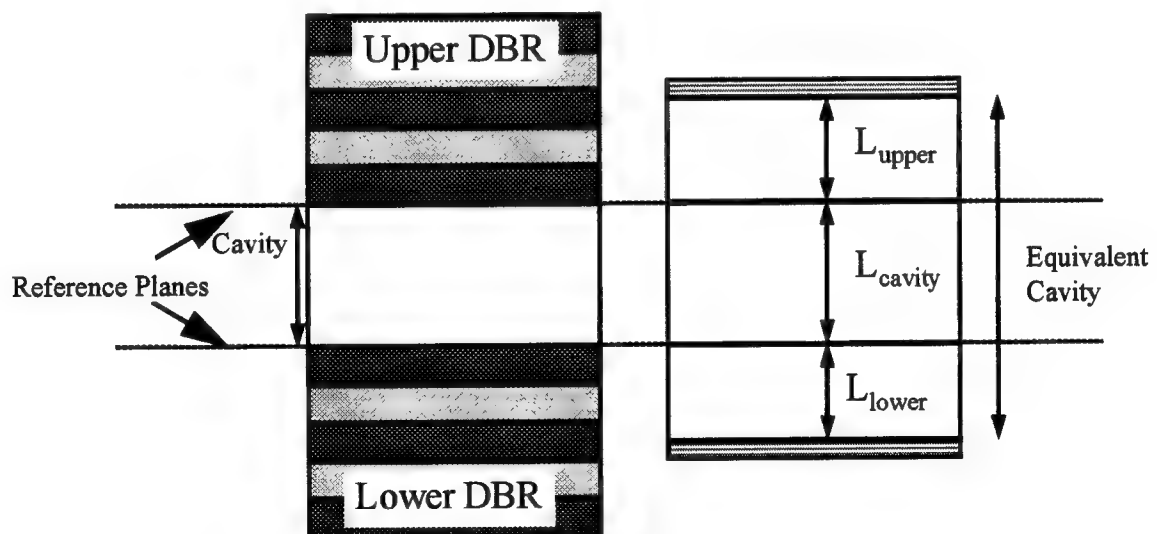


Figure 19. Penetration depth in distributed mirrors

The condition for the field reflected from the lower distributed mirror and the lower fixed mirror to have equal phase is given by [26]:

$$(\omega - \omega_0)\tau_r = \frac{2n\omega}{c}\Theta_0 \quad (\text{radians}) \quad (17)$$

given:

$$\Theta_0 = \omega_0\tau_r \quad (\text{radians}) \quad (18)$$

$$\tau_r = \frac{n_{cav} \tanh(\kappa l)}{c} l \quad (\text{radians}) \quad (19)$$

$$\omega_0 = 2\pi c / \lambda_0 \quad (\text{radians/sec}) \quad (20)$$

- $\kappa$  : coupling coefficient
- $\tau_r$  : DBR reflection delay
- $n_{cav}$  : effective refractive index of cavity
- $l$  : thickness of DBR structure
- $\Theta_0$  : the phase change at the fixed-phase mirror.

The resonant condition for the Fabry-Perot microcavity is that the wavefront phase be self consistent (equal) for a round trip in the cavity:

$$\frac{4\pi}{\lambda}(d_{eff}) - \Theta_{lower} - \Theta_{upper} = 2m\pi \quad (\text{radians}) \quad (21)$$

$$d_{eff} = n_{cav}d_{cav} + n_{upper}d_{upper} + n_{lower}d_{lower} \quad (nm) \quad (22)$$

where  $d_{upper}$  and  $d_{lower}$  represent the electric field intensity penetration depths into the upper and lower DBRs respectively. Equation 21 suggests that the new effective length of the microcavity should change the primary resonance condition (design wavelength). However, for a microcavity that is wavelength matched with the DBR (as in an RCLED)



this is not the case. The DBR always reflects it's design wavelength with either 0 or  $\pi$  phase change and this causes Equation 21 to give  $d_{cav} = d_{eff}$  at the design wavelength at normal incidence.

The characteristic narrowness of the spectral output of the RCLED is caused by the microcavity. Only certain modes propagate, and only those modes may be excited by the gain spectrum of the quantum wells. Therefore, it is essential to know the mode structure of the RCLED microcavity [9].

**2.2.2 RCLED Microcavity Parameters.** The mode structure of the microcavity is defined by it's characteristic parameters. That is, the quality  $Q$ , the Free Spectral Range  $FSR$ , the Finesse  $F$ , and the photon lifetime  $\tau_p$  in the cavity. Because of the distributed nature of DBRs, these characteristic parameters change for RCLEDs.

$$Q = \frac{\lambda_0}{\Delta\lambda} \quad (unitless) \quad (23)$$

$$FSR = \frac{c}{2n_{cav}d_{eff}} \cong \frac{\lambda_0^2}{2n_{cav}d_{eff}} \quad (nm) \quad (24)$$

$$F = \frac{FSR}{FWHM} = \frac{\lambda_0^2}{2n_{cav}d_{eff}\Delta\lambda} \quad (unitless) \quad (25)$$

$$\tau_p = \frac{Q\lambda_0}{2\pi c} = \frac{2n_{cav}d_{eff}}{c(1-R_1R_2)} \quad (sec) \quad (26)$$

### 2.3 Reflectance Calculations for RCLED

The Mathcad 5.0+® document used to calculate the reflectance spectra for this thesis uses a finite element approach to calculating device reflectance. Each quarter-wave ( $\lambda/4$ )

layer is broken into  $N_{\text{sublayer}}$  separate sublayers. More sublayers give greater accuracy in modeling the smooth compositional grading of the  $\lambda/4$  layers. However, increasing  $N_{\text{sublayer}}$  results in increased processing time. For this reason, the program breaks graded areas into sublayers, but treats the “plateaus” in the  $\lambda/4$  layers as a single sublayer (see Figure 20). The reflectance program using the Macleod matrix method makes the following assumptions about the multilayer device being modeled:

1. Non-magnetic materials
2. Smooth interfaces without scatter
3. Plane parallel layers with infinite lateral extent
4. Semi-infinite incident (air) and substrate (GaAs) media
5. Linear wave equation.

The program can handle arbitrary compositional grading with complex refractive index information. The condition for setting the thickness of the  $N_{\text{sublayer}}$  separate sublayers is a discrete form of Equation 11.

$$\sum_{r=1}^{N_{\text{sublayer}}} n_r(z)_{\lambda_0} d_r = \frac{\lambda_0}{4} \quad (nm) \quad (27)$$

where  $n_r(z)$  denotes the compositional grading in the growth direction,  $d_r$  is the sublayer physical thickness, and the subscript  $\lambda_0$  means the equation should be calculated at the design wavelength,  $\lambda_0$ . This ensures that each  $\lambda/4$  layer is the correct optical thickness at the design wavelength. The criteria for the optical cavity of the RCLED is

$$\sum_{r=1}^{N_{\text{cavity}}} n_r(z)_{\lambda_0} d_r = NUM \frac{\lambda_0}{2} \quad (nm) \quad (28)$$

where  $N_{cavity}$  is the number of sublayers modeled for the cavity and  $NUM$  is the width of the cavity in half-wavelengths.

The reflectance program listing is included in Appendix B.

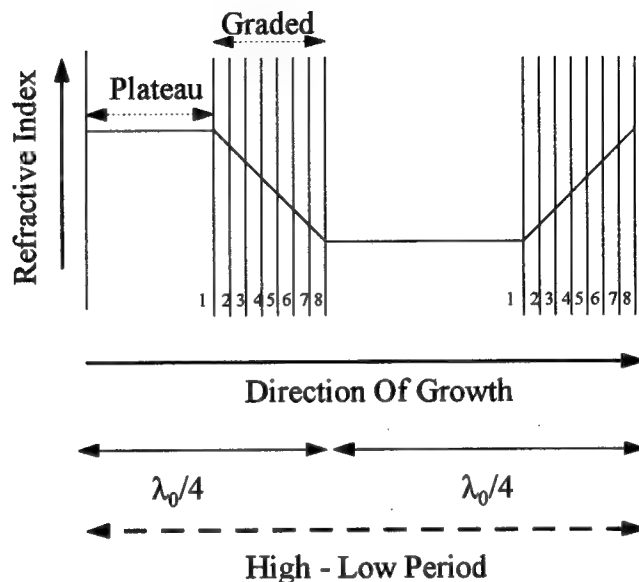


Figure 20. Scheme for dividing HL layers into sublayers in reflectance program

**2.3.1 Example Calculation.** Figure 21 shows the calculated reflectance pattern for an RCLED with 38 periods in the lower DBR, a cavity of 1 Bragg wavelength, and 6 periods in the upper DBR (Figure 18). The HL periods are composed of  $\text{Al}_{0.15}\text{Ga}_{0.85}\text{As}/\text{AlAs}$  with interfaces that are linearly graded over  $12\text{nm}$ . The reflectance of the upper DBR is less than that of the lower DBR in order to favor emission through the upper surface. The GaAs substrate is absorbing for wavelengths shorter than  $\lambda < \sim 870\text{nm}$ . As expected, the characteristic Fabry-Perot dip is seen to move toward decreasing wavelengths with increasing incidence angle.

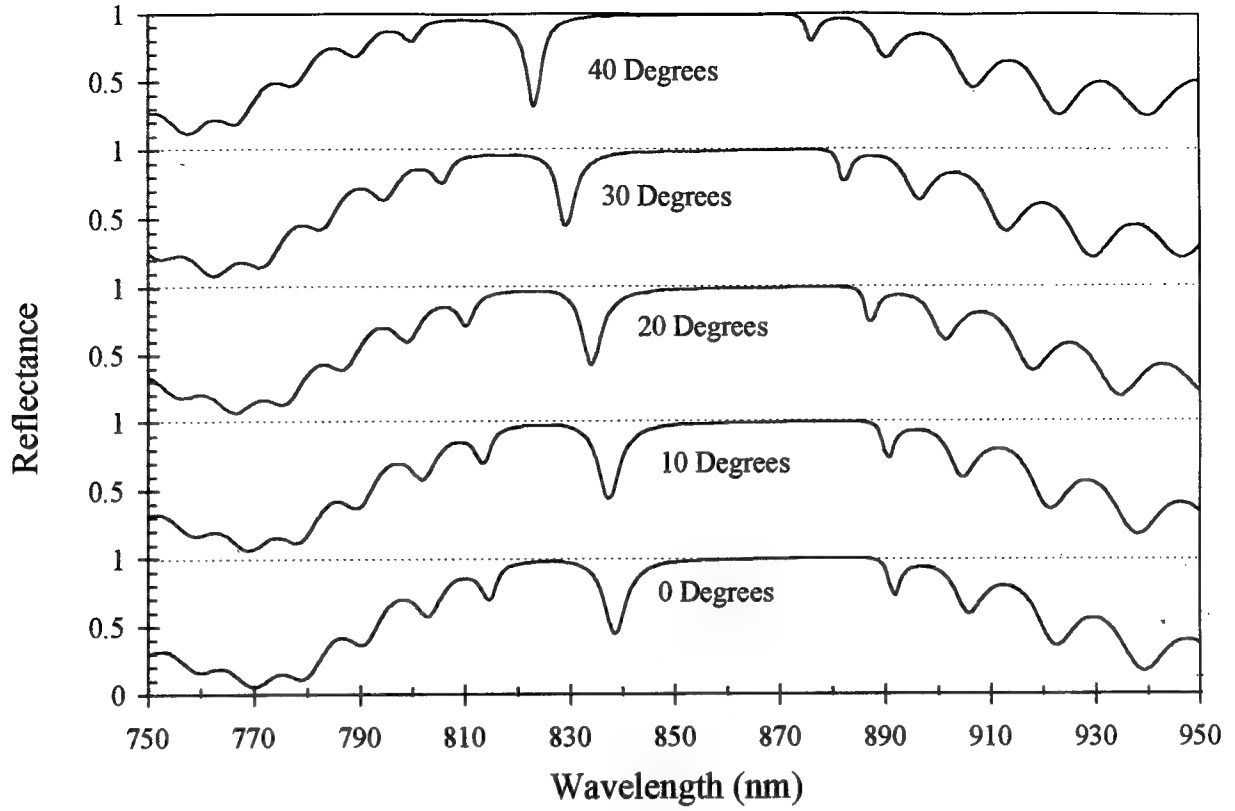


Figure 21. Reflectance spectrum of RCLED with 6 HL periods of  $\text{Al}_{0.15}\text{Ga}_{0.85}\text{As}/\text{AlAs}$  in the upper DBR, 38 HL periods of  $\text{Al}_{0.15}\text{Ga}_{0.85}\text{As}/\text{AlAs}$  in the lower DBR and a  $1\lambda$ , at  $\lambda_0 = 850\text{nm}$ , cavity (Calculated for TE polarization)

Compare the characteristics of a RCLED with a  $1\lambda$  cavity at  $850\text{nm}$  with  $n_{\text{cav}} = 3$  and  $R_{\text{upper}} = 0.5$ ,  $R_{\text{lower}} = 0.99$  to a typical He-Ne laser cavity with a  $20\text{cm}$  cavity at  $\lambda = 632.8\text{nm}$ ,  $n_{\text{cav}} = 1$ ,  $R_{\text{upper}} = 0.95$ , and  $R_{\text{lower}} = 0.99$ . The results are given in Table 2.

Table 2. Comparison of Selected Cavity Parameters.

	FSR	Finesse	Photon Lifetime
RCLED Cavity	425 nm	8.889	11.22 femto sec
HeNe Cavity	0.001 nm	102.422	22.41 nano sec

A major advantage of the RCLED is the width between the modes (FSR). For the He-Ne laser at  $632.80025\text{nm}$  the mode number,  $q$ , is 632,111 and at  $632.80125\text{nm}$   $q$  is 632,110. Therefore the gain spectrum is wide enough for many modes to propagate and multimode operation is the norm. For the RCLED at  $850\text{nm}$  the mode number  $q$  is 2. For  $q = 3$  the wavelength is  $566\text{nm}$ . Thus the RCLED is single mode because the microcavity formed by DBRs is wavelength dependent and does not reflect sufficiently at  $566\text{nm}$ , and the quantum well gain spectrum does not extend to  $566\text{nm}$ .

## 2.4 Quantum Well Layers

The last wavelength selection capability occurs inside the quantum well (QW) layers. Saleh and Teich describe a layer as being quantum in nature when it is “smaller than the de Broglie wavelength of a thermalized electron [28].” For the present study, quantum well layers must be 25nm thick, or less.

The wavelength of the light emitted from a semiconductor diode is dependent upon its energy bandgap. Quantum wells have discrete allowed carrier (electron and hole) energy levels in the direction of growth. These discrete levels mandate that electron-hole recombinations are only allowed for certain energies. Therefore the art of bandgap engineering (quantum tailoring) involves the exploitation of individual layers of atoms to realize properties that would not exist otherwise [29;30].

**2.4.1 Ternary and Quaternary Compound Materials.** Ternary (three element) and quaternary (four element) compound materials are used by device makers to realize desired energy bandgaps and lattice constants [15; 29].

Figure 22 shows the range of useful wavelengths that can be achieved by some compound materials. The object of interest to this thesis is the  $\text{Al}_x\text{Ga}_{1-x}\text{As}$  family, capable of

emitting light from  $0.7\mu\text{m}$  to  $0.9\mu\text{m}$  wavelength depending on the value of  $x$  ( $0 \leq x \leq 0.45$ ). The composition  $x$  is cutoff at 0.45 because  $\text{Al}_x\text{Ga}_{1-x}\text{As}$  becomes an indirect semiconductor. What makes these composite compounds so useful is that the energy bandgap may be changed *in situ* by varying the composition with time during growth.

**2.4.2 Allowed Energy Levels.** Figure 23 schematically shows the approximately parabolic shells that define the allowed energies of the quantum well electrons and holes close to the subband energy levels [28].

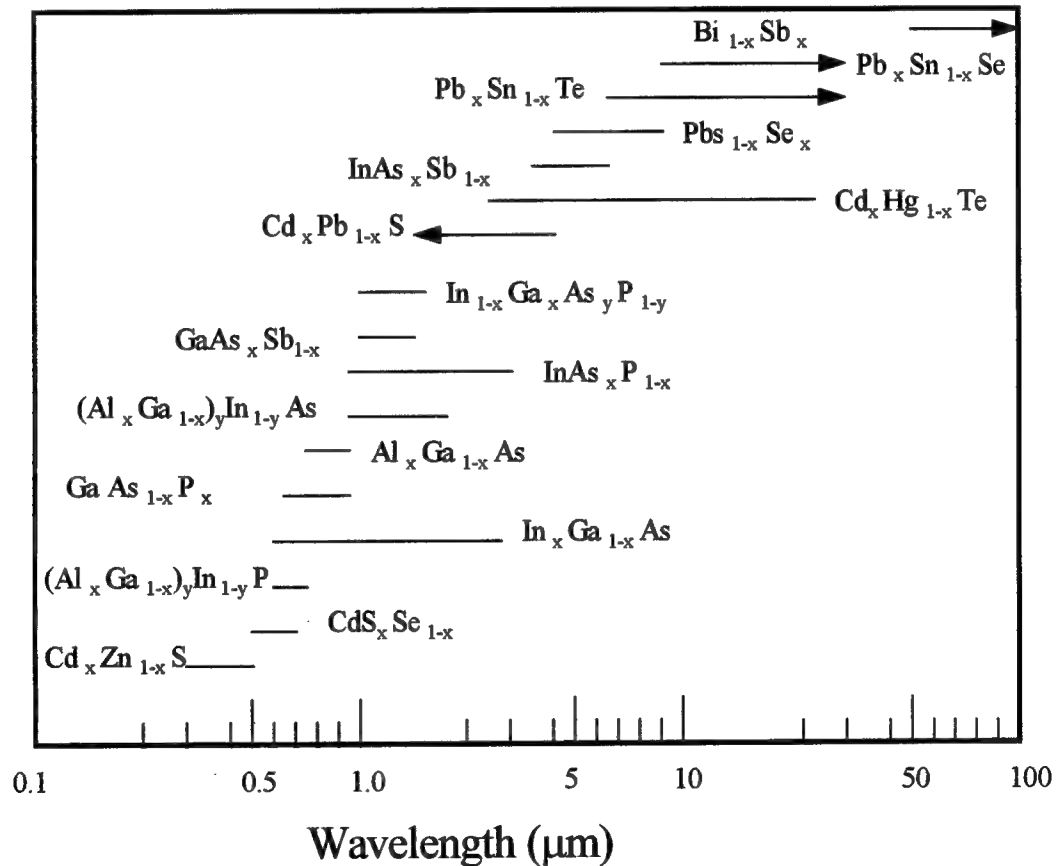


Figure 22. Range of possible emission wavelengths for selected compound semiconductors

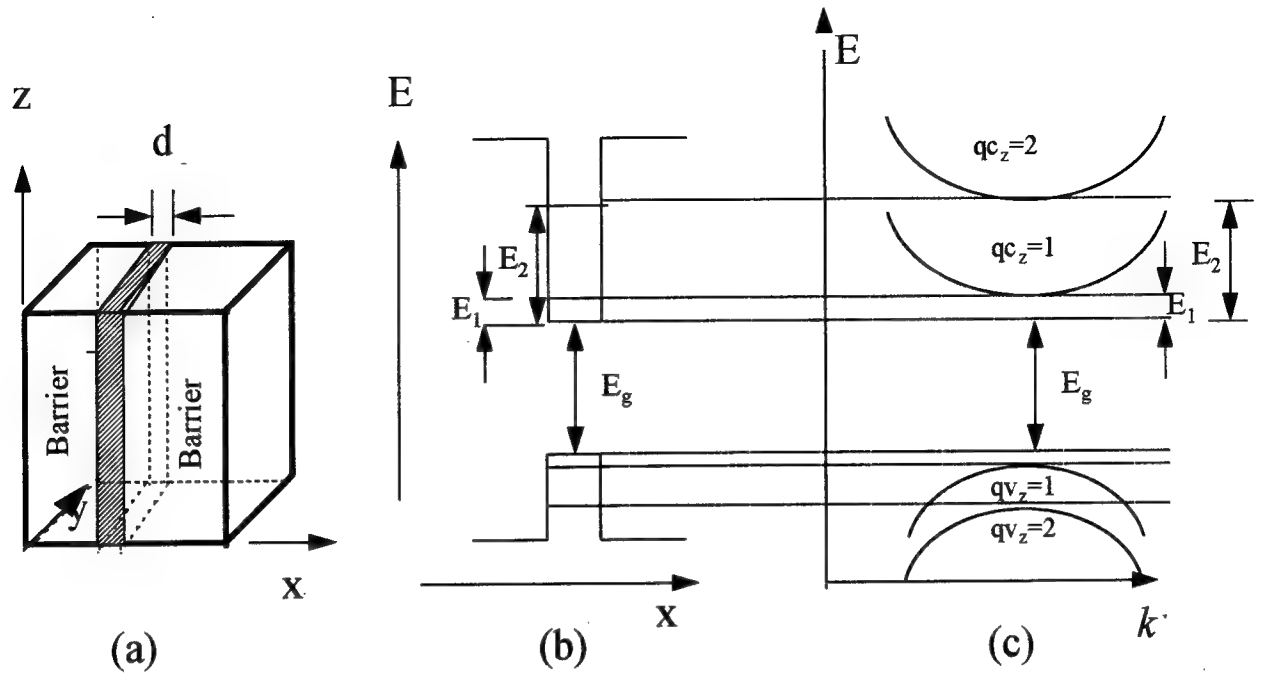


Figure 23. (a) Geometry of quantum well. (b) Energy level diagram for electrons and holes in quantum well. (c) Cross section of  $E$ - $k$  relation

In bulk material the  $E$ - $k$  (energy-momentum) relationships for electrons near the bottom of the conduction band and holes near the top of the valence band are given by

$$E = E_c + \frac{\hbar^2 k^2}{2m_c} \quad (\text{eV}) \quad (29)$$

$$E = E_v - \frac{\hbar^2 k^2}{2m_v} \quad (\text{eV}) \quad (30)$$

$$k^2 = k_x^2 + k_y^2 + k_z^2 \quad (\text{m}^{-2}) \quad (31)$$

where  $m_c$  and  $m_v$  are the effective masses in the conduction band and valence band respectively, and the subscripts  $\{x,y,z\}$  denote a coordinate system choice. In a quantum well the energy levels become discrete in the direction of growth, but remain continuous for

the transverse (x,y) directions (perpendicular to growth). The  $E-k$  relationships for the conduction and valence bands for the quantum well grown in the  $z$  direction are:

$$E_2 = E_c + E_{qc_z} + \frac{\hbar^2 k_{\perp}^2}{2m_c} \quad (eV) \quad (32)$$

$$E_1 = E_v - E_{qv_z} - \frac{\hbar^2 k_{\perp}^2}{2m_v} \quad (eV) \quad (33)$$

$$k_{\perp}^2 = k_x^2 + k_y^2 \quad (m^{-2}) \quad (34)$$

Therefore all electron-hole recombinations leading to photon emission are at energies defined by:

$$E_{\text{emission}} = E_2 - E_1 = E_{\text{gap}} + E_{q1c} + E_{q1v} + \frac{\hbar^2 k_{\perp}^2}{2m_r} \quad (eV) \quad (35)$$

where  $E_{\text{gap}}$  is the natural bandgap of the quantum well material and the reduced mass  $m_r$  is calculated using  $1/m_r = 1/m_c + 1/m_v$ . From Figure 23, electron-hole recombinations, which lead to photon emission, are not allowed at the bandgap energy in a quantum well, but must take place at a higher energy. The first allowed energy transition is between  $qc_z = 1$  in the conduction band and  $qv_z = 1$  in the valence band ( $q(c-v)_z = 1$ ). With careful selection of materials and QW geometry it is possible to choose emitted wavelength. Figure 24 shows the wavelength dependence versus well width of the  $q(c-v)_z = 1$  (electron - heavy hole) transition for a  $\text{Al}_x\text{Ga}_{1-x}\text{As}$  quantum well with a  $\text{Al}_{0.15}\text{Ga}_{0.85}\text{As}$  barrier region.



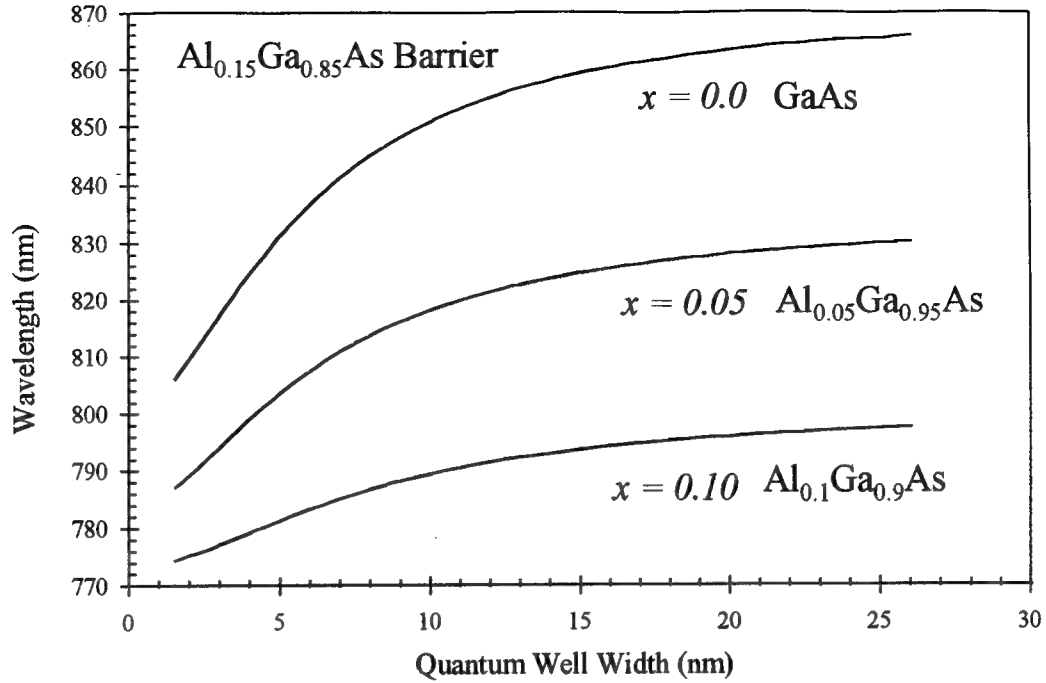


Figure 24. Dependence of emission wavelength on  $\text{Al}_x\text{Ga}_{1-x}\text{As}$  well width and aluminum content  $x$  with an  $\text{Al}_{0.15}\text{Ga}_{0.85}\text{As}$  barrier region

Figure 25 and Figure 26 show the wavefunctions describing the location of the carrier in the conduction and valence bands of the quantum well. The figures are calculated by solving the one-dimensional time-independent Schrödinger equation [19] for a  $15\text{nm}$  GaAs quantum well with  $\text{Al}_{0.3}\text{Ga}_{0.7}\text{As}$  barrier layers (Appendix C). There are 2 allowed electron levels, 7 allowed heavy hole levels (4 are shown) and 3 allowed light hole levels (none are shown). The probability of a transition between levels is proportional to the correlation of the energy level wave functions given by

$$P_{trans} \propto \int_{-\infty}^{\infty} \Psi_m(z) \Psi_n(z) dz \quad (\text{unitless}) \quad (36)$$

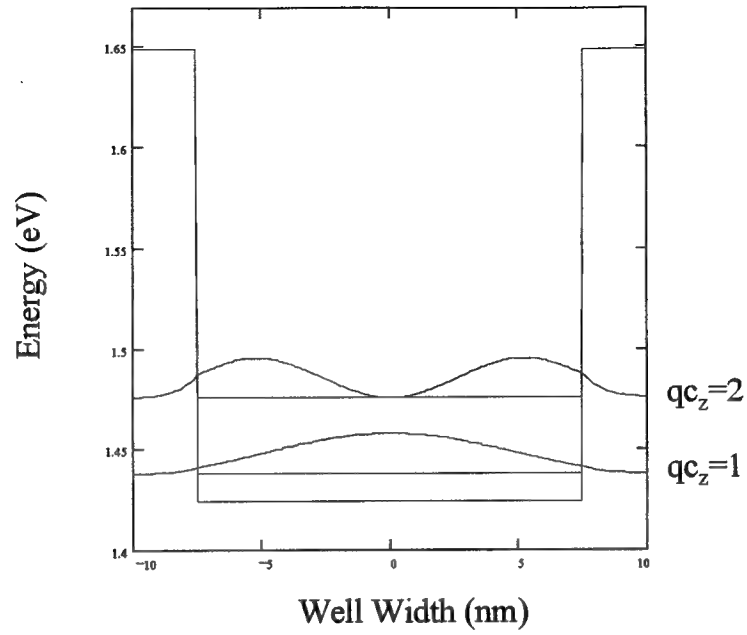


Figure 25. Wavefunctions of energy levels in conduction band calculated for a  $15\text{nm}$  GaAs quantum well with  $\text{Al}_{0.3}\text{Ga}_{0.7}\text{As}$  barrier layers

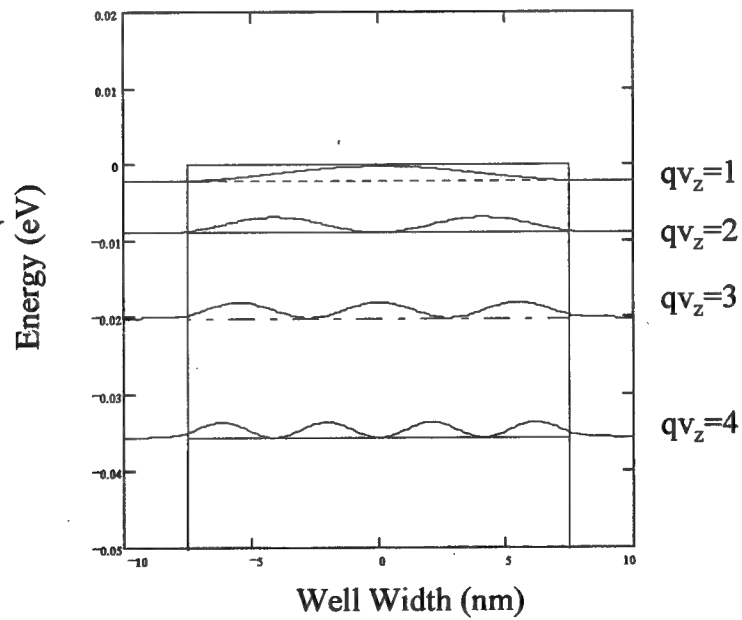


Figure 26. Wavefunctions of heavy hole energy levels in valence band calculated for a  $15\text{nm}$  GaAs quantum well with  $\text{Al}_{0.3}\text{Ga}_{0.7}\text{As}$  barrier layers

The wave functions are given by  $\Psi \propto \cos kz$  for odd energy levels (1, 2, 3...) and  $\Psi \propto \sin kz$  for even energy levels (2, 4, 6...) where  $k$  is the wave number of the energy level and  $z$  is the distance across the quantum well. Thus transitions between levels  $m$  and  $n$  are more likely for  $m = n$  than transitions between levels where  $m \neq n$ . For the purpose of this thesis, rigorous transition rules are applied.  $P_{trans}$  is assumed to be zero for  $m \neq n$  and only electron-heavy hole recombinations are considered. Electron-light hole recombinations are ignored in this thesis because they occur at different, higher energies and therefore will not be enhanced by the microcavity.

**2.4.3 Quantum Well Gain Spectrum.** The optical gain available to a photon of energy  $E$  in a quantum well is given by [28]:

$$g(E) = \frac{\lambda^2}{8\pi\tau_r} \rho(E) f_g(E) \quad (cm^{-1}) \quad (37)$$

- $\rho(E)$  is the 2D optical joint density of states
- $E$  is the photon energy
- $f_g(E)$  is the fermi inversion factor
- $\tau_r$  is the electron-hole recombination lifetime.

For a quantum well with  $i$  electron energy levels and  $j$  hole energy levels Equation 37 becomes [16;31].

$$g(E) = \frac{q^2 |M|^2}{E \epsilon_0 m_0^2 c_0 \hbar n L_z} \sum_{i,j} m_{i,j} C_{i,j} A_{i,j} [f_c - f_v] \Phi(E - E_{i,j}) \quad (cm^{-1}) \quad (38)$$

where

- $i, j$  are integers referring to the quantized electron, heavy hole, and light hole states respectively
- $E$  is the photon energy

- $|M|^2$  is the transition matrix element [31].
- $m_{r_{ij}}$  is the reduced mass of the  $i,j$  transition
- $C_{ij}$  is the strength, or degree of wavefunction correlation, of the  $i,j$  transition
- $A_{ij}$  accounts for the polarization dependence of the  $i,j$  transition
- $f_c$  and  $f_v$  are the Fermi-Dirac distribution functions for the conduction and valence bands
- $\Phi$  is the Heaviside step function  $\{\Phi(x) = 0, x < 1 \text{ and } 1, x \geq 0\}$ .
- $n$  is the effective group refractive index of the quantum well
- $L_z$  is the thickness of the quantum well.

In order to include the spectral broadening of each recombination transition due to interactions with phonons and other electrons, the gain expression (Equation 38) is convolved with the Lorentzian spectral lineshape function

$$L(E) \equiv \frac{1}{\pi} \frac{\hbar / \tau_{in}}{(E - \hbar\omega)^2 + (\hbar / \tau_{in})^2} \quad (eV^{-1}) \quad (39)$$

to get the final calculated gain

$$G(\hbar\omega) = \int_{-\infty}^{\infty} g(\hbar\omega - E_{trans}) L(E_{trans}) dE_{trans} \quad (cm^{-1}) \quad (40)$$

The optical gain for the RCLED depends on the quasi fermi levels,  $E_{fc}$  and  $E_{fv}$ , which are a function of carrier density in the well. The relationship between the carrier densities;  $N_{electrons}$ ,  $P_{holes}$ , and the energy difference between the  $i_{th}$  quantized electron/hole energy level and the quasi-fermi levels, assuming parabolic  $E-k$  bands, is given by:

$$N_{electrons} = \frac{4\pi k_B T}{h^2 L_z} \sum_i m_{e_i} \ln\{1 + \exp(-(E_{q_i} - E_{fc}) / k_B T)\} \quad (cm^{-3}) \quad (41)$$

$$P_{holes} = \frac{4\pi k_B T}{h^2 L_z} \sum_{k=lh, hh} \sum_i m_{k_i} \ln\{1 + \exp(-(E_{v_i} - E_{f_v}) / k_B T)\} \quad (cm^{-3}) \quad (42)$$

where  $L_z$  is the width of the quantum well. For this thesis charge neutrality is assumed and  $N_{electrons} = P_{holes}$ . Given  $N_{electrons}$  and  $P_{holes}$ , Equations 41 and 42 may be solved for the quasi-fermi levels.  $E_{fc}$  and  $E_{fv}$  are then put back into the gain equation and used to determine  $G(\hbar\omega)$ .

Figure 27 shows the calculated gain for an 8nm GaAs quantum well with  $Al_{0.15}Ga_{0.85}As$  barrier layers (same parameters as Figure 25). As stated before only the  $q(c-v)_z=1$  electron to heavy hole transition is being considered as contributing to the gain.

The width of the gain spectrum is defined as the energy difference between the  $q(c-v)_z=1$  electron to heavy hole transition and the separation of the quasi-fermi levels. Put another way, the quantum wells provide gain for photon energies in the range

$$E_1 < E < E_{fc} - E_{fv} \quad (eV) \quad (43)$$

where  $E_1$  is the transition energy for  $q(c-v)_z = 1$ .

**2.4.4 Quantum Well Rate of Spontaneous Emission.** The spectral rate of spontaneous emission from the quantum well is the summation over all possible energies of the product of the transition probability density, the emission probability, and the 2D optical density of states that can interact with the photon [28].

$$R(E) = \frac{1}{\tau_r} \rho(E) f_e(E) \quad (J^{-1}cm^{-3}sec^{-1}) \quad (44)$$

- $\rho(E)$  is the 2D optical joint density of states
- $E$  is the photon energy

- $f_e(E)$  is the probability of photon emission
- $\tau_r$  is the electron-hole recombination lifetime.

The rate of spontaneous emission from a quantum well, in accordance with Equation 44, is given by

$$R(E) = \frac{q^2 n E |M|^2}{\epsilon_0 m_0^2 c^3 \hbar^4 L_z} \sum_{i,j} m_{i,j} C_{i,j} A_{i,j} f_c (1 - f_v) \Phi(E - E_{i,j}) \quad (J^{-1} cm^{-3} sec^{-1}) \quad (45)$$

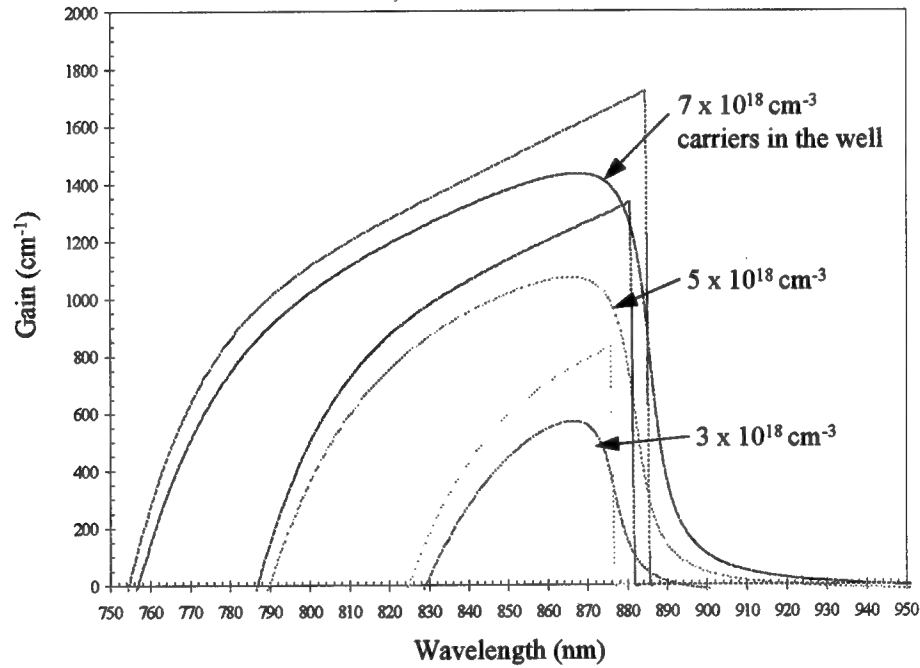


Figure 27. Gain for 8nm GaAs quantum well with a  $Al_{0.15}Ga_{0.85}As$  barrier layers for various well carrier concentrations showing both calculated (sharp) and convolved (smoothed) spectra at  $T=300K$

To obtain the spontaneous emission at a given photon energy Equation 45 must be convolved with the Lorentzian line-shape function as before. The quasi fermi levels are calculated as before. In the RCLED microcavity, it is the spontaneous rate of emission that is modified by the microcavity. This can also be thought of as modification of the spontaneous emission lifetime by the microcavity.

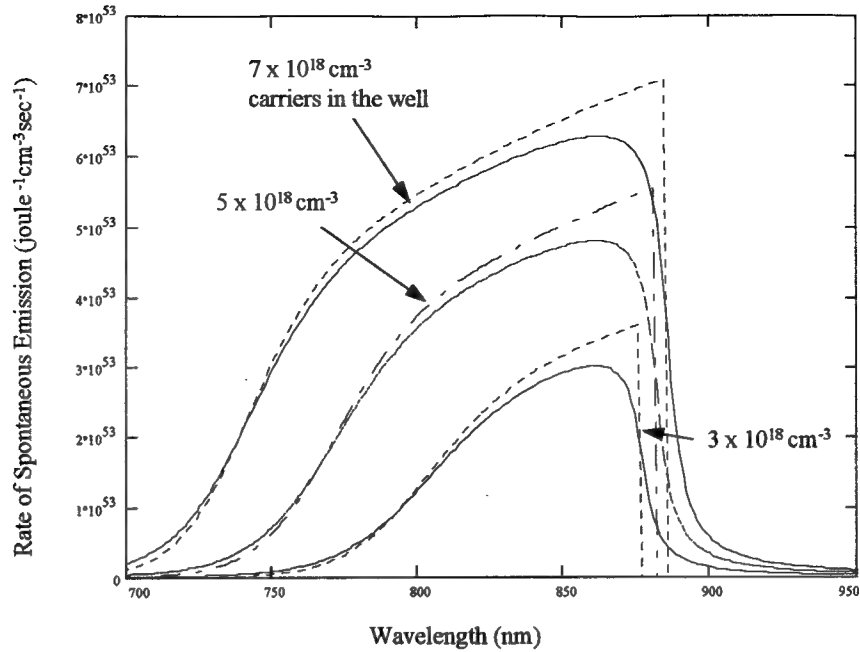


Figure 28. Spontaneous emission rates for a 8nm GaAs quantum well with  $\text{Al}_{0.15}\text{Ga}_{0.85}\text{As}$  barrier layers for various well carrier concentrations showing both calculated (sharp) and convolved (smoothed) spectra at  $T=300\text{K}$

## 2.5 The RCLED Structure

The Fabry-Perot microcavity and the quantum well layers work together to select the emitted wavelength of the RCLED. The next step is to examine some parameters that affect the RCLED.

**2.5.1 Spontaneous Emission Enhancement Factor  $\Xi$ .** The spontaneous emission enhancement factor,  $\Xi$ , of a microcavity is the ratio of the spectral output of a dipole emitting into a microcavity to a dipole emitting into a bulk medium.  $\Xi$  describes the modification of the emission due to the longitudinal mode structure of the microcavity. An electron-hole recombination may be considered as the source of coherent wave-packets emitted in opposite directions. These wave packets evolve independently upon reflection leading to interference outside the microcavity. The complex reflectivity of the electric field

at a DBR is quantified by the amplitude modifier  $\rho$  and the phase change  $\theta$ , where  $0 \leq \rho \leq 1$  and  $0 \leq \theta \leq 2\pi$ . The incident and reflected E-fields are related by:

$$E_{\text{reflected}} = \rho e^{j\theta} E_{\text{incident}} \quad (46)$$

$\Xi$  is derived in Chapter 3 but is shown here for completeness.  $\Xi$  as a function of wavelength at  $0^\circ$  incidence is given by:

$$\Xi(\lambda) = \frac{|E_{\text{emitted}}|^2}{|E_{\text{qw}}|^2} = \frac{(1 - R_1) \left( 1 + R_2 + 2\sqrt{R_2} \cos\left(\frac{4\pi}{\lambda} n_{\text{cav}}(d - d_1) + \theta_2\right) \right)}{1 + R_1 R_2 - 2\sqrt{R_1 R_2} \cos\left(\frac{4\pi}{\lambda} n_{\text{cav}} d + \theta_1 + \theta_2\right)} \quad (47)$$

- $R_1$  is the reflectance of the upper DBR
- $R_2$  is the reflectance of the lower DBR
- $n_{\text{cav}}$  is the refractive index of the cavity
- $d$  is the width of the cavity
- $d_1$  is the distance between the quantum wells and the upper DBR
- $\theta_1$  is the phase change upon reflection by  $R_1$
- $\theta_2$  is the phase change upon reflection from  $R_2$
- $|E_{\text{qw}}|^2$  is the intensity of the E-field emitted by the quantum well layers.
- $|E_{\text{emitted}}|^2$  is the intensity of the E-field emitted from the RCLED.

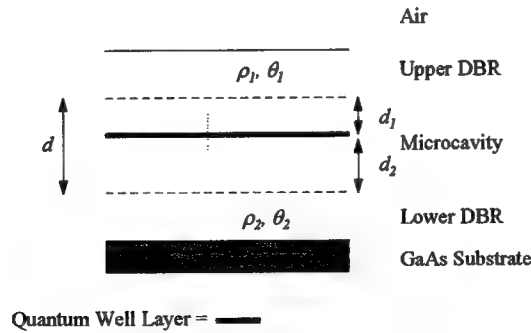


Figure 29. Graphic representation of architecture for  $\Xi$  in Equation 47, only normal propagation is considered here



**2.5.2 Electric Field Intensity in the Cavity.** The electric field confinement factor is a measure of how much the electric field overlaps the quantum well layers. The figure of merit for vertical structures, such as an RCLED, is the longitudinal confinement factor (along the direction of growth)  $\Gamma_z$ .  $\Gamma_z$  is given by:

$$\Gamma_z = \frac{\int_{Active} E^2(z) dz}{\int_d E^2(z) dz} \quad (\text{unitless}) \quad (48)$$

where  $d$  is equal to the cavity width and *Active* denotes the extent of the quantum wells. Thus the comparison is made with the effective coupling between the energy in the cavity and the energy in the quantum wells. Higher confinement factors mean greater efficiency and lower losses in the cavity. Figure 30 and Figure 31 show the calculated electric field intensity in a RCLED with a  $1\lambda$  optical cavity. The RCLED is designed for operation at  $\sim 850nm$ . Clearly the RCLED will not work well at  $825nm$ .

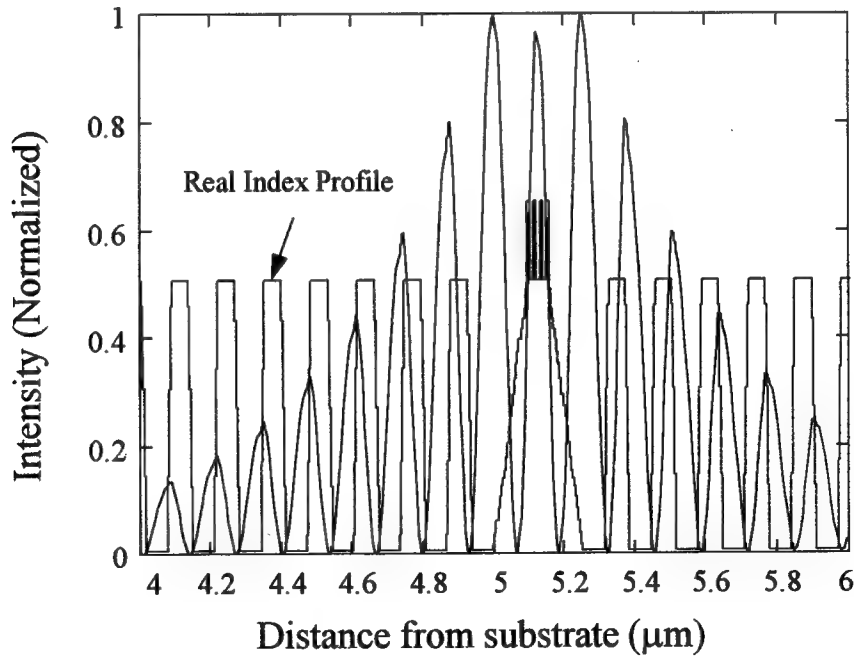


Figure 30. Normalized electric field intensity inside RCLED plotted against distance from substrate for  $\lambda = 841nm$

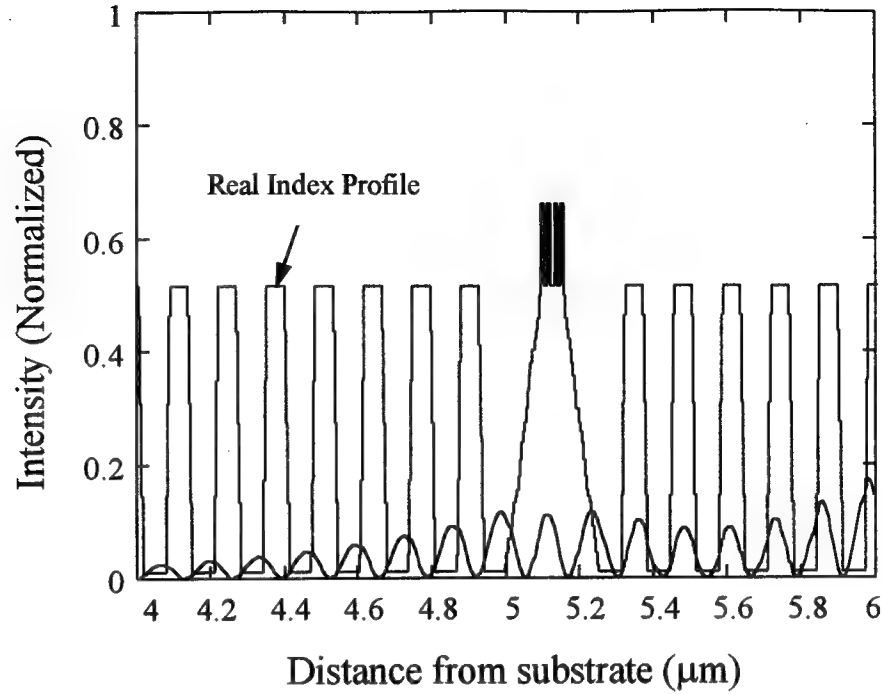


Figure 31. Normalized electric field intensity inside RCLED plotted for against distance from substrate  $\lambda = 825 \text{ nm}$

**2.5.3 RCLED Losses.** For stimulated emission to occur, gain in the cavity must overcome losses due to absorption, mirror transmittance and other sources. The threshold gain necessary for lasing in vertical devices is given by [32]:

$$g_{th} \Gamma_z d_{cav} = \alpha_i L + \alpha_m L_m + \alpha_{oc} (d_{oc} - L) - \frac{1}{2} \ln(R_1 R_2) \quad (\text{unitless}) \quad (49)$$

$$\alpha_i = \alpha_a \Gamma_z + \alpha_{scat} + (1 - \Gamma_z) \alpha_p \quad (\text{cm}^{-1}) \quad (50)$$

- $\Gamma_z$  is the longitudinal confinement factor
- $g_{th}$  is the threshold gain
- $d_{cav}$  is the width of the cavity
- $L$  is the gain length (sum of width of quantum wells)
- $\alpha_m$  is the scattering/absorption loss within the DBRs
- $L_m$  is the penetration depth into the DBRs
- $\alpha_{oc}(d_{oc}-L)$  accounts for absorptive losses in the passive region of the cavity
- $\alpha_a$  is the free carrier loss within the quantum wells

- $\alpha_p$  is the free carrier loss within the passive layers
- $\alpha_{scat}$  is scattering loss throughout the cavity due to sidewall roughness
- $\ln(R_1 R_2)$  accounts for losses due to mirror transmittance

Given that the only major difference between the RCLED and the VCSEL is the upper mirror reflectance,  $\ln(R_1 R_2)$  is the most important term in comparing these similar devices. An example is an RCLED and a VCSEL each with lower mirror reflectance  $R_2 \sim 0.999$ . The VCSEL has upper mirror reflectance  $R_1 = 0.95$  while the RCLED has  $R_1 = 0.5$ . Both have the same microcavity architecture and the same number of quantum wells. Therefore in Equation 49 all cavity and scattering losses are presumed equal, as is the longitudinal confinement factor. This reduces Equation 49 to:

$$\frac{g_{thVCSEL}}{g_{thRCLED}} = \frac{1}{2} (\ln(R_1 R_2)_{VCSEL} - \ln(R_1 R_2)_{RCLED}) \quad (unitless) \quad (51)$$

Using the numbers in the scenario the RCLED has **3.116** times the threshold gain necessary for lasing as the VCSEL. This implies that the RCLED will lase only if the upper DBR reflectance is increased.

## 2.6 Summary

Chapter 2 presents all of the basic theory behind the Resonant Cavity Light-Emitting Diode in a piecewise fashion. The physics of the basic RCLED components are examined separately. In a real device all of these components must be designed, and built, to work together at the design wavelength. Component integration is the focus of Chapters 3 and 5.

### 3. Designing The RCLED

#### 3.1 Introduction

In order to examine and quantify the effects of a microcavity on the spectral emission properties of a light-emitting diode the individual components of the RCLED must be examined separately. Two devices were designed for this purpose. The first device consisted of a microcavity deposited on a GaAs substrate. This device gave the unenhanced emission spectrum of a microcavity with four quantum wells,  $E_{qw}$ . The second device has complete upper and lower DBRs and is a true RCLED. The emission spectrum,  $E_{emitted}$ , is enhanced by the microcavity and the location of the quantum wells.

By comparing emission spectra from each device the effects of enhancement of the microcavity formed by the two DBRs may be examined. The goal of this chapter is to quantify that change in a meaningful manner. Both devices are shown in Figure 32.

#### 3.2 Structure 1: The Cavity

Figure 33 shows the as-grown composition profile for Structure 1. The cavity contains four  $8nm$  wide GaAs quantum wells separated by  $10nm$   $Al_{0.15}Ga_{0.85}As$  barrier layers. The barrier layers are wide enough that negligible coupling occurs between quantum wells. The absorptive and gain effects of the quantum wells are assumed to be four times that of a single one (i.e. uniform carrier injection in every quantum well).

Note that Structure 1 has a single quarter-wave layer above and below the cavity. This is in order to properly define a separate confinement heterostructure for the quantum well active region. The energy levels of a single  $8nm$  GaAs quantum well surrounded by  $Al_{0.15}Ga_{0.85}As$  barrier layers are shown in Figure 34. For the purposes of this thesis only interactions between the electron level and the first allowed heavy hole level are considered (i.e.  $e1 \rightarrow hh1$ ). Figure 34 was generated using the material parameters in Table 3, where  $m_0$  is the mass of an electron.  $E_{trans}$ , the calculated transition energy for Figure 34, is  $1.458 eV$  or  $850nm$ . Figure 35 shows the calculated gain spectrum for the four quantum wells as a function of wavelength for various carrier densities. Figure 36 shows the calculated rate of spontaneous emission versus energy for various carrier densities, assuming uniform charge distribution in the quantum well. Figure 36 represents the expected unenhanced spontaneous emission from the microcavity. The smoother curve in Figure 35 and Figure 36 has been convolved with the Lorentzian function to approximate intra-band scattering effects.

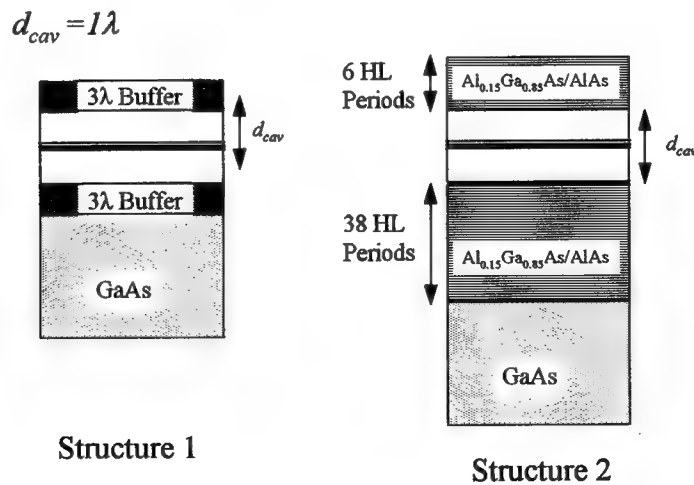


Figure 32. Schematic of RCLED structures

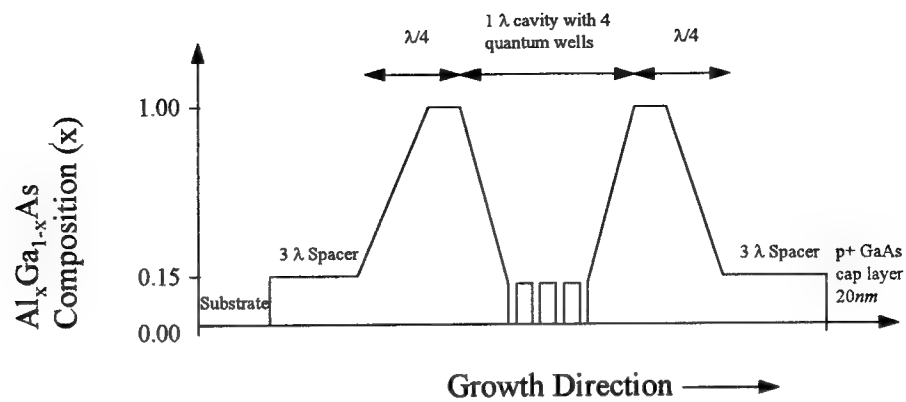


Figure 33. Composition diagram of Structure 1

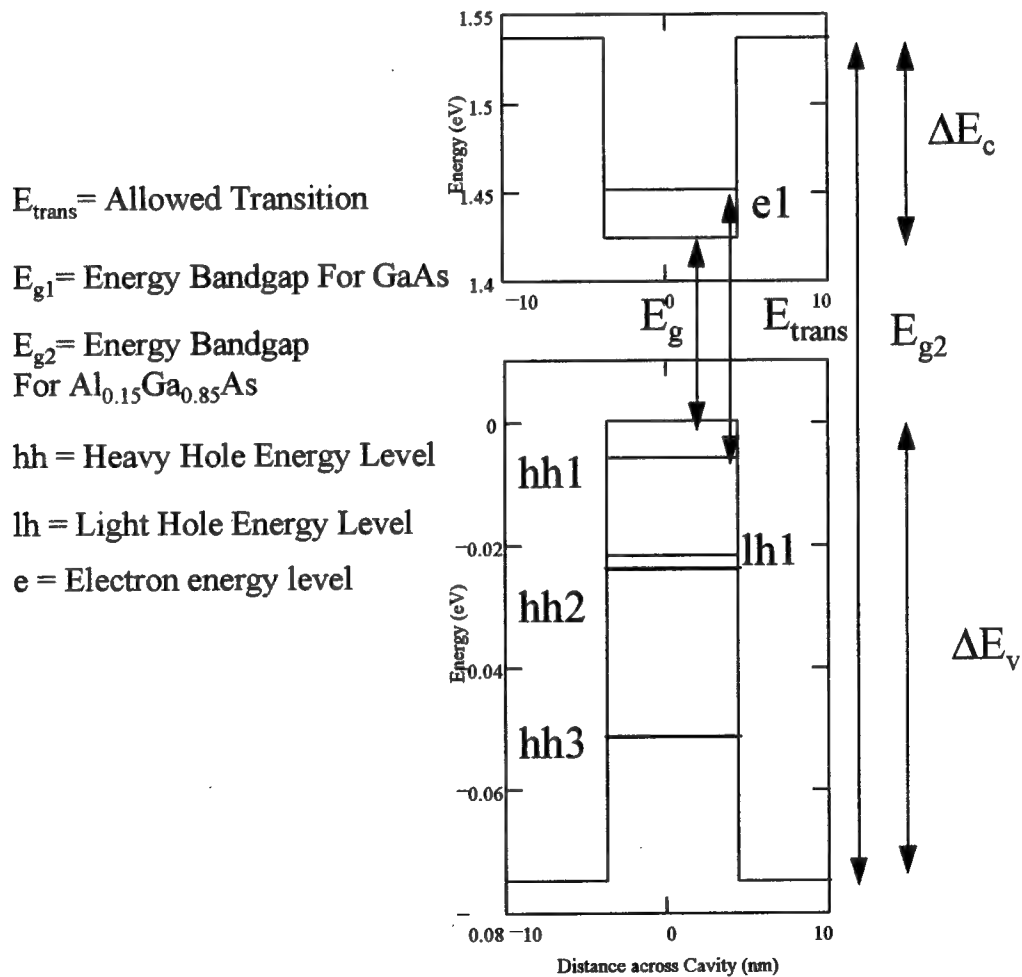


Figure 34. Calculated allowed energy levels for quantum wells of Structure 1 at T=300K

Table 3. Material parameters for Figure 34

	in well	in barrier
Mass of electron	$0.067m_0$	$0.079m_0$
Mass of heavy hole	$0.62m_0$	$0.641m_0$
Mass of light hole	$0.087m_0$	$0.096m_0$
Energy Levels	eV	
$\Delta E_c$	0.122	
$\Delta E_v$	0.075	
$E_{g1}$	1.424	
$E_{g2}$	1.536	

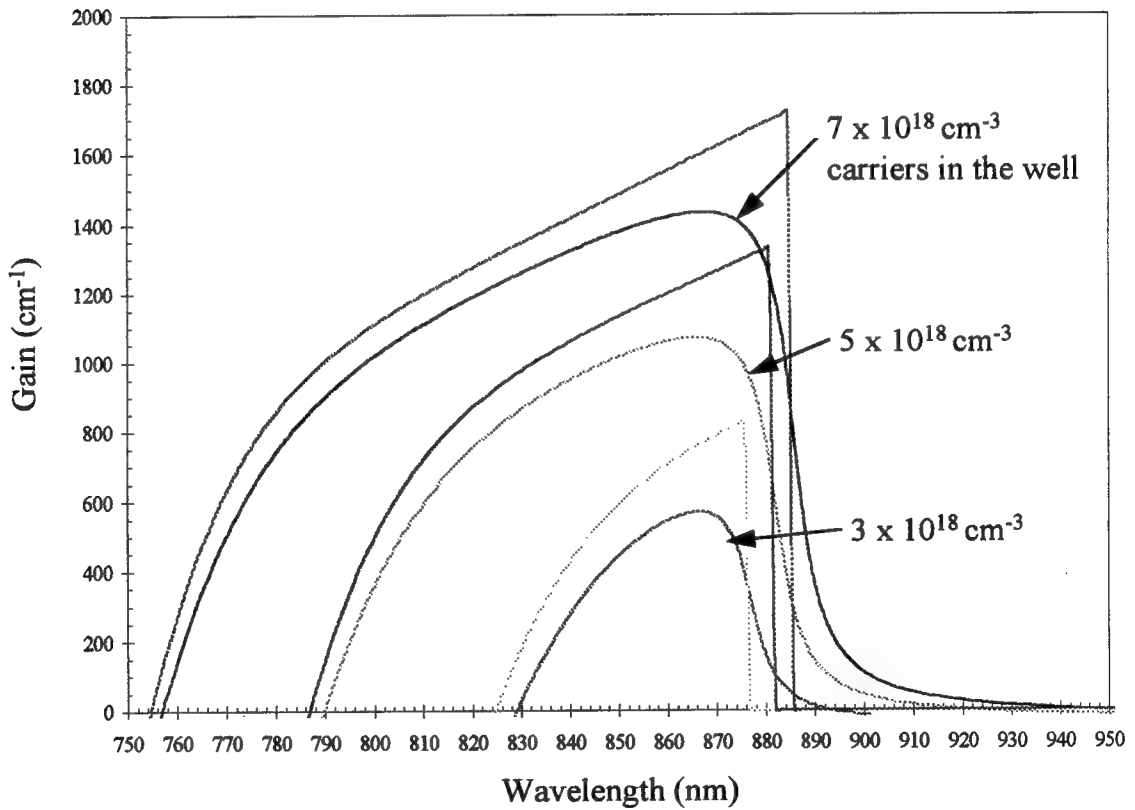


Figure 35. Calculated gain of an 8nm GaAs quantum well surrounded by 10nm Al<sub>0.15</sub>Ga<sub>0.85</sub>As barrier layers

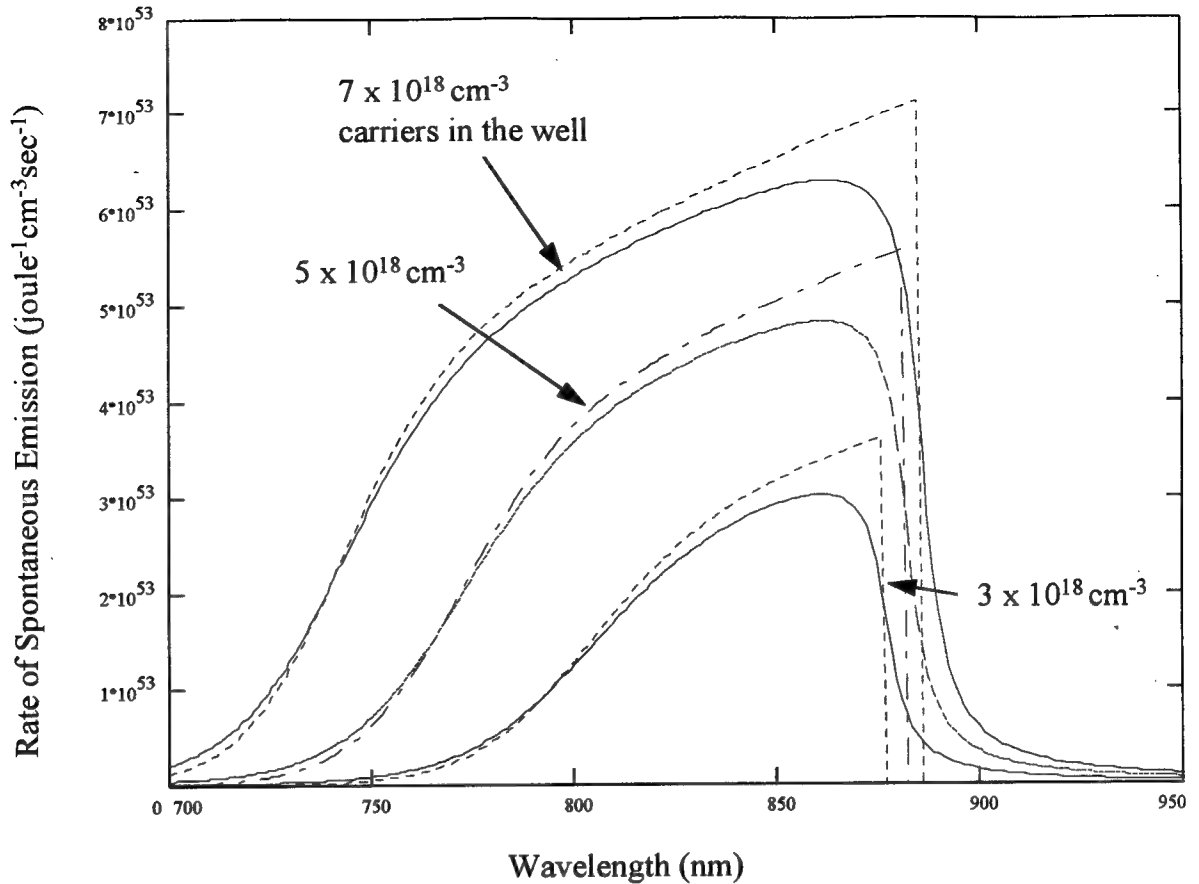


Figure 36. Calculated rate of spontaneous emission of an  $8\text{nm}$  GaAs quantum well surrounded by  $10\text{nm}$   $\text{Al}_{0.15}\text{Ga}_{0.85}\text{As}$  barrier layers

Figure 35 and Figure 36 were calculated with Mathcad using the document in Appendix C and the equations presented in Chapter 2.4.

### 3.3 Structure 2: The Cavity with Upper and Lower DBRs (RCLED)

In Structure 2 the resonant cavity is fully formed with the inclusion of upper and lower linearly graded DBRs. The composition diagram of Structure 2 is shown in Figure 37. Figure 38 shows the calculated normal incidence reflectance and phase (with absorption) for the RCLED structure in Figure 37. An interesting feature is the blue-shifting of the Fabry-Perot dip predicted by the model from the as-designed



wavelength of  $850nm$  to  $839nm$ . The blue-shifting occurs because of the choice of periodic structure of the HL layers. By making the cavity  $2.2\lambda$  the dip can be red-shifted back to  $850nm$ , if desired.

Figure 39 shows the normal incidence reflectance and phase calculated without absorptance. The most obvious difference is in the minimum value of the dip. The absorptance causes a perceived lower reflectance on the lower mirror. This is due to less photons being reflected due to absorption. Therefore the dip is lower with included absorptance. The linear phase region used by Corzine and Babic and described in Chapter 2 is clearly seen between  $830nm$  and  $850nm$  in both figures.

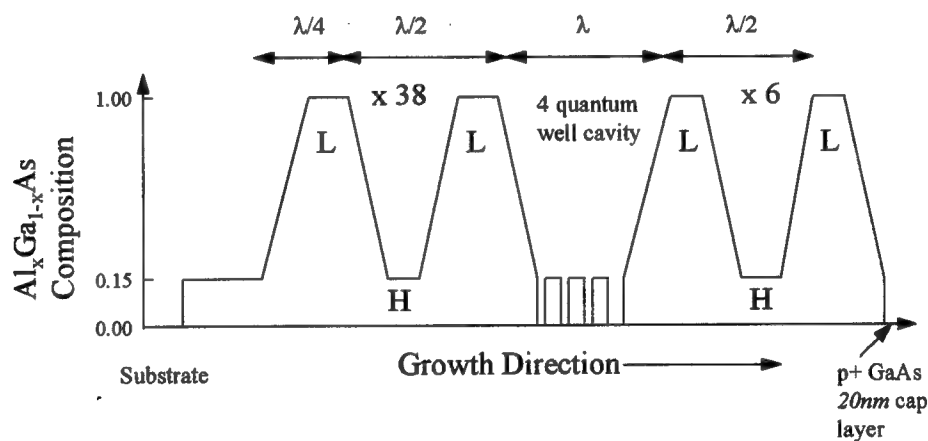


Figure 37. Composition diagram for Structure 2

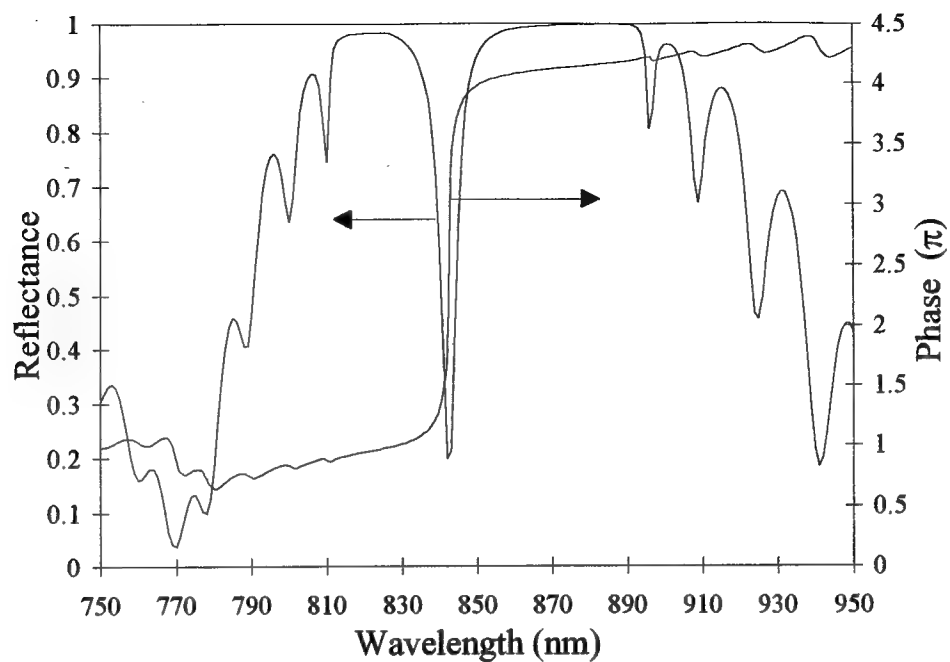


Figure 38. Calculated reflectance and phase spectra for Structure 2, including absorption. ( $\kappa \neq 0$ )

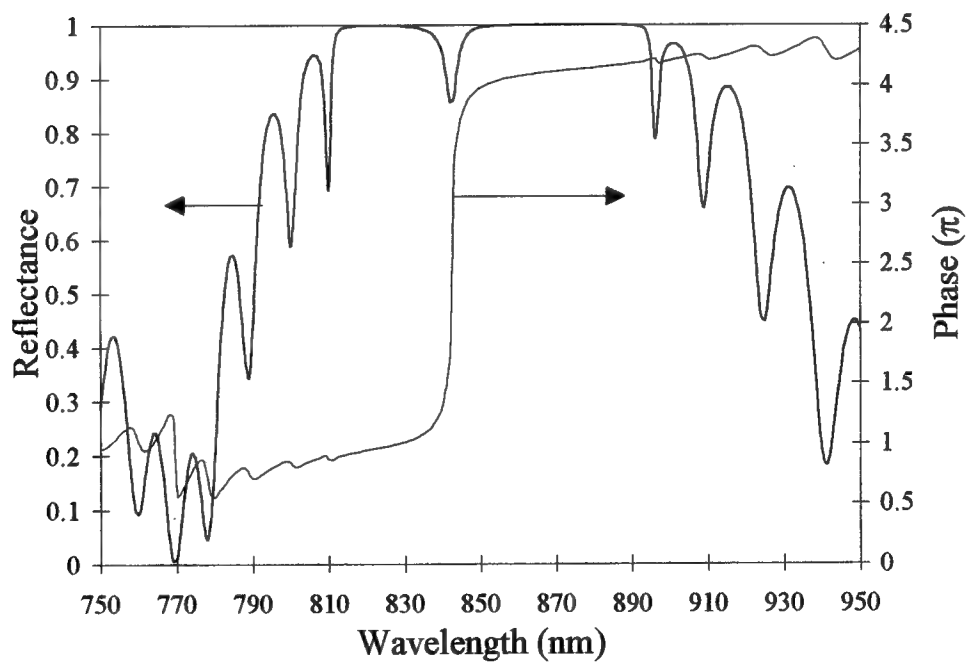


Figure 39. Calculated reflectance and phase spectra for Structure 2, not including absorption. ( $\kappa = 0$ )

Figure 40 shows an example of the linear periodic grading schemes that can be used in the HL half wave DBR layers. If Scheme 1 is used, the Fabry-Perot dip blue-shifts, unless the cavity is extended. If Scheme 2 is used the Fabry-Perot dip is at the design wavelength. Figure 41 shows the refractive index profile at  $\lambda_0 = 850nm$  for Structure 2 using grading Scheme 1. The cavity region and a single HL layer on either side of the cavity are shown. The cavity contains four quantum wells. The stepped profile designates the sublayers used in the Mathcad calculation.

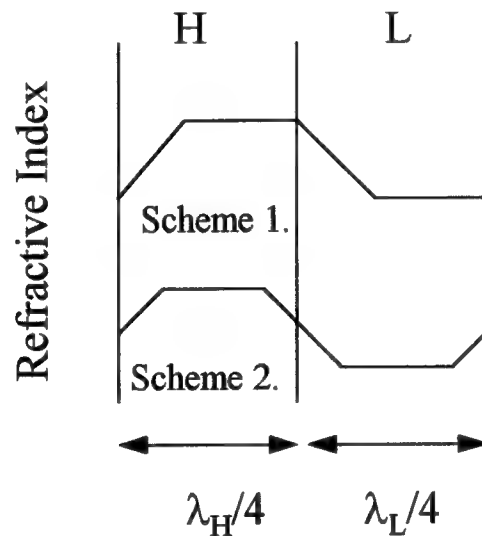


Figure 40. Example periodic grading schemes of high-low index layers

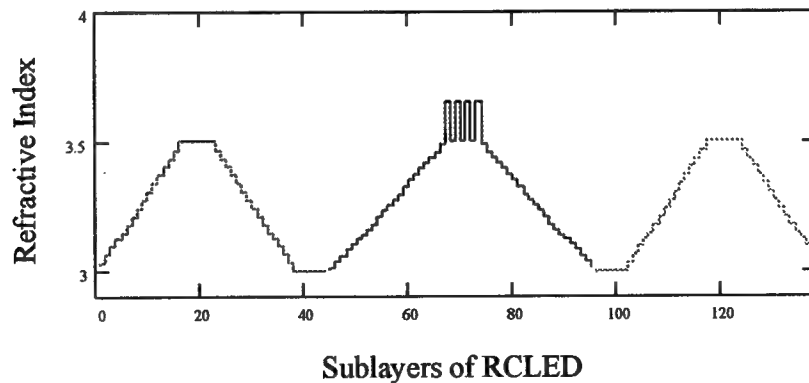


Figure 41. Actual refractive index profile of Structure 2 at  $\lambda_0 = 850nm$  used in reflectance program

Figure 42 shows the reflectance of the upper and lower DBRs seen from inside the microcavity looking out for TE Polarization.

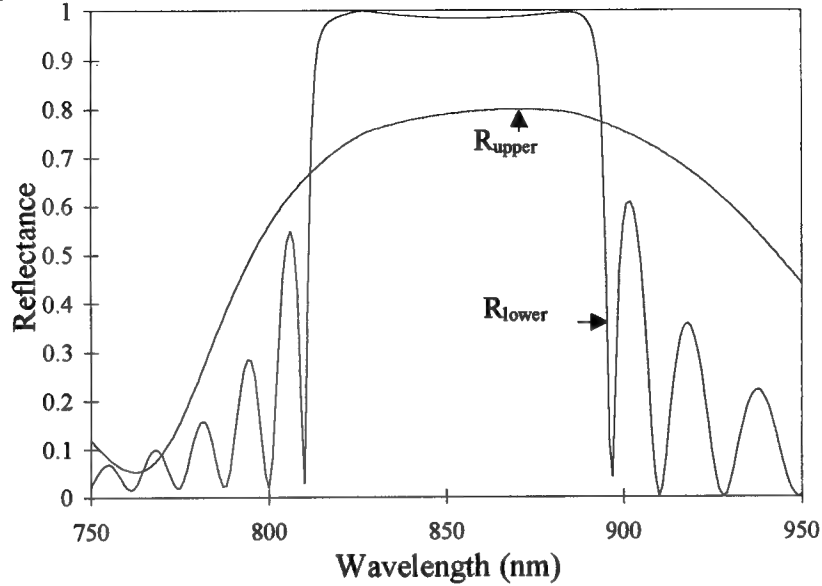


Figure 42. Calculated reflectance spectra for upper and lower DBRs of Structure 2 at 0° incidence angle

### 3.4 The Spontaneous Emission Enhancement Factor: $\Xi$

In Chapter 2 it is stated that the threshold gain necessary for stimulated emission is not achievable due to the low reflectance of the upper DBR. However, the presence of the microcavity does change the spontaneous emission profile in a measurable way. The spontaneous emission is enhanced or diminished depending on the location of the quantum well with respect to the resonant standing wave anti-nodes of the microcavity. This change is characterized by the spontaneous emission enhancement factor derived here using a classical wave interference model.

Presented here, for the first time, is the inclusion of angular dependency in  $\Xi$ . The angular dependence represents the angular sensitivity of the spectral

enhancement of  $\Xi$ . As the angle from the normal increases, shorter wavelengths will be enhanced and the peak wavelength of the emitted light blue-shifts.

**3.4.1 Derivation of  $\Xi$ .** Figure 43 shows the architecture used to derive  $\Xi$ . The microcavity contains a layer of emitters located at  $d_1$  from the upper DBR. This is the QW layer. Multiple QWs are assumed thin enough to be considered as a single layer, although in the device the QW layer may take up as much as 25% of the thickness of the cavity. For example, in a RCLED emitting at  $850nm$ , a  $1\lambda$  cavity is  $274nm$  thick, using  $n_{cav} \approx 3.1$ . A RCLED with four QWs, each  $8nm$  wide with 3 barriers of  $10nm$  represents a layer  $72nm$  thick. In this study, the finite thickness of the QWs is not considered. The QWs are assumed to be represented by a layer of infinitesimal width in the cavity.

The DBRs have complex reflectivity  $\rho_1 e^{j\theta_1}$  and  $\rho_2 e^{j\theta_2}$  which contain amplitude and phase information necessary for calculating reflected fields. The emitted radiation is examined using a classical wave interference model.

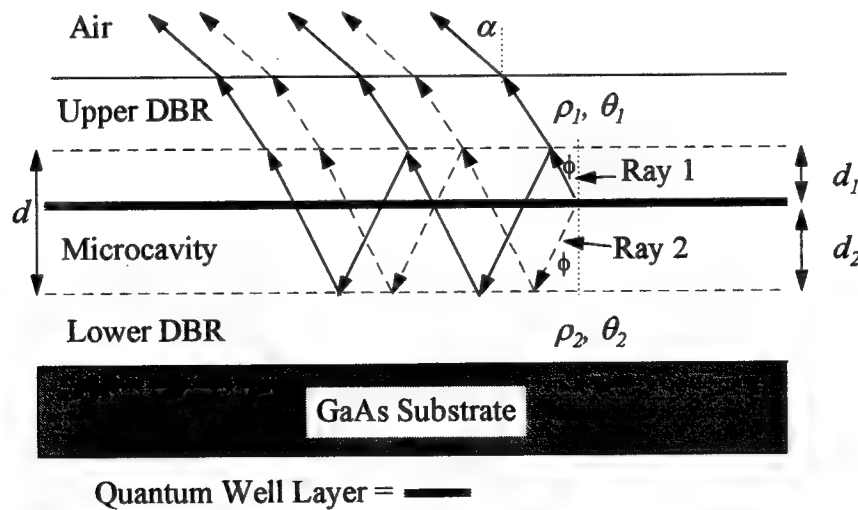


Figure 43. Graphic representation of architecture for  $\Xi$

For emission at an angle  $\phi$ , two rays may be considered to propagate. Ray 1 (denoted by the solid arrow in Figure 43) is directed up towards the upper DBR and is partially reflected and partially transmitted by that DBR. Ray 2 (denoted by the dashed arrow in Figure 43) is directed down towards the lower DBR and is partially reflected and partially transmitted by that DBR. Subsequent reflections and transmissions through the upper DBR for both rays are also shown in Figure 43.

To analyze the microcavity the relative phase differences between the ray and its reflections ( $\delta_{upper}$ ) and the second ray and its reflections ( $\delta_{lower}$ ) must be accounted for. Then the relative phase difference between Ray 1 and Ray 2 is needed in order to interferometrically sum their fields. The relative phase differences, ( $\delta_{upper}$ ) and ( $\delta_{lower}$ ), are equal for both rays. They will now be referred to as  $\delta_l$  which is given in Equation 52 as a function of  $\lambda$ , the emitted wavelength, and  $z$ , the growth direction. The functional dependence on the growth direction,  $z$ , is due to the cavity grading shown in Figure 37.

$$\delta_l(\lambda, z) = \frac{4\pi}{\lambda} n(\lambda, z) d \cos(\phi) \quad (radians) \quad (52)$$

The modified E-field spectrum,  $E_1$ , for Ray 1 in a microcavity is given by:

$$E_1(\lambda) = \tau_1 E_{qw} + \tau_1 \rho_2 \rho_1 E_{qw} e^{-i\delta_1} + \dots + \tau_1 (\rho_2 \rho_1)^n E_{qw} e^{-ni\delta_1} \quad (Volts/m) \quad (53)$$

where  $\tau_1$  is the transmissivity through the upper DBR,  $E_{qw}$  is the unmodified E-field spectrum, and  $n$  denotes the number of reflections. By summing  $n$  over infinity  $E_1$  becomes:

$$E_1(\lambda, z) = \tau_1(\lambda) E_{qw}(\lambda) \frac{1}{1 - \rho_2(\lambda) \rho_1(\lambda) e^{-i \delta_1(\lambda, z)}} \quad (\text{Volts/m}) \quad (54)$$

The E-field due to Ray 2 is also modified and becomes  $E_2$  given by:

$$E_2(\lambda) = \tau_1 \rho_2 E_{qw} + \tau_1 \rho_2 \rho_1 \rho_2 E_{qw} e^{-i \delta_1} + \dots + \tau_1 (\rho_1 \rho_2)^n E_{qw} e^{-ni \delta_1} \quad (\text{Volts/m}) \quad (55)$$

which reduces to:

$$E_2(\lambda, z) = \tau_1(\lambda) \rho_2(\lambda) E_{qw}(\lambda) \frac{1}{1 - \rho_2(\lambda) \rho_1(\lambda) e^{-i \delta_1(\lambda, z)}} \quad (\text{Volts/m}) \quad (56)$$

The relative phase difference,  $\delta_{rel}$  between Ray 1 and Ray 2 is given by:

$$\delta_{rel}(\lambda, z) = \frac{4\pi}{\lambda} n(\lambda, z) d_2 \cos(\phi) \quad (57)$$

where  $d_2$  is the distance from the QW layer in RCLED to the lower DBR. Using  $\delta_{rel}$

the modified E-fields may be summed interferometrically to obtain the output

E-field measured at the surface of the RCLED,  $E_{emitted}$ .

$$E_{emitted}(\lambda, z) = E_1(\lambda) + E_2(\lambda) e^{-i \delta_{rel}(\lambda, z)} \quad (58)$$

$$E_{emitted}(\lambda, z) = \tau_1 \frac{1 + \rho_2 e^{-i \delta_{rel}(\lambda, z)}}{1 - \rho_1 \rho_2 e^{-i \delta_1}} E_{qw}(\lambda) \quad (59)$$

The output intensity is proportional to the modulus squared of the output E-field,  $E_{emitted}$ . The ratio of  $|E_{emitted}|^2$  to  $|E_{qw}|^2$  represents the Spontaneous Emission Enhancement Factor,  $\Xi$ , due to the microcavity and, for emission through  $R_1$ , is given by:

$$\Xi(\lambda, z) = \frac{|E_{emitted}|^2}{|E_{qw}|^2} \quad (60)$$

which, after substitution, becomes:

$$\Xi(\lambda, z) = \frac{|\tau_1|^2 \left( 1 + |\rho_2|^2 + 2|\rho_2| \cos \left( \theta_2(\lambda) - \frac{4\pi}{\lambda} n(\lambda, z)(d - d_1) \cos \phi \right) \right)}{1 + |\rho_1|^2 |\rho_2|^2 - 2|\rho_1||\rho_2| \cos \left( \theta_1(\lambda) + \theta_2(\lambda) - \frac{4\pi}{\lambda} n(\lambda, z)d \cos \phi \right)} \quad (61)$$

For the case of no absorption in the cavity or the DBRs, the transmission,  $|\tau_1|^2$ , through the upper DBR is equal to  $(1 - R_1)$  and Equation 60 becomes:

$$\Xi(\lambda, z) = \frac{(1 - R_1(\lambda)) \left( 1 + R_2(\lambda) + 2\sqrt{R_2(\lambda)} \cos \left( \theta_2(\lambda) - \frac{4\pi}{\lambda} n(\lambda, z)(d - d_1) \cos \phi \right) \right)}{1 + R_1(\lambda)R_2(\lambda) - 2\sqrt{R_1(\lambda)R_2(\lambda)} \cos \left( \theta_1(\lambda) + \theta_2(\lambda) - \frac{4\pi}{\lambda} n(\lambda, z)d \cos \phi \right)} \quad (62)$$

where  $R_1$  and  $R_2$  are the reflectances of the upper and lower DBRs respectively.

**3.4.2 Applying  $\Xi$ .** The angle  $\phi$  in Equation 60 must be referenced to the output angle measured from the surface of the RCLED,  $\alpha$ . Using Snell's Law for refractive indices:

$$n_{air} \sin \alpha = n_{qw} \sin \phi \quad (63)$$

where  $n_{qw}$  is the refractive index of the quantum well layer of the cavity and  $n_{air} = 1$ .

Now substituting back into Equation 60:

$$\Xi(\lambda) = \frac{(1 - R_1) \left( 1 + R_2 + 2\sqrt{R_2} \cos \left( \theta_2 - \frac{4\pi n(z)}{\lambda(n_{qw})} (d - d_1) (n_{qw}^2 - \sin^2 \alpha)^{1/2} \right) \right)}{1 + R_1 R_2 - 2\sqrt{R_1 R_2} \cos \left( \theta_1 + \theta_2 - \frac{4\pi n(z)}{\lambda(n_{qw})} d (n_{qw}^2 - \sin^2 \alpha)^{1/2} \right)} \quad (64)$$



Equation 64 includes absorption in the DBRs, but not in the cavity. Note that  $(R_1, \theta_1)$  and  $(R_2, \theta_2)$  must be calculated from the viewpoint of the quantum well layer inside the cavity. This requires reversing the order of the matrix multiplication outlined in Chapter 2 for  $R_1$ . Figure 42 shows calculated upper and lower reflectance spectra for Structure 2. There is no dependency on carrier injection level included in  $\Xi$ , therefore the customary widening of the emission spectrum with increasing injection seen in a conventional LED is not expected.

**3.4.3 Examining the Effects of  $\Xi$ .** Figure 44 shows the blue shifting of  $\Xi$  with increased angle from the normal. The displayed angle is referenced to the emission angle from the surface of  $R_1$  (the upper DBR). The blue-shifting has a cosine dependence as seen in Equation 60. The wavelength dependent reflectance and phase change of Structure 2 are calculated using the Mathcad document in Appendix B. The graphic insert shows the location of the QW layer in the cavity. Figure 45 shows the calculated  $\Xi$  (normalized) with calculated reflectance spectra of Structure 2 at  $0^\circ$  and  $40^\circ$ . The spontaneous enhancement is predicted to occur at the Fabry-Perot dip. Figure 46 shows the effect of placing the QW layer at a node of the resonant mode located at  $\lambda/4$  from the lower DBR. Emission through  $R_1$  is greatly inhibited as compared to Figure 44 where the QW layer is placed at a cavity anti-node. Figure 47 shows the effect of placing the QW layer at a node of the microcavity located  $\lambda/4$  from the upper DBR. Again the spontaneous emission is inhibited greatly compared to Figure 44.

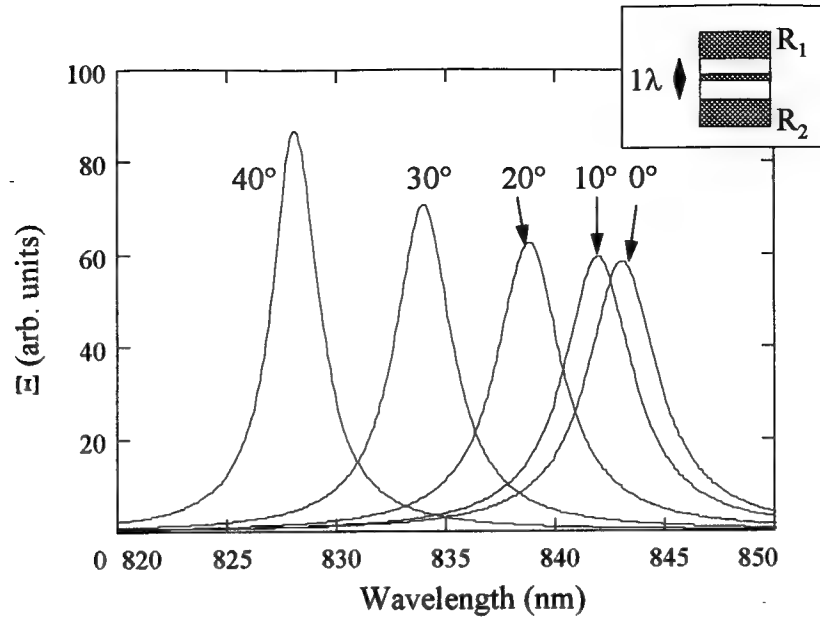


Figure 44.  $\Xi$  for Structure 2 with quantum well located at the center of the cavity (TE polarized)

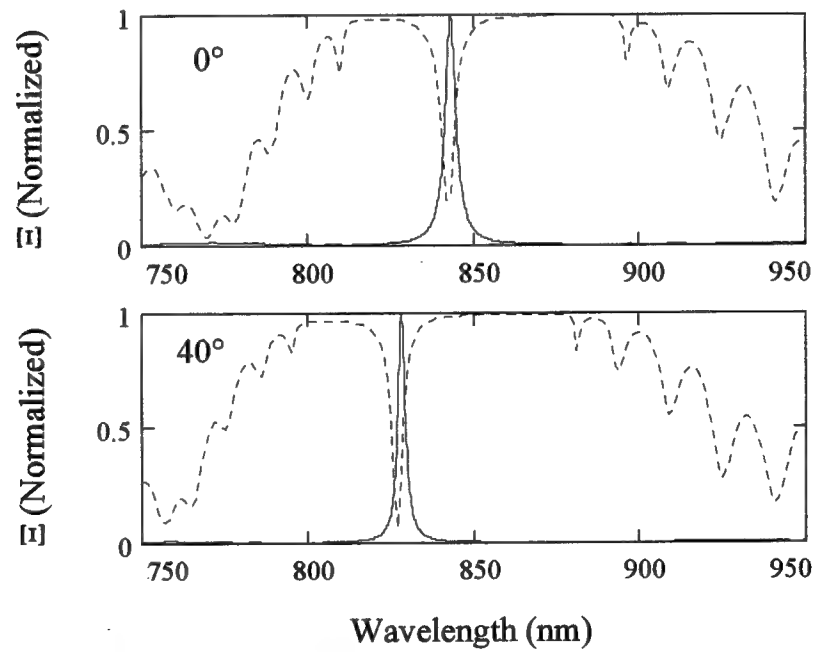


Figure 45. Normalized  $\Xi$  for Structure 2 at  $0^\circ$  and  $40^\circ$  with calculated reflectance spectrum (TE polarized)

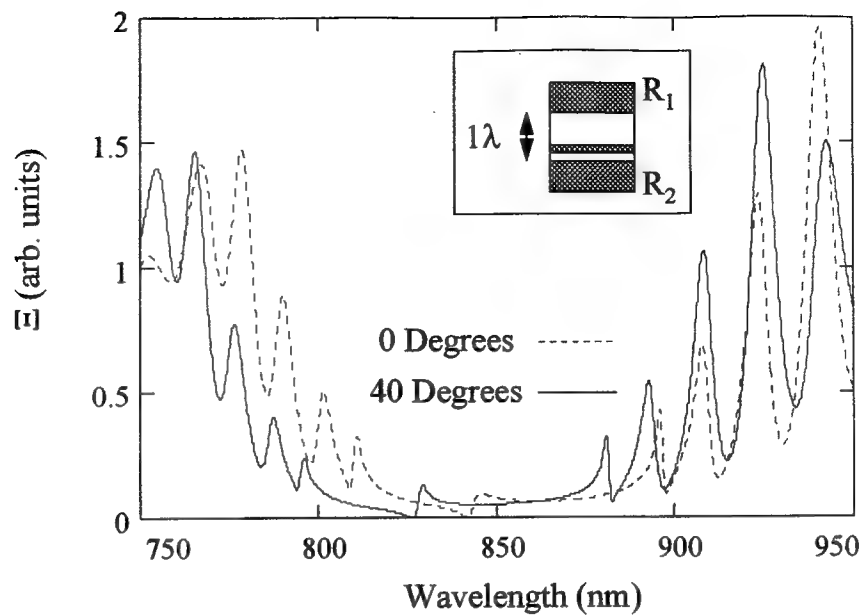


Figure 46.  $R$  calculated for quantum well layer located  $\lambda/4$  away from the center of the microcavity toward  $R_2$

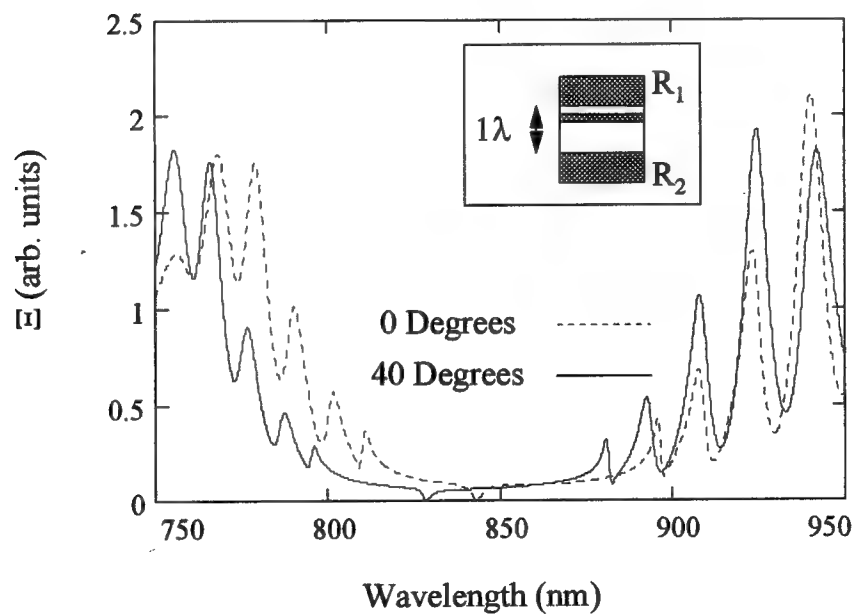


Figure 47.  $R$  calculated for quantum well layer located  $\lambda/4$  away from the center of the microcavity toward  $R_1$

The next step is to modify the unenhanced, calculated emission spectrum of the QW layer with  $\Xi$  in order to calculate the expected output spectrum of Structure 2. Figure 48 shows that the spontaneous emission blue-shifts with angle and that the Q of the output, increases with increasing angle.

Table 4 shows the FWHM,  $\lambda_{\text{peak}}$  and Q ( $Q = \lambda_{\text{peak}}/\text{FWHM}$ ), associated with Figure 48. Table 4 indicates that this model expects the narrowing of the emission spectrum with increasing output angle. This narrowing of the FWHM is attributed to increased DBR reflectance at shorter wavelengths due to greater differences between the refractive indices of the high and low index quarter wave layers.

It should be noted that  $\Xi$  could also be modified by other microcavity factors in order to completely model the coupling between the energy in the field and the emission mode of the RCLED. The mode coupling parameter,  $\beta$ , accounts for this efficiency.  $\beta$  is defined as the “cavity-induced enhancement of the spontaneous emission coupling efficiency into a lasing mode [27].” The external quantum efficiency also decreases for increasing cavity Q, because fewer photons are emitted due to increased reflectance [33]. These parameters are beyond the scope of a classical wave interference model and require a rigorous quantum electrodynamic treatment[8;34]. Therefore Figure 45 does not necessarily show the correct scaled output with respect to intensity. This may affect other results, such as FWHM, that must be measured using intensity.

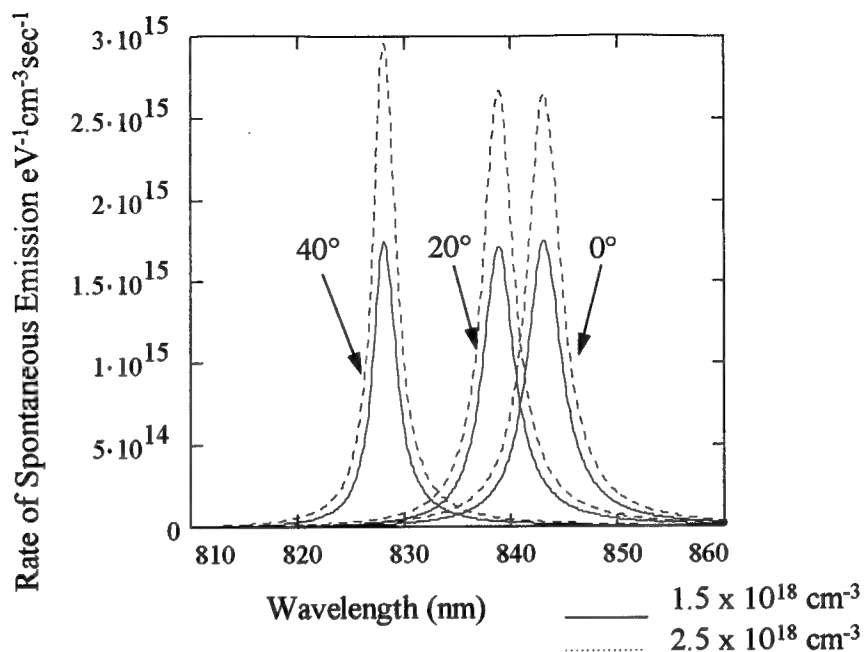


Figure 48. Calculated spontaneous emission from Structure 2 for carrier injection levels of  $1.5 \times 10^{18} \text{ cm}^{-3}$  and  $2.5 \times 10^{18} \text{ cm}^{-3}$ .  $T = 300\text{K}$

Table 4. Calculated Parameters of Figure 48.

Angle (deg)	0	5	10	15	20	25	30	35	40
$\lambda_{\text{peak}}$	843.1	842.9	842.0	840.7	838.9	836.6	834.0	831.1	828.0
FWHM( $\Delta\lambda_{1/2}$ )	3.832	3.822	3.741	3.673	3.526	3.382	3.14	2.873	2.568
Q	220	220	225	229	238	247	266	289	322

### 3.5 Summary

A new classical wave interference model with included angular dependence was presented. The purpose was to examine the enhancement effects of a microcavity on spontaneous emission. First, the reflectance spectrum of Structure 2 was calculated with the Mathcad document in Appendix B. Then, the spontaneous emission

spectrum of Structure 1 was calculated using Appendix C. Finally, the spontaneous emission enhancement,  $\Xi$ , due to the presence of a microcavity was calculated for Structure 2.  $\Xi$  enhances the spontaneous emission of Structure 2 and also blue-shifts the emission spectrum, with increasing angle.

The choice of grading scheme used for the DBRs changes the effective size of the cavity. Using Scheme 1 in Figure 40 blue-shifts the Fabry-Perot dip while Grading Scheme 2 puts the dip at the calculated wavelength. Scheme 1 may be favored because of the better field confinement for the quantum well layer in the separate confinement hetero-structure formed by the cavity.

Other  $\Xi$  modification factors caused by the micro-cavity such as the mode coupling efficiency  $\beta$ , and decreasing external quantum efficiency with increasing  $Q$  are not considered in this model.

## 4. Experimental Method

### 4.1 Laboratory Configuration

This section contains the experimental setups used for measuring the photo-luminescence (PL), electro-luminescence (EL), reflectance and angular emission spectra under EL of the two cavity structures. There were two samples available for study. Sample E236 corresponds to Structure 1 and consists of a microcavity alone. Sample E231 corresponds to Structure 2 and is a complete RCLED structure.

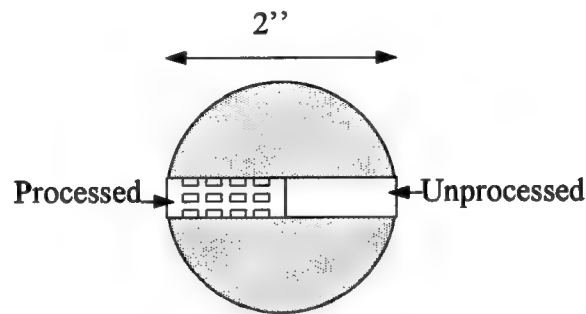


Figure 49. Location of samples E236 and E231 on 2" GaAs wafer

E236 and E231 both consisted of processed and unprocessed halves of a strip of the wafer taken from the center (Figure 49). Processed means that metal contacts with circular apertures for light-emission were deposited on the top and bottom of the devices after growth using lithographic techniques. The apertures range in diameter from  $5\mu\text{m}$  to  $50\mu\text{m}$ . Unprocessed means that no fabrication was performed after growth (i.e. bare epitaxial layers).

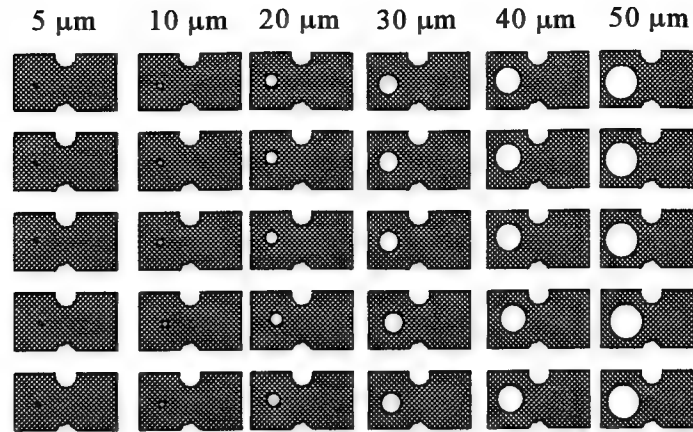


Figure 50. Device layout on processed samples (the size of the aperture is indicated)

#### 4.2 Photo-Luminescence Experimental Setup

Photo-luminescence (PL) is caused by the injection of energetic photons. The photons must have energy  $E_{inject} > E_{trans}$  where  $E_{trans}$  is the transition energy of the energy levels in the QWs. The injected energy generates carriers that recombine at the QW transition energies. For an  $8nm$  GaAs QW with  $Al_{0.15}Ga_{0.85}As$  barrier layers this represents a peak emission wavelength of  $\sim 850nm$ .

The experimental setup necessary to measure both the emitted PL and reflectance spectra during PL is shown in Figure 51.

The Ti:Sapphire laser is pumped by an Argon laser and is wavelength tunable from  $\sim 780-920nm$ . The white light source emits broadband light (ultra-violet - infrared) to generate the reflectance spectrum. The Ti:Sapphire must be tuned to a wavelength where the RCLED has low reflectance, and which is less than the design wavelength, in order to pump the RCLED and fill the QWs with carriers. The white light source is used to determine the reflectance of the substrate at the pumping location. To ensure that the



Ti:Sapphire laser and the white light source illuminate the RCLED at the same location, it is necessary to align them using beam-splitters (Figure 51). Peak PL emission occurs at the Fabry-Perot dip of the RCLED being pumped.

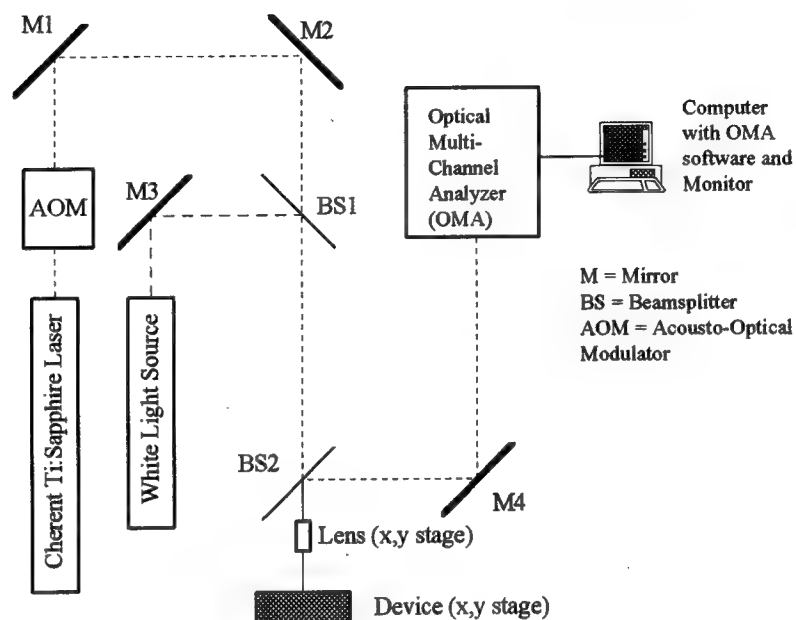


Figure 51. Experimental setup for photo-luminescence and reflectance measurements on RCLEDs.

Table 5. Equipment Listing for Photo-Luminescence.

Optical Multichannel Analyzer (OMA)	Manufacturer	Princeton Applied Research
	Model	EG&G 1460
	Accuracy	$\pm 3\text{\AA}$
Ti:Sapphire Laser	Manufacturer	Coherent
	Output Power	$\sim 1$ Watt
Diode Focusing Lens	Manufacturer	Melles Griot
	Focal length	2.54cm
	Spot Size	1.85 $\mu\text{m}$

### 4.3 Electro-Luminescence Experimental Setup

Electro-luminescence (EL) is caused by the application of an electric field. As the field is applied to the RCLED, injected carriers recombine in the QW layers and photons are emitted. The wavelength of the emitted photons is governed by the energy levels within the QW of the RCLED microcavity. The experimental setup necessary to measure both the emitted EL and reflectance spectra during EL is shown in Figure 52.

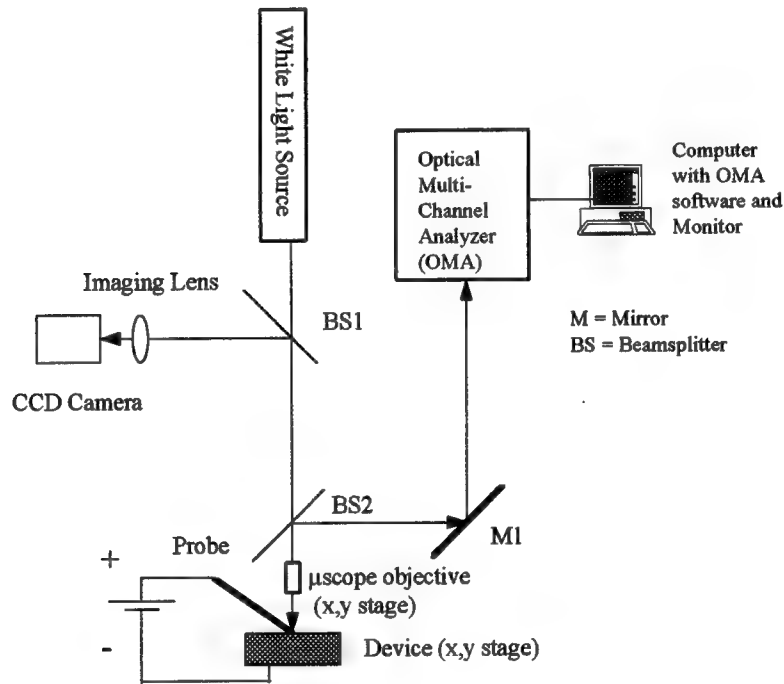


Figure 52. Experimental setup for electro-luminescence and reflectance measurements of RCLEDs

EL requires a charge-coupled device (CCD) camera in order to place the electrical probe on the RCLED near the aperture. It was found that imaging the devices directly onto the CCD array without the camera lens worked best. During this research the electrical probe was located at exactly the same place on the device each time in order to achieve uniformity in injection conditions. The device was also aligned in the same orientation in the field of

view of the microscope objective to reduce errors due to different sampling conditions. The microscope objective has magnification 10X and numerical aperture of 0.25.

A waveform generator in continuous wave (CW) mode was used to energize the electrical probe and cause electro-luminescence in the RCLED. The electrical path to ground for the injected electrons is through the RCLED and into the x-y translation stage (grounding pad) shown in Figure 52. It is essential that good electrical contact be made between the back of the RCLED and the grounding pad.

#### **4.4 Angular Measurements Using Fiber Optic Probe**

In order to fulfill the main goal of this thesis, the correlation of the theoretical emission spectrum with the experimentally measured spectrum, it was necessary to build a fiber optic probe capable of being rotated around the sample. The silica fiber used was a Belden Inc., graded index, multimode fiber with a  $50\mu\text{m}$  core and a numerical aperture (NA) of 0.28.

The tip of the fiber probe was aligned to the axis of rotation of the angular translation device in Figure 53. Therefore the tip of the probe would not be pulled off the RCLED during rotation. In practice it was better to intentionally pull the fiber tip off the axis of rotation by a small amount (Figure 54), because if it were too long the fiber would hit the RCLED during rotation. Some assumptions were made in order to validate the use of the fiber probe. First, that the best way to keep the fiber probe on-sample (that is pointing squarely at the sample) was to use the intensity reading from the optical multi-channel analyzer (OMA) as the metric of alignment. That is, for a given angle,  $\alpha$ , the fiber was translated using its x-y stage until the peak wavelength intensity was maximized, according to the OMA. Second, that the fiber used was too short ( $\sim 0.5\text{m}$ ) to significantly

change the parameters being measured, either through absorption or dispersion. The fiber probe is shown in Figure 53.

The physical limitations of the fiber probe are as follows. The angle of rotation of the fiber optic was measured to an error of  $\pm 1$  degree. The fiber-optic probe was aligned to the axis of rotation to an error of  $\sim 1$  mm. Again, this was necessary to prevent the probe being pulled off the sample as it was rotated (Figure 54) and the error was purposely made on the short side in order to keep the probe tip on a constant circular trajectory as it was translated around the sample. This kept lateral translations with the x-y stage to a minimum.

The multi-mode nature of the fiber caused broadening in the measured samples. This broadening is due to two factors. First, the numerical aperture (NA) caused emission from non-desired angles (not the angle being measured) to enter during a measurement (Figure 54). Secondly, due to the multi-mode nature of the fiber, the emission from the non-desired angles propagated in the fiber and broadened the measurement. The broadening is less for lesser angles ( $\sim 0^\circ$ ) because of the symmetry of the emission at those angles. As the measured angle increases the asymmetrical field at higher angles causes more broadening in the measurement. Broadening of the emission spectrum leads to errors in measured full width at half maximum (FWHM). Fiber broadening would be avoided with a single-mode fiber, however the equipment was not available to align a single-mode fiber with  $\sim 7\mu\text{m}$  core.

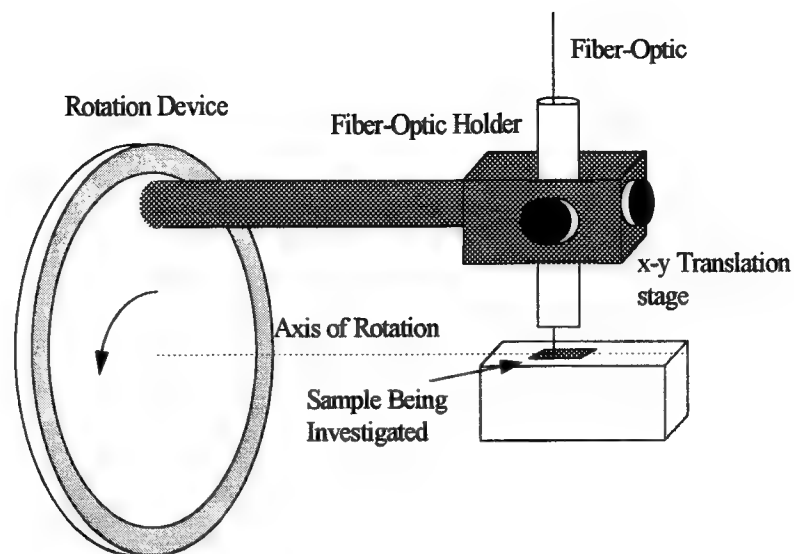


Figure 53. Fiber-optic probe with angular translation used in experiments.

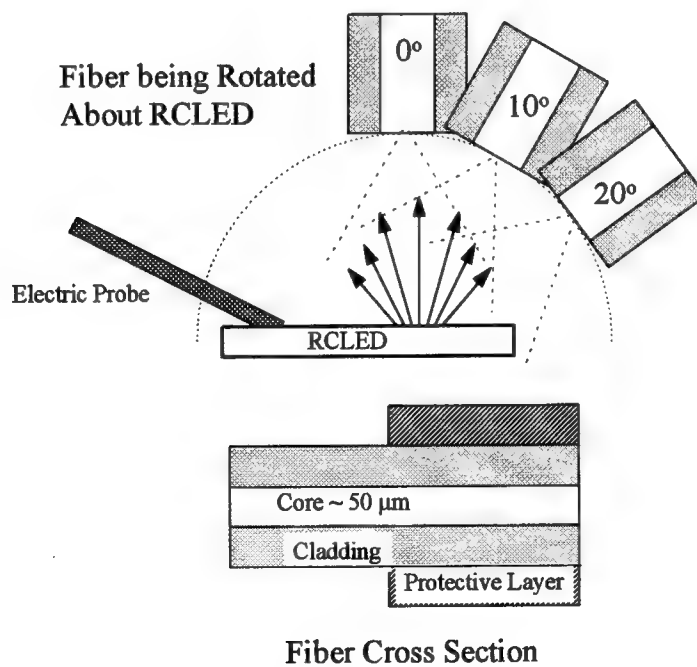


Figure 54. Fiber being rotated around sample RCLED, the dashed lines represent the numerical aperture of the fiber

#### **4.5 Aligning The Fiber Optic Probe**

The best way to align the fiber probe was to first electrically pump the RCLED using the microscope objective to image the electrical probe and the RCLED on the CCD camera. Then the microscope objective was removed and the fiber probe put in its place. The output end of the fiber probe is placed against the CCD camera. When the fiber probe is aligned a circular pattern appears indicating a photon flux emerging from the fiber-optic. Next the end of the fiber probe is placed against the entrance slit of the OMA and adjusted until an emission pattern is visible on the computer monitor. The fiber is now vertically aligned with the sample and ready for angular measurements. The probe worked extremely well. Although it was always difficult to align initially, once aligned it was relatively easy stay centered on the sample.

## 5. Experimental Results

### 5.1 Introduction

For the purposes of presenting the experimental data, sample E236 refers to Structure 1 and sample E231 refers to Structure 2. Both designs have been discussed in Chapter 3. As shown in Figure 55 both E236 and E231 have processed and unprocessed sections. "Processing" means depositing metal contacts on the upper and lower wafer surfaces in order to electrically inject carriers into the sample. Photo-luminescence does not require these extra manufacturing steps. The wafer had been split into three sections for each sample. One section was unprocessed and was used for PL. Two sections were processed and used for EL. Sections ii and iii had very similar properties because the sample was rotated during growth. Section iii was not used during the experiment.

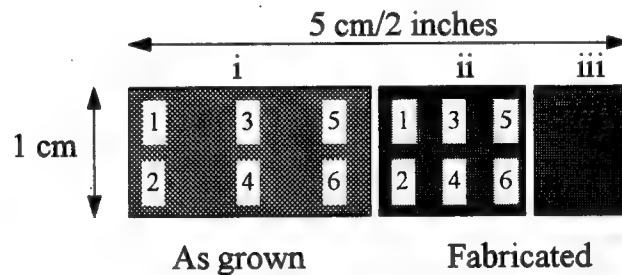


Figure 55. Diagram of E236 and E231 orientation used in PL (left) and EL (right)

This chapter presents the data measured using the methods outlined in Chapter 4 and then compares these measured results to the theoretical results of Chapter 3. Good agreement is found for predicting blue-shift behavior with angle. The FWHM is not tracked very well due to the limitations of the model with regard to changing absorptance under current injection, lack of second-order microcavity effects, and diffraction effects due to the device aperture.

## 5.2 Device Parameters

These devices were built using a low-pressure MOVPE system with quartz lamp heating. The temperatures inside the growth chamber can reach 700-800°C depending on the layer being grown. The layers of E231 and E236 are grown on top of an  $\sim 500\mu m$  thick, (100) oriented, (n+) GaAs substrate. A buffer layer of (n+) GaAs was grown on the substrate to smooth the surface for further growth. E231's lower DBR (Si doped  $\sim 2 \times 10^{18} \text{cm}^{-3}$ ) has a HL index  $\lambda/2$  period of  $\sim 12nm$  linear grading  $\text{Al}_x\text{Ga}_{1-x}\text{As}$ :  $0.15 \leq x \leq 1.0$ ,  $\sim 58.6nm$  AlAs,  $\sim 12nm$  linear grading  $\text{Al}_x\text{Ga}_{1-x}\text{As}$ :  $1.0 \geq x \geq 0.15$ ,  $\sim 49.8nm$   $\text{Al}_{0.15}\text{Ga}_{0.85}\text{As}$ . There are 38.5 HL periods in the lower DBR. E231's upper DBR (C doped  $\sim 2 \times 10^{18} \text{cm}^{-3}$ ) has a LH index  $\lambda/2$  period of  $\sim 58.6nm$  AlAs,  $\sim 12nm$  linear grading  $\text{Al}_x\text{Ga}_{1-x}\text{As}$ :  $1.0 \geq x \geq 0.15$ ,  $\sim 49.8nm$   $\text{Al}_{0.15}\text{Ga}_{0.85}\text{As}$  and  $\sim 12nm$  linear grading  $\text{Al}_x\text{Ga}_{1-x}\text{As}$ :  $0.15 \leq x \leq 1.0$ . There are 6 periods in the upper DBR. The last  $\lambda/4$  layer contains  $\sim 20nm$  p+ GaAs to help form an ohmic contact. The E231 DBR grading scheme corresponds to Scheme 1 (Chapter 3) and the Fabry-Perot dip is expected to blue shift from the design wavelength of  $850nm$ . E236 has  $\sim 735nm$   $\text{Al}_{0.15}\text{Ga}_{0.85}\text{As}$ ,  $\sim 12nm$  linear grading  $\text{Al}_x\text{Ga}_{1-x}\text{As}$ :  $0.15 \leq x \leq 1.0$ ,  $\sim 58.6nm$  AlAs beneath its cavity and  $\sim 58.6nm$  AlAs,  $\sim 12nm$  linear grading  $\text{Al}_x\text{Ga}_{1-x}\text{As}$ :  $1.0 \geq x \geq 0.15$ ,  $\sim 715nm$   $\text{Al}_{0.15}\text{Ga}_{0.85}\text{As}$ ,  $\sim 20nm$  p+ GaAs above the cavity. The cavity for both E236 and E231 is  $\sim 99.8nm$   $\text{Al}_x\text{Ga}_{1-x}\text{As}$ :  $1.0 \geq x \geq 0.15$ , four GaAs  $8nm$  quantum wells with  $10nm$   $\text{Al}_{0.15}\text{Ga}_{0.85}\text{As}$  barriers,  $\sim 99.8nm$   $\text{Al}_x\text{Ga}_{1-x}\text{As}$ :  $0.15 \leq x \leq 1.0$ . The cavity is  $1\lambda$  thick at  $\lambda = 850nm$ . This information is abbreviated in Table 6.



Table 6. Growth Table for E231 and E236.

	E236 (Structure 1)	E231 (Structure 2)
Ohmic Contact	200Å GaAs Cap p+doped (C)	200Å GaAs Ca p+doped (C)
Upper DBR (HL)	7150Å Buffer Region p-doped (C)	Al <sub>0.15</sub> Ga <sub>0.85</sub> As/AlAs (linearly graded) p-doped (C)
Cavity	1λ Al <sub>0.15</sub> Ga <sub>0.85</sub> As/AlAs (linearly graded)	1λ Al <sub>0.15</sub> Ga <sub>0.85</sub> As/AlAs (linearly graded over 998 Å)
Quantum Wells	Four 8nm GaAs QWs with 10nm Al <sub>0.15</sub> Ga <sub>0.85</sub> As Barriers	Four 8nm GaAs QWs with 10nm Al <sub>0.15</sub> Ga <sub>0.85</sub> As Barriers
Lower DBR (HL)	7350Å Buffer Region n-doped (Si)	Al <sub>0.15</sub> Ga <sub>0.85</sub> As/AlAs (linearly graded) n-doped (Si)
Substrate	GaAs n+ doped (Si)	GaAs n+ doped (Si)

### 5.3 Experimental Data Presentation

Figure 56 shows the measured blue-shifting of the emission spectrum with increasing angle of E231 (Structure 2) under electro-luminescence. This was expected from the calculations in Chapter 3. The spectrum broadening, instead of narrowing, with increasing angle is attributed to diffraction from the  $50\mu\text{m}$  aperture, sampling with a multi-mode fiber, and increased absorptance with injected current. Diffraction causes energy from smaller emission angles to be spread into larger measured angles. Other apertures were not used for measuring because of difficulties in aligning the fiber probe.

Figure 57 shows the calculated emission from E231 (Structure 2) using the measured emission spectrum of E236 (Structure1). The peak wavelengths and FWHMs of Figure 57 are given in Table 4.

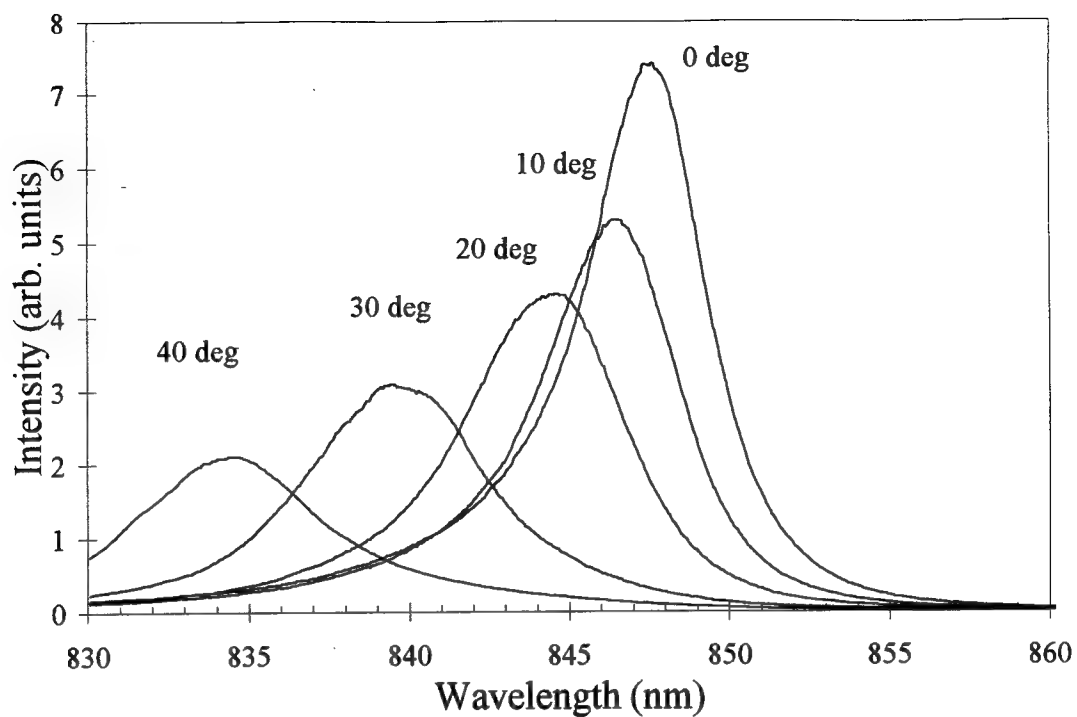


Figure 56. Measured electro-luminescence spectrum of E231 (Structure 2) versus angular deviation from normal

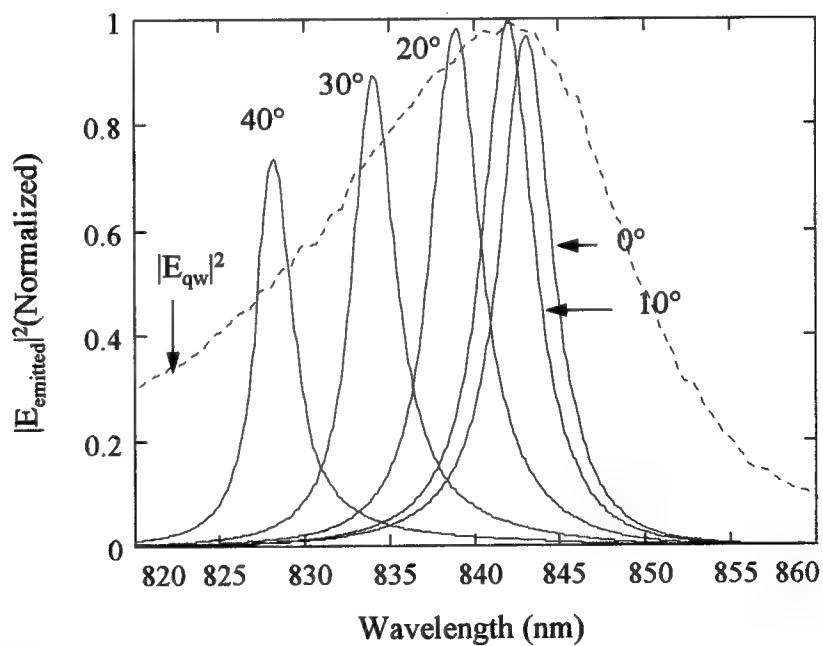


Figure 57. Normalized calculated E231 (Structure 2) emission (solid) using measured E236 (Structure 1) emission.

Table 7 contains the relevant parameters from Figure 56. These parameters are peak wavelength, FWHM, and Q versus measured angle. Figure 58 shows the measured reflectance from the unprocessed E231 sample. The measurements were taken at the corresponding locations in Figure 55. The Fabry-Perot dip does not vary by more than 1% between devices 4 and 6 showing high uniformity during growth. Device 2 is ~3% from the other devices, probably because it was located so close to an edge, which can cause non-uniformity. Figure 59 compares the calculated and measured reflectances for E231 (Structure 2). Figure 59 shows that the calculated reflectance does not include enough absorptance in the refractive index information. This is evident because of the lower reflectances of the measured data. The design wavelength is *850nm*, but the MATHCAD reflectance program calculates a shifted dip at *841nm* due to grading the DBRs using Scheme 1. Figure 60 shows the emission spectrum of E236 under electro-luminescence. The emission clearly has no angular dependence and does not change for various fiber sampling angles. It has the characteristics of a lambertian emitter.

Table 7. Measured Parameters for Figure 56.

Angle	0	5	10	15	20	25	30	35	40
Peak $\lambda$	847.62	847.32	846.47	845.68	844.65	842.17	839.5	837.08	834.47
FWHM	4.52	4.7	5.07	5.48	5.9	6.53	6.6	6.3	6.84
Q	187.53	180.28	166.96	154.32	143.16	128.97	127.20	132.87	122.00

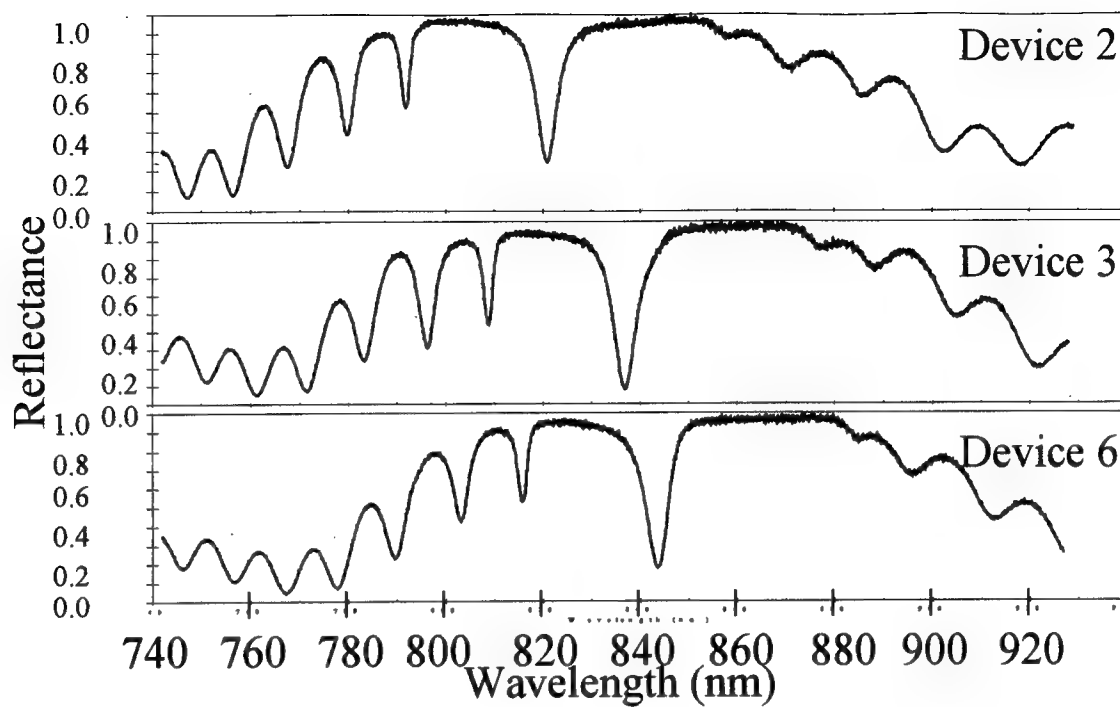


Figure 58. Measured reflectance from various locations on unprocessed E231 sample (Structure 2)

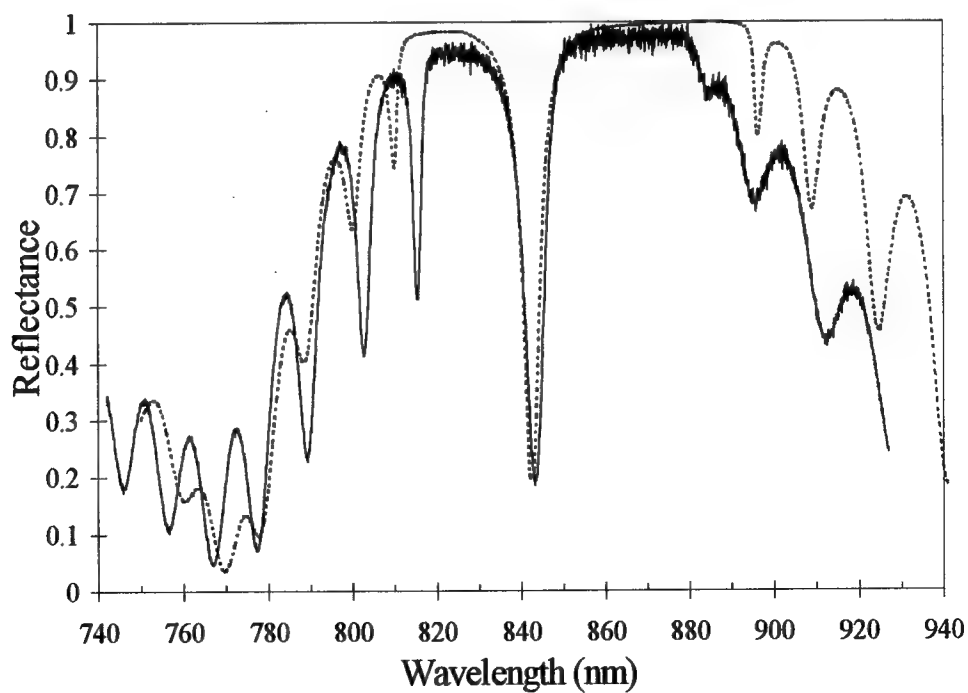


Figure 59. Measured (solid) and calculated (dashed) reflectance from device E231 at location 3 (unprocessed) in Figure 55

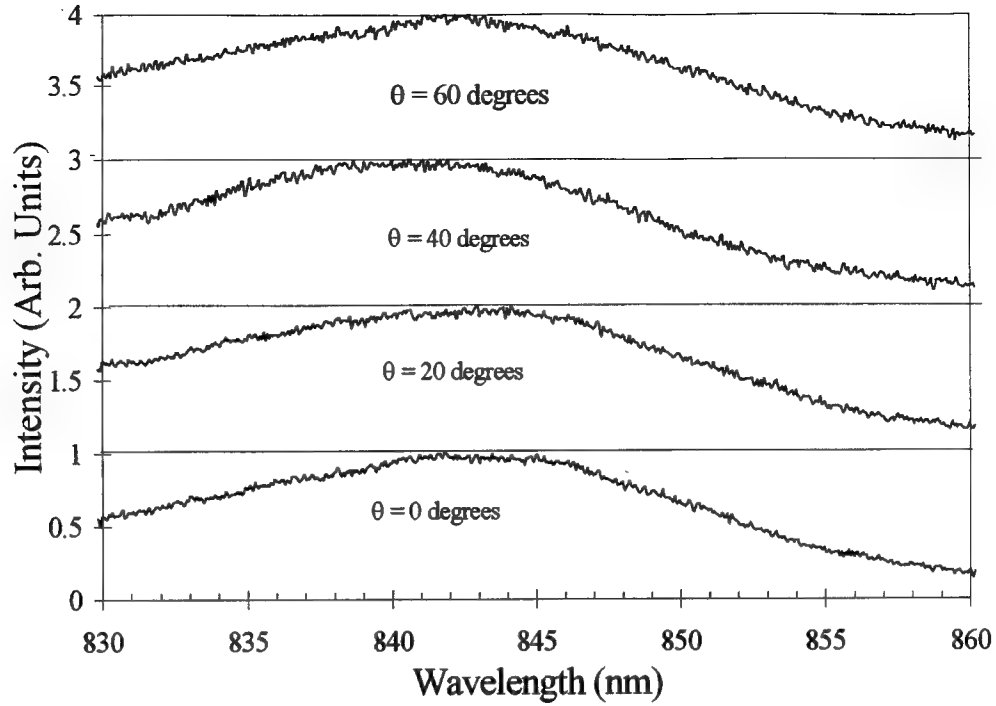


Figure 60. Electro-luminescence of sample E236 versus angle

The emission from a QW layer such as E236 (Structure 1) should be narrower than that of a bulk emitter. The spectral width of the emission in Figure 61, using the full-width at half maximum (FWHM) criteria, is  $\sim 25\text{nm}$ . The approximate predicted wavelength for a bulk spontaneous emitter at  $300\text{K}$  with  $\lambda_{\text{peak}} \sim 840\text{nm}$  is  $27\text{nm}$  using  $\Delta\lambda \approx 1.45\lambda_{\text{peak}}^2 k_B T$ , where  $\Delta\lambda$  and  $\lambda_{\text{peak}}$  are in microns and  $k_B T$  is in eV. The QW emission is slightly narrower than the calculated bulk emission. Table 2 shows the parameters of peak wavelength, FWHM, and Q for Figure 61. The FWHM is seen to increase fairly substantially with increased injection current. The increase in FWHM is expected because of the increasing separation of the quasi-fermi levels with increased carrier injection.

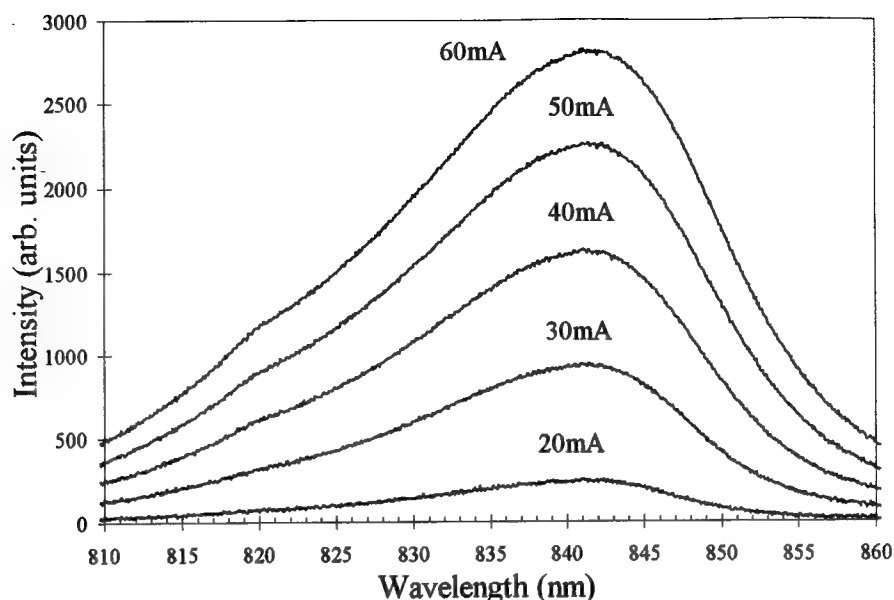


Figure 61. Measured electro-luminescence spectrum from sample E236 (Structure 1) for various injection currents

The lack of additional transitions in the spectrum enforces the calculated finding of only one electron/heavy-hole transition at  $\lambda=850nm$  in the well. The shifting of the transition wavelength for E236 (Structure 1) from the calculated  $850nm$  may be due to thickness variations in the quantum well. Because the transition has blue-shifted from  $850nm$  this indicates that the quantum well is narrower than designed, thus causing the allowed, quantized, energy levels to increase their separation. Figure 63 shows the emission spectrum from a device on E231 plotted for various injection currents. Notice that the FWHM of  $\sim 5nm$  does not change for increasing carrier injection. This is due to the microcavity effects of the RCLED. Although direct intensity comparisons between Figures 61 and 62 is not possible because no exact intensity readings were taken, a qualitative examination of the numbers reveals that the spontaneous emission has been greatly enhanced. Much narrower FWHM and higher output intensity are the main advantages of RCLEDs over conventional LEDs.

Table 8. Measured Parameters for Figure 61.

Current (mA)	20	30	40	50	60
Peak $\lambda$	840.8	841.2	841.2	841.4	841.2
FWHM	20.1	23.0	25.0	26.5	28.0
Q	41.8	36.6	33.6	31.8	30.0

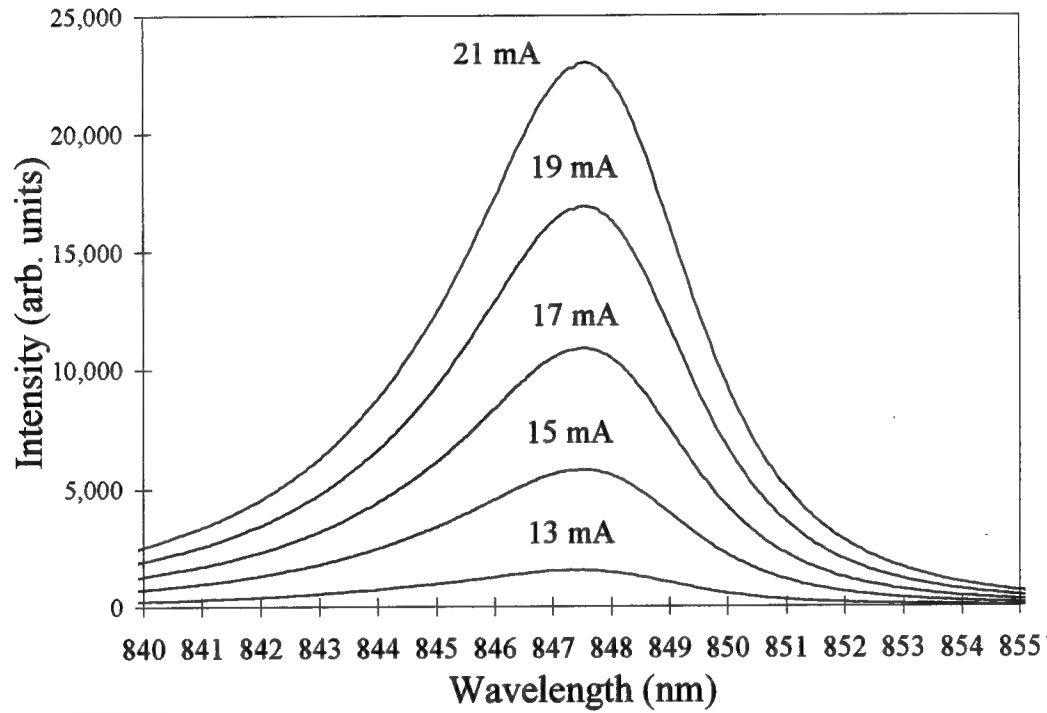


Figure 62. Measured electro-luminescence of sample E231 (Structure 2) for various injection currents

Table 9. Measured Parameters for Figure 62.

Current (mA)	13	15	17	19	21
Peak $\lambda$	847.3	847.5	847.6	847.6	847.6
FWHM	5.2	5.0	5.0	5.0	4.8
Q	162.9	169.5	169.5	169.5	176.6

Figure 63 shows the emission and reflectance spectra for a device on sample E231.

Figure 63 clearly shows that the Fabry-Perot dip does indeed define the location the

emitted radiation. Figures 64 and 65 show the emitted spectrum from samples E236 and E231 under photo-luminescence from a Ti:Sapphire laser. The AOM scale is not power-calibrated but a relative comparison is possible. The emission wavelength of the Ti:Sapphire laser is  $800\text{nm}$ . The same characteristics of FWHM and Q as for EL are visible, although Figure 64 has a lot of noise that may be due to photo-luminescence of the bulk GaAs substrate and AlGaAs buffer by the Ti:Sapphire laser.

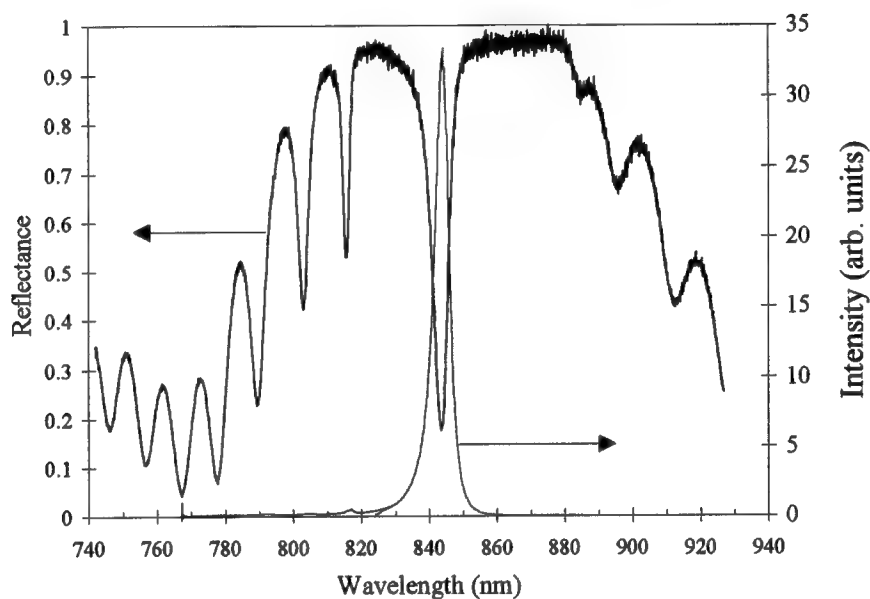


Figure 63. Measured electro-luminescence and reflectance spectra from same location on sample E231 (Structure 2)



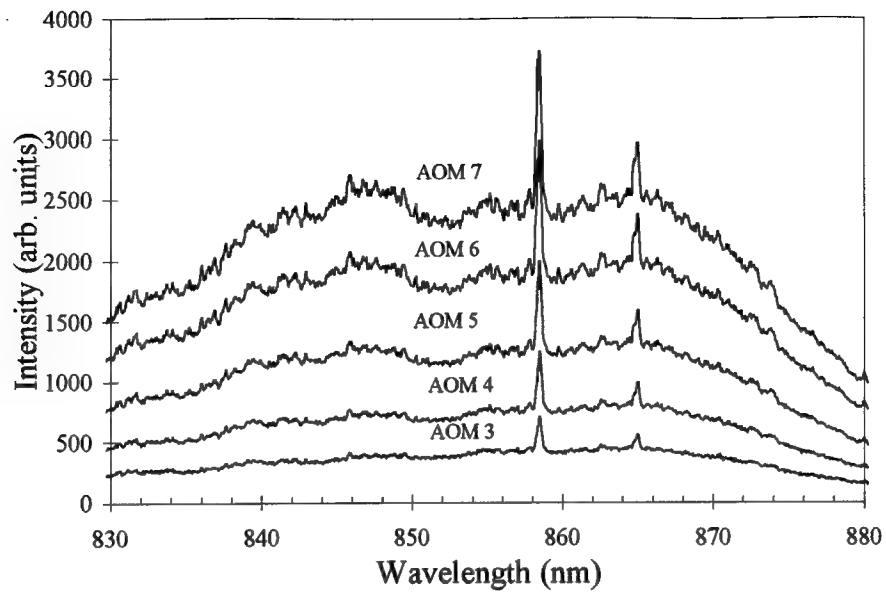


Figure 64. Photo-luminescence of sample E236 (Structure 1) at various input optical power densities

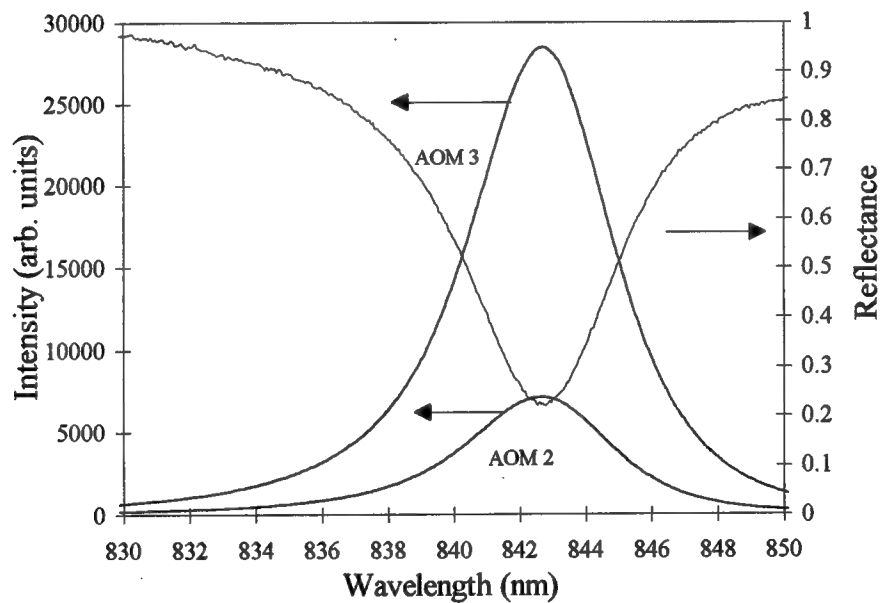


Figure 65. Photo-luminescence from sample E231 (Structure 2)

#### 5.4 Comparison of Calculated and Experimental Results

The data in the tables above is presented in graphical form in direct comparison with the calculated results. Injection levels cannot be compared directly because they were not explicitly addressed in the model. Figure 66 shows the calculated Q and FWHM for the plots of Figure 61. The RCLED model predicts a non-varying Q and FWHM with increased injection current. This is because the model depends only on the reflectances of the upper and lower DBRs of the RCLED. The Q has a linear coefficient of  $R^2=0.8366$ . The FWHM has a linear coefficient of  $R^1=0.823$  with error bars denoting  $\pm 3\text{\AA}$ . This error is based upon the accuracy of the OMA and the subtraction of the upper and lower half maximum wavelengths needed to get the FWHM. Figure 66 shows the calculated and measured FWHM and Q for sample E231 (Structure 2). The parameters are plotted against the angle  $\phi$ , which is the angle of the fiber-optic probe during measurement. Figure 67 shows the calculated and measured peak  $\lambda$  values for E231 (Structure 2). The values are always within 1.0% of each other and have a joint correlation coefficient of 0.998. The joint correlation coefficient is calculated using:

$$\rho_{x,y} = \frac{\frac{1}{n} \sum_{i=1}^n (x_i - \mu_x)(y_i - \mu_y)}{\sigma_x \sigma_y} \quad -1 \leq \rho_{x,y} \leq 1 \quad (\text{unitless}) \quad (65)$$

where  $\mu_x$  and  $\mu_y$  are the means of the data, and  $\sigma_x$  and  $\sigma_y$  are the respective standard deviations. Note that the peak wavelength difference is due to measuring the emission at a location where the DBR thickness' and cavity thickness were not exactly as calculated. The calculated data can easily be shifted to match the experimental data by changing the design wavelength used in the emission model.

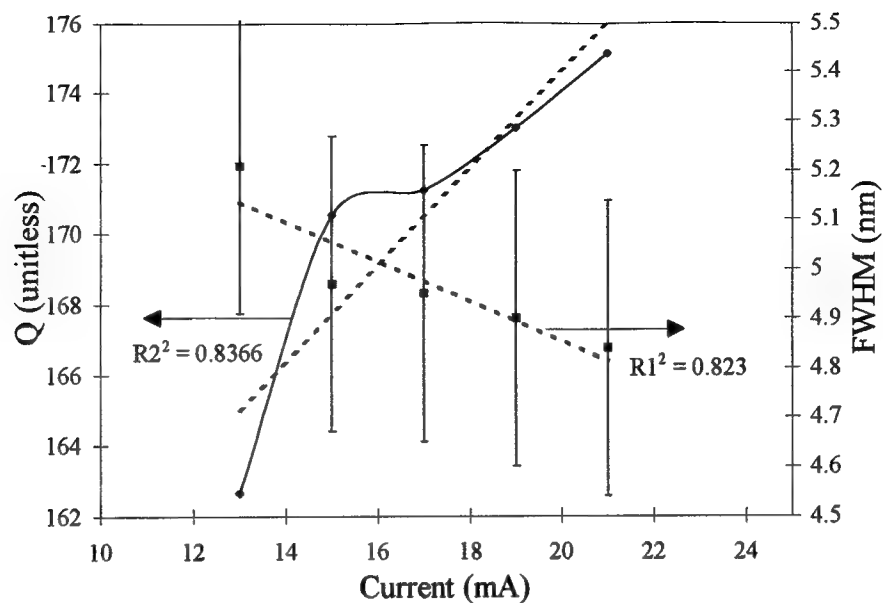


Figure 66. Measured FWHM and Q for sample E231 (Structure 2) under electro-luminescence (Figure 62) showing linear correlation coefficients for the data (dotted)

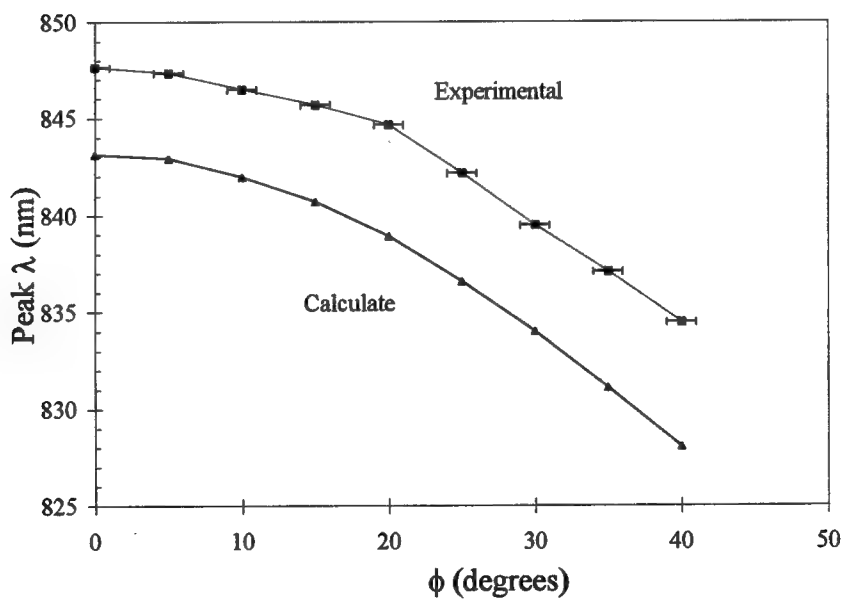


Figure 67. Calculated and experimental peak  $\lambda$  for E231 (Structure 2)

Figure 68 shows the calculated and measured FWHM for Structure 2. RCLED. The trendline (dotted) shows the coefficient of linearity,  $R^2$ , of the experimental FWHM. There is a substantial disagreement in the change of FWHM vs.  $\phi$ . The two data sets have a joint correlation coefficient of -0.867. The broadening of the experimental FWHM with increasing angle may be due to a change of complex refractive index under current injection. Increased absorption, for instance due to prolonged current injection during measurements, will broaden the Fabry-Perot dip and cause the FWHM to decrease. Broadening also occurs due to diffraction effects at the device aperture and using a multi-mode fiber for taking measurements. Both of these cause energy at longer wavelengths from lower emission angles to be measured at a higher angle. The diffraction affects at the aperture are unavoidable. By taking all the measurements at the largest aperture, broadening due to diffraction was made as small as possible.

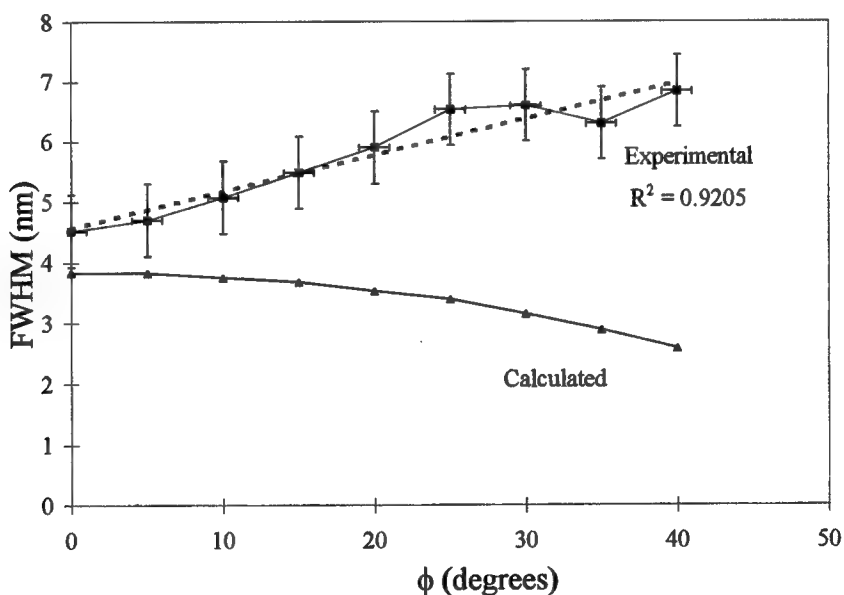


Figure 68. Calculated and experimental FWHM for E231 (Structure 2)

## 5.5 Results Summary

The experimental and calculated values of FWHM and  $\lambda_{\text{peak}}$  were examined for E231 (Structure 2). Good results were obtained for tracking and estimating  $\lambda_{\text{peak}}$  with high accuracy, given the initial location of the Fabry-Perot dip. However the FWHM estimator shows high negative correlation. This may be due to inaccurate absorptance data under current injection, diffraction affects at the device aperture, non-inclusion of second order microcavity effects such as mode coupling and loss of external quantum efficiency, or a mixture of all four. All events would serve to broaden the output. The model does show good accuracy in calculating the prospective range of the output FWHM, and may prove a useful tool in this regard.

## 6. Conclusion

The goal of this thesis was to develop a to simulate the emission spectra of the RCLED and its variation with angle. Achieving this goal required modeling the quantum well energy levels and emission characteristics, calculating gain and spontaneous emission spectra for the quantum well, calculating DBR reflectances, calculating electric field intensity, and using a new classical wave interference model to derive an analytic expression for the spontaneous emission enhancement factor ( $\Xi$ ) of a microcavity device. Two devices were designed, grown and fabricated in order to measure the parameters described above. The first consisted of a  $1\lambda$  cavity with four quantum wells. The second consisted of the same  $1\lambda$  cavity with four quantum wells, but with DBRs used to form a true RCLED structure. The emission from the second device was significantly narrower in bandwidth and of higher intensity than that of the first device. The spectral emission of the second device was compared to that of the model.

The results achieved during this work are new and demonstrate the emission pattern of a RCLED is not lambertian. A blue-shift occurs in the emission spectrum with increasing angle from the normal. The model is extremely accurate in tracking peak emission wavelength variation with angle. The model was less accurate in calculating the FWHM of the emitted radiation, but factors not considered in the model come into play for this parameter. Diffraction effects from the emission aperture, and the use of multi-mode fiber, cause broadening because longer wavelengths from lower emitted angles are measured by the probe at a greater angle. Extra absorption in the device due to heating under current load would also cause a broadening of the emission spectrum at all angles. An experimental technique developed during the course of this work was to use a fiber optic cable on a

rotational stage to measure the emitted spectrum versus angle of an RCLED under electroluminescence.

The main contribution of this work is a new model for calculating the emission spectra of the RCLED with angular dependence. This model is applicable to any RCLED structure, regardless of emission wavelength or DBR design. The Mathcad document in Appendix B can calculate the reflectances of any RCLED DBR, regardless of compositional grading scheme or material composition, that is required for the model.

Future work in this area should include the following:

1. Measure emitted spectrum from range of aperture sizes and compare using FWHM as a metric. Diffraction effects should be greater for smaller apertures.
2. Use a single-mode fiber to make angular measurements. This will eliminate broadening due to the fiber probe.
3. Further examine differences in DBR grading schemes presented in Chapter 3 with regard to exact placement of the Fabry-Perot dip. This seems to be a new area for research that is presently untapped.
4. Examine other microcavity effects, such as the mode coupling efficiency factor  $\beta$ , that are not discussed in this thesis.  $\beta$  modifies  $\Xi$  in a nonlinear way and prevents all the available energy from being coupled into a microcavity emission mode.
5. Apply model to RCLEDs in other wavelength ranges, such as *560-690nm*, using  $(\text{Al}_x\text{Ga}_{1-x})\text{In}_{1-y}\text{P}$  cavities with AlGaInP and/or AlGaAs DBRs. Also to the new ZnSe and AlGaInN blue-emitting RCLEDs

RCLEDs are a new and exciting addition to Photonics, and it was exciting to work on the cutting edge of LED technology.

## Appendix A: Reflectance Calculations

### A.1 Reflectance Calculations

Macleod's matrix method relating the input and output electric fields is used to calculate the reflectance spectrum for arbitrary layers of thin films [10;26]. By relating the electric and magnetic fields at two boundaries in a matrix form, it is possible to calculate the reflectance spectra of complicated structures.

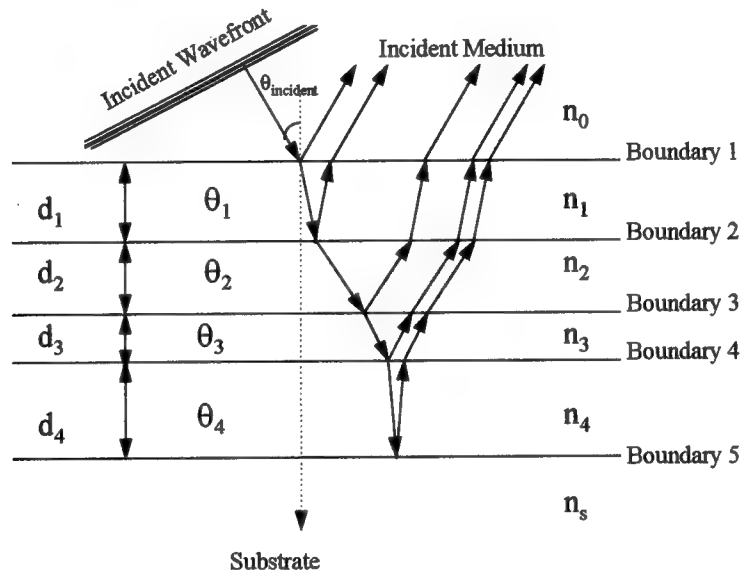


Figure 69. Plane wave incident on a set of thin films

The electric (E) and magnetic (H) fields at boundary 1 may be related to the electric and magnetic fields at boundary 2 by:

$$\begin{pmatrix} E_1 \\ H_1 \end{pmatrix} = \begin{pmatrix} \cos \delta_1 & i \sin \delta_1 / \eta_1 \\ i \sin \delta_1 \eta_1 & \cos \delta_1 \end{pmatrix} \begin{pmatrix} E_2 \\ H_2 \end{pmatrix} = M_1 \begin{pmatrix} E_2 \\ H_2 \end{pmatrix} \quad (66)$$



where  $\delta_l$  is given by Equation 5 for non-absorbing media and by Equation 14 for absorbing media. The optical admittance  $\eta_l$  is measured in *Siemens* and is polarization dependent.

$$\eta_1 = \Psi \eta_1 \cos \theta_1 \text{ (Siemens)} \quad (\text{s-polarized light}) \quad (67)$$

$$\eta_1 = \Psi \eta_1 / \cos \theta_1 \text{ (Siemens)} \quad (\text{p-polarized light}) \quad (68)$$

is the characteristic optical admittance of free space and has a value of  $2.6544 \times 10^{-3}$  *Siemens*. The parameter  $\theta_l$  is the angle between the wavefront and the normal to the film in the first layer. For absorbing media the expressions for optical admittance change to

$$\eta_1 = \Psi (n_1^2 - \kappa_1^2 - n_0^2 \sin^2 \theta_0 - 2in_1\kappa_1)^{1/2} \text{ (Siemens)} \quad (\text{s-polarized light}) \quad (69)$$

$$\eta_1 = \Psi \frac{(n_1 - i\kappa_1)}{(n_1^2 - \kappa_1^2 - n_0^2 \sin^2 \theta_0 - 2in_1\kappa_1)^{1/2}} \text{ (Siemens)} \quad (\text{p-polarized light}) \quad (70)$$

Using this matrix form the fields in the incident layer can be related to the fields at the substrate interface by:

$$\begin{pmatrix} E_1 \\ H_1 \end{pmatrix} = E_1 \begin{pmatrix} 1 \\ Y \end{pmatrix} = \left[ \prod_{r=1}^q \begin{pmatrix} \cos \delta_r & i \sin \delta_r / \eta_r \\ i \eta_r \sin \delta_r & \cos \delta_r \end{pmatrix} \right] \begin{pmatrix} 1 \\ \eta_s \end{pmatrix} E_s = \prod_{r=1}^q M_r \begin{pmatrix} 1 \\ \eta_s \end{pmatrix} E_s \quad (71)$$

The reflectance of a series of thin films is given by:

$$R = \left( \frac{\eta_0 - Y}{\eta_0 + Y} \right) \left( \frac{\eta_0 - Y}{\eta_0 + Y} \right)^* \quad (\text{unitless}) \quad (72)^3$$

---

<sup>3</sup> In all equations an asterisk (\*) denotes the complex conjugate.

where  $Y$  is the input optical admittance of the thin films and is equal to  $H_1/E_1$ . The parameter  $Y$  can be manipulated into:

$$Y = B / C \quad (\text{Siemens}) \quad (73)$$

where  $B$  and  $C$  are obtained from:

$$\begin{pmatrix} B \\ C \end{pmatrix} = \left[ \prod_{r=1}^q \begin{pmatrix} \cos \delta_r & i \sin \delta_r / \eta_r \\ i \eta_r \sin \delta_r & \cos \delta_r \end{pmatrix} \right] \begin{pmatrix} 1 \\ \eta_s \end{pmatrix} \quad (74)$$

The substrate material is taken to be GaAs throughout this thesis. The transmittance ( $T$ ) and absorptance ( $A$ ) are also calculated by Macleod and are readily accessible from the same calculation.

$$T = \frac{4\eta_0 \operatorname{Re}(\eta_m)}{(\eta_0 B + C)(\eta_0 B + C)^*} \quad (\text{unitless}) \quad (75)$$

$$\bullet \quad A = \frac{4\eta_0 \operatorname{Re}(BC^* - \eta_m)}{(\eta_0 B + C)(\eta_0 B + C)^*} \quad (\text{unitless}) \quad (76)$$

## **APPENDIX B: Mathcad Reflectance Calculation Document**

This document calculates reflectance values over a range of wavelengths for grading Scheme 1 structures. Output includes reflectance of the entire structure, reflectance of the upper and lower DBRs from a viewpoint inside the cavity, and the electric field intensity at any point in the structure for any wavelength in the user defined range. The document uses Macleod notation throughout and is based on work by Macleod and Yeh.

### Constants used in Program

$$\begin{aligned} \mu\text{m} &\equiv \text{m} \cdot 10^{-6} & \text{nm} &\equiv \text{m} \cdot 10^{-9} & \text{\AA} &\equiv \text{m} \cdot 10^{-10} & \mathcal{Z} &\equiv 2.6544 \cdot 10^{-3} \cdot \text{siemens} \\ \mu_0 &\equiv 4 \cdot \pi \cdot 10^{-7} \cdot \frac{\text{newton}}{\text{amp}^2} & \epsilon_0 &\equiv 8.854187817 \cdot 10^{-12} \cdot \frac{\text{farad}}{\text{m}} & c &\equiv 299792458 \cdot \frac{\text{m}}{\text{sec}} \\ eV &\equiv \text{joule} \cdot 1.60217733 \cdot 10^{-19} & h &\equiv 6.6260755 \cdot 10^{-34} \cdot \text{joule} \cdot \text{sec} & n_{\text{air}} &:= 1 \end{aligned}$$

### Equations to change wavelength to energy and vice versa

$$\lambda(\text{Energy}) := \frac{1.24 \cdot 10^3}{\left( \frac{\text{Energy}}{\text{eV}} \right)} \cdot \text{nm} \qquad E(\text{wavelength}) := \frac{1.24 \cdot 10^3}{\left( \frac{\text{wavelength}}{\text{nm}} \right)} \cdot \text{eV}$$

### **Program User Input Starts Here**

The bragg wavelength: desired wavelength of operation.

$$\text{data}_0 := \frac{\lambda_{\text{op}}}{\text{nm}}$$

$$\lambda_{1/4} := \frac{\lambda_{\text{op}}}{4} \qquad \lambda_{1/4} = 212.5 \cdot \text{nm} \quad \text{Free space quarter wavelength.}$$

$$E(\lambda_{\text{op}}) = 1.459 \cdot \text{eV} \quad \text{The energy equivalent of the desired wavelength.}$$

Refractive Index Calculation starts Here. All files use Aspnes and Adachi AlGaAs information

$$\text{known} := (0 \ 0 \ 0 \ 0.099 \ 0.099 \ .198 \ .198 \ .315 \ .315 \ .419 \ .419 \ .491 \ .491 \ .590 \ .590 \ .7 \ .7 \ .804 \ .804 \ 1.0 \ 1.0)^T$$

$$A := \text{READPRN}(\text{ALGAAS}) \quad n := 1.. \text{cols}(A) - 1 \qquad \text{cols}(\text{known}) = 1 \qquad \text{cols}(A) = 21$$

$$vx := A^{<0>} \quad vy^{<n>} := A^{<n>} \quad vs^{<n>} := \text{lspline}(vx, vy^{<n>}) \quad f(x, n) := \text{interp}(vs^{<n>}, vx, vy^{<n>}, x)$$

$N_{\text{sublayer}} := 19$  The number of sub-layers per layer

$data_1 := N_{\text{sublayer}}$

$N_{\text{cavity}} := 51$  The number of sublayers in the cavity stack

$data_2 := N_{\text{upper}}$

$data_3 := N_{\text{cavity}}$

$data_4 := N_{\text{lower}}$

$layers_{\text{period}} := 2 \cdot N_{\text{sublayer}} \quad layers_{\text{period}} = 38$

$z_{\text{period}} := 1 \dots layers_{\text{period}} \quad subs := layers_{\text{period}} + 1 \quad air := 0 \quad subs = 39$

The  $Al_xGa_{1-x}As$  refractive index information is imported from ALGAAS\_N.PRN, and was generated in another file. The  $Al_xGa_{1-x}As$  index information is taken from a paper by Adachi. Journal of Applied Physics, VOL. 58, No 3, 1 August 1985.

$j := 1 \dots 10$

$$kr_j := \text{known}_{2,j} \quad kr^T = \begin{array}{c|cccccccccccc} & 0 & 1 & 2 & 3 & 4 & 5 & 6 & 7 & 8 & 9 & 10 \\ \hline 0 & 0 & 0 & 0.099 & 0.198 & 0.315 & 0.419 & 0.491 & 0.59 & 0.7 & 0.804 & 1 \end{array}$$

$$\text{real}(E, X) := \sum_{n=1}^9 \left[ \left[ f(E, 2 \cdot n - 1) \cdot \left[ 1 - \left( \frac{X - kr_n}{kr_{n+1} - kr_n} \right) \right] + f(E, 2 \cdot n + 1) \cdot \left( \frac{X - kr_n}{kr_{n+1} - kr_n} \right) \right] \cdot (X \leq kr_{n+1}) \cdot (X > kr_n) \right]$$

$$\text{imag}(E, X) := \sum_{n=1}^9 \left[ \left[ f(E, 2 \cdot n) \cdot \left[ 1 - \left( \frac{X - kr_n}{kr_{n+1} - kr_n} \right) \right] + f(E, 2 \cdot n + 2) \cdot \left( \frac{X - kr_n}{kr_{n+1} - kr_n} \right) \right] \cdot (X \leq kr_{n+1}) \cdot (X > kr_n) \right]$$

$$n_{AlGaAs}(x, \lambda) := \text{real} \left( \frac{E(\lambda)}{eV}, x \right) - i \cdot \left| \text{imag} \left( \frac{E(\lambda)}{eV}, x \right) \right| \quad \text{Calculated complex refractive Index}$$

Refractive Index of low index layer

$$x_{\text{avg}} := \frac{x_{\text{lowindex}} + x_{\text{highindex}}}{2} \quad \text{Compositional average used in calculations} \quad x_{\text{avg}} = 0.575$$

$$x_{\text{diff}} := \left| \frac{x_{\text{lowindex}} - x_{\text{highindex}}}{2} \right| \quad \text{Compositional difference used in calculations}$$

Here I calculate the actual high and low indices for reference purposes

$$n_{\text{low}} := n_{AlGaAs}(x_{\text{lowindex}}, \lambda_{\text{op}}) \quad n_{\text{low}} = 3.001 - 3.379 \cdot 10^{-10}i \quad data_5 := n_{\text{low}}$$

$$n_{\text{low}} = 3.001 - 3.379 \cdot 10^{-10} i$$

$$n_{\text{high}} := n_{\text{AlGaAs}}(x_{\text{highindex}}, \lambda_{\text{op}}) \quad n_{\text{high}} = 3.502 - 0.003i$$

$$\text{data}_6 := n_{\text{high}} \quad n_{\text{high}} = 3.502 - 0.003i$$

My new approach is to use a different program for each type of grading scheme. I do not like unnecessary repetitiveness, however this will simplify computation and speed up development. This program deals exclusively with RAMP index profiles. See fig 1.

$\text{tri}(x) := \text{if}(|x| \leq 1, 1 - |x|, 0)$  Define tri function to use in calculation of period structure. p1 and p2 define the center points of the tri functions.

$$p1 := \text{ceil}(N_{\text{sublayer}}) \quad p1 = 19$$

$$p2 := 2 \cdot N_{\text{sublayer}}$$

$$\text{rhomb}(x) := \frac{\text{tri}(x) - \text{tri}(6 \cdot x) \cdot \frac{1}{6}}{\left(\frac{5}{6}\right)}$$

Composition of period.

$$x(z) := \left[ \text{rhomb}\left(\frac{z - p1}{N_{\text{sublayer}}}\right) \cdot (x_{\text{highindex}} - x_{\text{lowindex}}) \right] + x_{\text{lowindex}}$$

$$x_{\text{comp}_{z_{\text{period}}}} := x(z_{\text{period}})$$

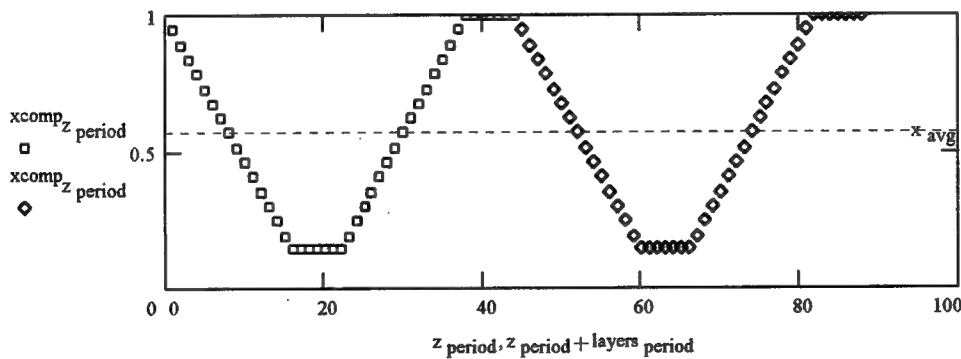
$$j := 39..44 \quad x_{\text{comp}_j} := x_{\text{lowindex}} \quad \text{layers}_{\text{period}} := \text{layers}_{\text{period}} + 6$$

$$\text{subs} := \text{layers}_{\text{period}} + 1$$

$$z_{\text{period}} := 1..44$$

$$n_{\text{comp}_{z_{\text{period}}}} := n_{\text{AlGaAs}}(x_{\text{comp}_{z_{\text{period}}}}, \lambda_{\text{op}})$$

$$N_{\text{sublayer}} := N_{\text{sublayer}} + 3$$



Now I will create the cavity profile using the same finite element method. I will assign each of the wells to a particular sublayer and put barrier material between them. I will then grade the cavity and ensure that the entire cavity comes out to measure the required number of half-wavelengths.

num := 2.0      number of half wavelengths across cavity, may be multiple of a half.

p3 defines the center of the cavity sublayers. I then use this to center the rhomb function in the cavity. The rhomb function is used to grade the filler region of the cavity. The quantum wells and barrier region are contained in the flat region on top.

$$p3 := \text{ceil}\left(\frac{N_{\text{cavity}}}{2}\right) \quad p3 = 26 \quad \text{rect}(x) := \text{if}\left(|x| \leq \frac{1}{2}, 1, 0\right) \quad \text{rhomb}(x) := \frac{\text{tri}(x) - \text{tri}(7 \cdot x) \cdot \frac{1}{7}}{\left(\frac{6}{7}\right)}$$

$$z_{\text{cav}} := 1..N_{\text{cavity}}$$

$$\text{num}_{\text{qw}} := 4 \quad \text{num}_{\text{barrier}} := 3 \quad \text{qw} := 0..\text{num}_{\text{qw}} - 1 \quad \text{bar} := 0..\text{num}_{\text{barrier}} - 1$$

$$x_{\text{qw}} := 0.0001 \quad x_{\text{bar}} := .15$$

$$x_{\text{cav}}(z) := \text{rhomb}\left(\frac{z - p3}{N_{\text{cavity}} \cdot \frac{1}{2}}\right) \cdot (x_{\text{highindex}} - x_{\text{lowindex}}) + x_{\text{lowindex}} \quad x_{\text{cavity}_z_{\text{cav}}} := x_{\text{cav}}(z_{\text{cav}})$$

$$x_{\text{cavity}_{23+2 \cdot \text{qw}}} := x_{\text{qw}} \quad x_{\text{highindex}} = 0.15$$

$$n_{\text{cavity}_z_{\text{cav}}} := n_{\text{AlGaAs}}(x_{\text{cavity}_z_{\text{cav}}}, \lambda_{\text{op}}) \quad n_{\text{qw}} := n_{\text{AlGaAs}}(x_{\text{qw}}, \lambda_{\text{op}})$$

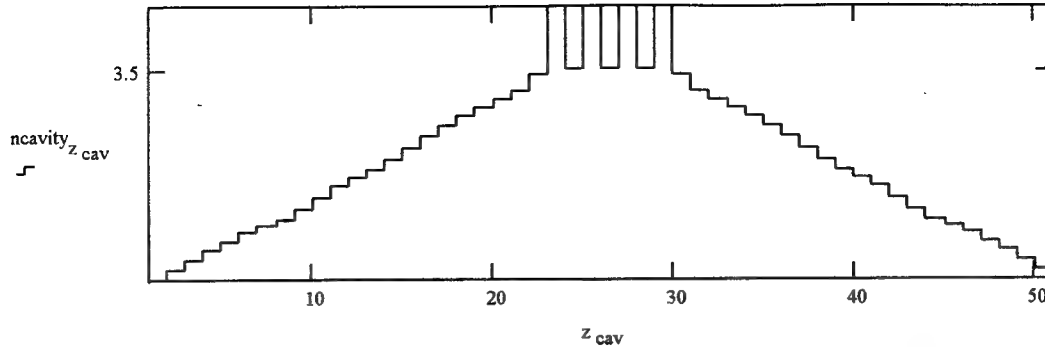
$$L_{\text{qw}} := 8 \cdot \text{nm} \quad \text{Barrier}_{\text{qw}} := 10 \cdot \text{nm}$$

The next equation accounts for linearly grading the cavity and calculates the sublayer thicknesses at the bragg wavelength

$$\text{cav}_{\text{step}} := \frac{\text{num} \cdot \frac{\lambda_{\text{op}}}{2} - \text{num}_{\text{qw}} \cdot L_{\text{qw}} \cdot \text{Re}(n_{\text{qw}}) - \text{num}_{\text{barrier}} \cdot \text{Barrier}_{\text{qw}} \cdot \text{Re}(n_{\text{high}})}{\sum \text{Re}(n_{\text{cavity}}) - \text{num}_{\text{qw}} \cdot \text{Re}(n_{\text{qw}}) - \text{num}_{\text{barrier}} \cdot \text{Re}(n_{\text{high}})} \quad \text{cav}_{\text{step}} = 44.001 \cdot \text{\AA}$$

$$\text{sublayer}_{\text{cavity}_z_{\text{cav}}} := \text{cav}_{\text{step}} \quad \text{sublayer}_{\text{cavity}_{24+2 \cdot \text{bar}}} := \text{Barrier}_{\text{qw}} \quad \text{sublayer}_{\text{cavity}_{23+2 \cdot \text{qw}}} := L_{\text{qw}}$$

$$\sum_{z_{\text{cav}}} \text{sublayer}_{\text{cavity}_z_{\text{cav}}} \cdot n_{\text{cavity}_z_{\text{cav}}} = 1 - 0.001i \cdot \left(\frac{\lambda_{\text{op}}}{2}\right) \cdot \text{num} \quad \text{A check to ensure that the cavity measures up to the proper number of half wavelengths.}$$



$$\text{dist}_{\text{low}} := \frac{\lambda_{\text{op}}}{4 \cdot \text{Re}(n_{\text{low}})} - 12 \cdot \text{nm}$$

$$\text{dist}_{\text{high}} := \frac{\lambda_{\text{op}}}{4 \cdot \text{Re}(n_{\text{high}})} - 12 \cdot \text{nm}$$

User input to decide how wide the plateaus of the indices should be. From all of my design drawings it is important to be able to specify this number and then calculate the inter-plateau distances.

$$\text{dist}_{\text{high}} = 48.674 \cdot \text{nm} \quad \text{dist}_{\text{low}} = 58.799 \cdot \text{nm}$$

$$a_{\text{step}} := \frac{\frac{\lambda_{\text{op}}}{2} - \text{Re}(n_{\text{high}}) \cdot \text{dist}_{\text{high}} - \text{Re}(n_{\text{low}}) \cdot \text{dist}_{\text{low}}}{\sum_{n=1}^{\text{layers}_{\text{period}}} \text{Re}(n_{\text{comp}})_n - 7 \cdot \text{Re}(n_{\text{low}}) - 7 \cdot \text{Re}(n_{\text{high}})}$$

The step size is determined by subtracting the optical distance (refractive index times physical distance) of the plateaus from the half wave layer. The remainder of course is what is left for grading.

$$a_{\text{step}} = 8.01729 \cdot \text{\AA}$$

Now I make the assignments of sublayer size based on the sizes  $\text{dist}_{\text{high}}$  and  $\text{dist}_{\text{low}}$ .

$$\text{sublayer}_{z_{\text{period}}} := a_{\text{step}}$$

$$p2 = 38$$

$$j := 0..6$$

$$\text{sublayer}_{16+j} := \frac{\text{dist}_{\text{high}}}{7}$$

$$\text{sublayer}_{p1} = 6.953 \cdot \text{nm}$$

$$x_{\text{comp}_{p1}} = 0.15$$

$$p1 = 19$$

$$p2 = 38$$

$$\text{sublayer}_{38+j} := \frac{\text{dist}_{\text{low}}}{7}$$

$$\text{sublayer}_{p2} = 8.4 \cdot \text{nm}$$

$$x_{\text{comp}_{p2}} = 1$$

Now that all the design considerations have been made, we may start the program.

Incident angle

$$\text{data}_7 := 0$$

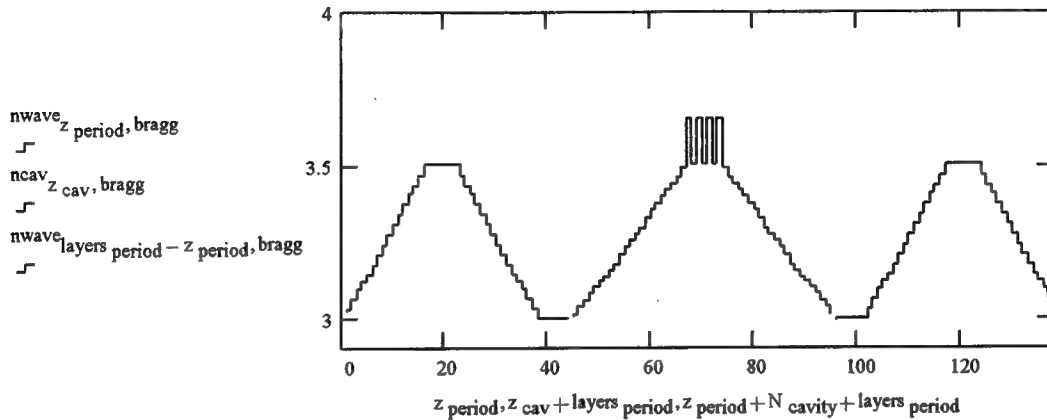
$$\text{ct} := 0.. \frac{\lambda_{\text{upper}} - \lambda_{\text{lower}}}{\text{SCALE} \cdot \text{nm}}$$

$$\lambda_{\text{ct}} := \lambda_{\text{lower}} + \text{ct} \cdot \text{nm} \cdot \text{SCALE}$$

$$\text{bragg} := \frac{\lambda_{\text{upper}} - \lambda_{\text{lower}}}{\text{nm} \cdot 2 \cdot \text{SCALE}} \quad \lambda_{\text{bragg}} = 850 \cdot \text{nm}$$

$$\text{nwave}_{z_{\text{period}}, \text{ct}} := n_{\text{AlGaAs}}(x_{\text{comp}_{z_{\text{period}}}, \text{ct}}, \lambda_{\text{ct}}) \quad \text{ncav}_{z_{\text{cav}}, \text{ct}} := n_{\text{AlGaAs}}(x_{\text{cavity}_{z_{\text{cav}}}, \text{ct}}, \lambda_{\text{ct}}) \quad \text{nwave}_{\text{air}, \text{ct}} := 1$$

$$\text{nwave} := \text{Re}(\text{nwave}) \quad \text{ncav} := \text{Re}(\text{ncav})$$



Polarization selection made here. 0 denotes a TM polarization, 1 denotes a TE polarization. I also give the general expression for intrinsic admittance of a layer.

$$\text{adm}(n) := \left[ \text{Re}(n)^2 - (|\text{Im}(n)|)^2 - n_{\text{air2}} \cdot \sin(\theta)^2 - 2 \cdot i \cdot \text{Re}(n) \cdot |\text{Im}(n)| \right]^{\frac{1}{2}} \quad \text{MacLeod page 37}$$

$$\text{Pol} := 1 \quad \text{data}_g := \text{Pol}$$

$$\eta_{\text{adm}}(n) := \text{if} \left[ \text{Pol} = 0, \frac{\mathcal{Y}(n)^2}{\text{adm}(n)}, \mathcal{Y}_{\text{adm}}(n) \right]$$

$$\text{nsubs}_{\text{ct}} := n_{\text{AlGaAs}}(0.001, \lambda_{\text{ct}}) \quad \text{Set substrate to GaAs} \quad \text{nsubs} := \text{Re}(\text{nsubs})$$

$$\theta_{\text{in}_{0, \text{ct}}} := \theta \quad \text{Vector of all incident angles per wavelength.}$$

$$\theta_{\text{trans}}(n_{\text{trans}}, n_{\text{in}}, \theta_{\text{in}}) := \text{asin} \left( \frac{\text{Re}(n_{\text{in}})}{\text{Re}(n_{\text{trans}})} \cdot \sin(\theta_{\text{in}}) \right)$$

Function linking angle incident from medium 1 to angle transmitted into medium 2.

$$\theta_{\text{in}_{z_{\text{period}}, \text{ct}}} := \theta_{\text{trans}}(\text{nwave}_{z_{\text{period}}, \text{ct}}, \text{nwave}_{z_{\text{period}} - 1, \text{ct}}, \theta_{\text{in}_{z_{\text{period}} - 1, \text{ct}}})$$

$$\theta_{\text{in}_{\text{subs}, \text{ct}}} := \theta_{\text{trans}}(\text{nwave}_{\text{layers period}, \text{ct}}, \text{nsubs}_{\text{ct}}, \theta_{\text{in}_{\text{layers period}, \text{ct}}})$$



$$\theta_{cav_{0,ct}} := \theta_{in_{layers\_period,ct}} \quad ncav_{0,ct} := n_{wave_{layers\_period,ct}}$$

$$\theta_{cav_{z_{cav,ct}}} := \theta_{trans}(ncav_{z_{cav,ct}}, ncav_{z_{cav-1,ct}}, \theta_{cav_{z_{cav-1,ct}}})$$

$$\delta_{delay}(n_{user}, d_{user}, \lambda_{user}) := \frac{2 \cdot \pi \cdot d_{user}}{\lambda_{user}} \cdot adm(n_{user})$$

Function describing phase delay  
per finite sublayer

$$\delta_{z\_period,ct} := \delta_{delay}(n_{wave_{z\_period,ct}}, sublayer_{z\_period}, \lambda_{ct})$$

Phase delay per sublayer.

$$\delta_{cav_{z_{cav,ct}}} := \delta_{delay}(ncav_{z_{cav,ct}}, sublayer_{cavity_{z_{cav}}}, \lambda_{ct})$$

$$\delta_{top_{ct}} := \delta_{delay}(n_{subs_{ct}}, 20 \text{ nm}, \lambda_{ct})$$

$$\frac{\frac{\lambda_{op}}{4}}{Re(n_{subs_{bragg}})} = 58.238 \cdot \text{nm}$$

This means the layers add up to  $\pi$  phase shifts, at the bragg wavelength for the periodic high - low layers.

$$\sum_{n=1}^{layers\_period} \delta_{n,bragg} = 1 - 3.737 \cdot 10^{-4} i \cdot \pi$$

$$\sum_{n=1}^{N_{cavity}} \delta_{cav_{n,bragg}} = 1.99931 - 0.00277 i \cdot \pi$$

Now I will take all of the previous information and create the Transfer matrix described by MacLeod in his book on thin film filters. First I will set up the parameters that I use in the calculation.

$$\eta_{air,ct} := \eta_{adm}(n_{wave_{air,ct}}) \quad \eta_{z\_period,ct} := \eta_{adm}(n_{wave_{z\_period,ct}})$$

$$\eta_{cav_{z_{cav,ct}}} := \eta_{adm}(ncav_{z_{cav,ct}}) \quad \eta_{subs,ct} := \eta_{adm}(n_{subs_{ct}}) \quad \eta_{top_{ct}} := \eta_{adm}(n_{subs_{ct}})$$

$$M(\delta, \eta) := \begin{bmatrix} \cos(\delta) & \frac{j \cdot \sin(\delta) \cdot \text{siemens}}{\eta} \\ \frac{j \cdot \eta \cdot \sin(\delta)}{\text{siemens}} & \cos(\delta) \end{bmatrix}$$

Characteristic Matrix of layer

$$NU := N_{upper} \quad NU = 6 \quad NL := N_{lower} \quad NL = 38 \quad LC := N_{cavity}$$

$$NS := N_{sublayer} \quad NS = 22 \quad LP := layers\_period \quad LP = 44 \quad LC = 51$$

$$Mupper(a) := M(\delta_{top,a}, \eta_{top,a}) \cdot \left( \prod_{k=17}^{LP} M(\delta_{k,a}, \eta_{k,a}) \right) \cdot \left( \prod_{k=1}^{LP} M(\delta_{k,a}, \eta_{k,a}) \right)^{NU-1}$$

$$Mlupper(a) := \left( \prod_{k=LP}^1 M(\delta_{k,a}, \eta_{k,a}) \right)^{NU-1} \cdot \left( \prod_{k=LP}^{17} M(\delta_{k,a}, \eta_{k,a}) \right) \cdot M(\delta_{top,a}, \eta_{top,a})$$

$$Mlower(a) := \left( \prod_{k=LP}^1 M(\delta_{k,a}, \eta_{k,a}) \right)^{NL} \cdot \left( \prod_{k=LP}^{23} M(\delta_{k,a}, \eta_{k,a}) \right)$$

$$Mcavity(b) := \left( \prod_{k=1}^{LC} M(\delta_{cav,k,b}, \eta_{cav,k,b}) \right)$$

Now we are at the final page where everything up to now is put together. I am using MacLeod notation throughout.

$$A_{mac\ ct}^{<>} := Mupper(ct) \cdot Mcavity(ct)^{onoff} \cdot Mlower(ct) \cdot \left[ \frac{1}{\frac{\eta_{subs,ct}}{siemens}} \right] \quad \text{calculates reflectance of RCLED}$$

$$A1_{mac\ ct}^{<>} := Mlower(ct) \cdot \left[ \frac{1}{\frac{\eta_{subs,ct}}{siemens}} \right] \quad \text{calculates reflectance of lower mirror}$$

$$A2_{mac\ ct}^{<>} := Mlupper(ct) \cdot \left[ \frac{1}{\frac{\eta_{air,ct}}{siemens}} \right] \quad \text{calculates reflectance of upper mirror from inside cavity}$$

$$A_{mac\ 2,ct} := \frac{\lambda_{lower}}{nm} + ct \cdot SCALE$$

$$B_{mac} := (A_{mac}^T)^{<0>} \quad B1_{mac} := (A1_{mac}^T)^{<0>} \quad B2_{mac} := (A2_{mac}^T)^{<0>}$$

$$C_{mac} := (A_{mac}^T)^{<1>} \cdot siemens \quad C1_{mac} := (A1_{mac}^T)^{<1>} \cdot siemens \quad C2_{mac} := (A2_{mac}^T)^{<1>} \cdot siemens$$

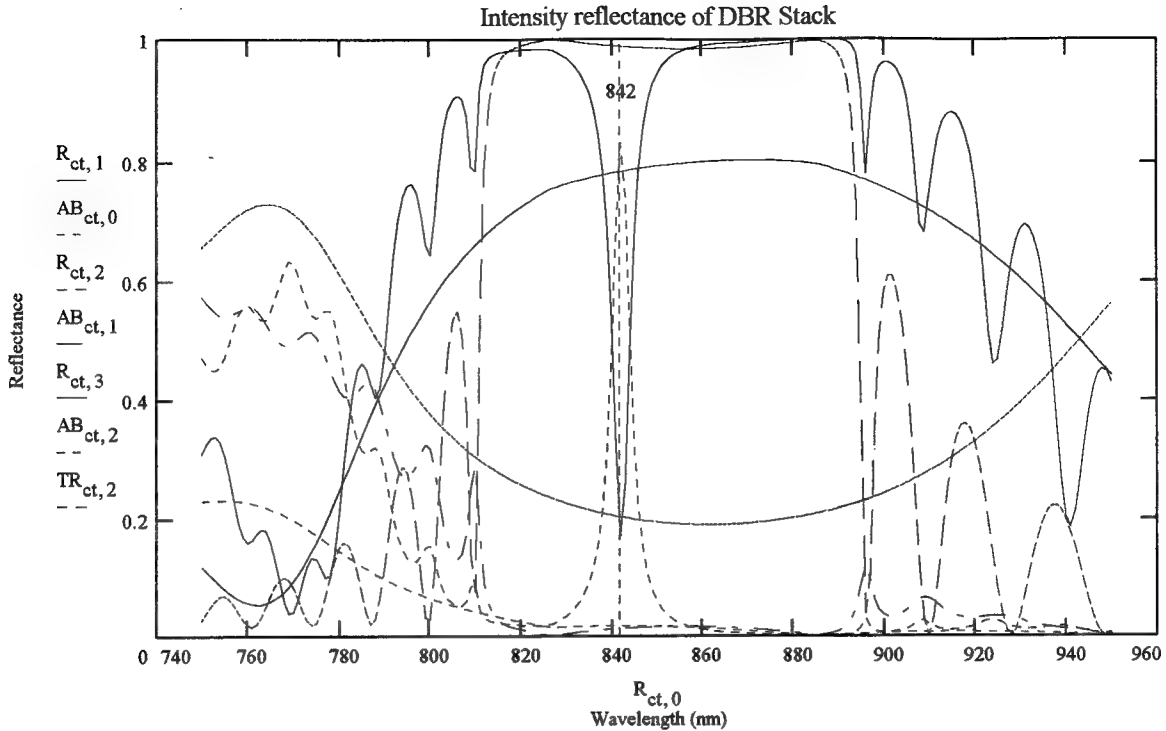
Assignations based on MacLeod notation.

$$\begin{aligned} \rho_{ct,0} &:= \frac{(\eta_{0,ct} \cdot B_{mac_{ct}} - C_{mac_{ct}})}{(\eta_{0,ct} \cdot B_{mac_{ct}} + C_{mac_{ct}})} & TR_{ct,0} &:= \frac{4 \cdot \eta_{0,ct} \cdot \text{Re}(\eta_{subs,ct})}{(\eta_{0,ct} \cdot B_{mac_{ct}} + C_{mac_{ct}}) \cdot (\eta_{0,ct} \cdot B_{mac_{ct}} + C_{mac_{ct}})} \\ \rho_{ct,1} &:= \frac{(\eta_{cav_{51,ct}} \cdot B1_{mac_{ct}} - C1_{mac_{ct}})}{(\eta_{cav_{51,ct}} \cdot B1_{mac_{ct}} + C1_{mac_{ct}})} & TR_{ct,1} &:= \frac{4 \cdot \eta_{cav_{51,ct}} \cdot \text{Re}(\eta_{subs,ct})}{(\eta_{cav_{51,ct}} \cdot B1_{mac_{ct}} + C1_{mac_{ct}}) \cdot (\eta_{cav_{51,ct}} \cdot B1_{mac_{ct}} + C1_{mac_{ct}})} \\ \rho_{ct,2} &:= \frac{(\eta_{cav_{1,ct}} \cdot B2_{mac_{ct}} - C2_{mac_{ct}})}{(\eta_{cav_{1,ct}} \cdot B2_{mac_{ct}} + C2_{mac_{ct}})} & TR_{ct,2} &:= \frac{4 \cdot \eta_{cav_{51,ct}} \cdot \text{Re}(\eta_{air,ct})}{(\eta_{cav_{1,ct}} \cdot B2_{mac_{ct}} + C2_{mac_{ct}}) \cdot (\eta_{cav_{1,ct}} \cdot B2_{mac_{ct}} + C2_{mac_{ct}})} \\ AB_{ct,0} &:= \frac{4 \cdot \eta_{0,ct} \cdot \text{Re}(B_{mac_{ct}} \cdot \overline{C_{mac_{ct}}} - \eta_{subs,ct})}{(\eta_{0,ct} \cdot B_{mac_{ct}} + C_{mac_{ct}}) \cdot (\eta_{0,ct} \cdot B_{mac_{ct}} + C_{mac_{ct}})} \\ AB_{ct,1} &:= \frac{4 \cdot \eta_{cav_{51,ct}} \cdot \text{Re}(B1_{mac_{ct}} \cdot \overline{C1_{mac_{ct}}} - \eta_{subs,ct})}{(\eta_{cav_{51,ct}} \cdot B1_{mac_{ct}} + C1_{mac_{ct}}) \cdot (\eta_{cav_{51,ct}} \cdot B1_{mac_{ct}} + C1_{mac_{ct}})} \\ AB_{ct,2} &:= \frac{4 \cdot \eta_{cav_{51,ct}} \cdot \text{Re}(B2_{mac_{ct}} \cdot \overline{C2_{mac_{ct}}} - \eta_{air,ct})}{(\eta_{cav_{1,ct}} \cdot B2_{mac_{ct}} + C2_{mac_{ct}}) \cdot (\eta_{cav_{1,ct}} \cdot B2_{mac_{ct}} + C2_{mac_{ct}})} \end{aligned}$$

Complex reflectivity of field derived by matrix method

Phase change upon reflection by DBR stack.

$$\begin{aligned} q := 0..2 \quad \phi_{ct,q} &:= (\text{angle}(\text{Re}(\rho_{ct,q}), \text{Im}(\rho_{ct,q}))) & R_{ct,q+1} &:= \text{Re}(\rho_{ct,q} \cdot \overline{\rho_{ct,q}}) \\ R_{ct,q+4} &:= \phi_{ct,q} & R_{ct,0} &:= A_{mac_{2,ct}} & j := 0..7 & R_{j,7} := data_j \\ R_{ct,8} &:= TR_{ct,2} \end{aligned}$$



Useful to have all user input parameters right here beside the graph

$\lambda_{\text{lower}} = 750 \cdot \text{nm}$      $\lambda_{\text{upper}} = 950 \cdot \text{nm}$     Range of wavelengths used by program    Pol = 1  
 SCALE = 1     $\lambda_{\text{op}} = 850 \cdot \text{nm}$   
 $\theta = 5 \cdot \text{deg}$      $N_{\text{upper}} = 6$      $N_{\text{lower}} = 38$     num = 2    onoff = 1  
 $x_{\text{lowindex}} = 1.0$     Composition of lowest index desired    WRITEPRN(Ref405) := R<sub>1</sub>  
 $x_{\text{highindex}} = 0.15$     Composition of highest index desired

The next step is to use the information previously calculated to determine the electric field intensity at each layer in the structure. The first thing to do is create the entire RCLED structure by stacking the matrices with index and phase information.

$$N_{\text{sublayer}} = 22 \quad \text{layers}_{\text{period}} = 44 \quad N_{\text{lower}} = 38 \quad N_{\text{upper}} = 6$$

$$N_{\text{cavity}} + N_{\text{sublayer}} = 73 \quad N_{\text{cavity}} = 51$$

$$l_t := \text{layers}_{\text{period}} \cdot N_{\text{upper}} + N_{\text{cavity}} + \text{layers}_{\text{period}} \cdot N_{\text{lower}}$$

$$l_t = 1.987 \cdot 10^3$$

$$l_1 := \text{layers}_{\text{period}} \cdot N_{\text{lower}} \quad l_1 = 1.672 \cdot 10^3$$

```

l_u := layers_period * N_upper      l_u = 264
l_c := N_cavity                     l_c = 51

rows(nwave) = 45      cols(nwave) = 201      rows(ncav) = 52      cols(ncav) = 201
z := 0..3

mak1 := 1..l_u      n_0,z := 1      choice := (bragg - 25  bragg  bragg - 8  bragg - 40)^T
                                                    bragg = 100

n_mak1,z := if(mod(mak1, layers_period) == 0, nwave_layers_period, choice_z, nwave_mod(mak1, layers_period), choice_z)

theta2_mak1 := if(mod(mak1, layers_period) == 0, theta_layers_period, choice, theta_mod(mak1, layers_period), choice)^0

sub_mak1 := if(mod(mak1, layers_period) == 0, sublayer_layers_period, sublayer_mod(mak1, layers_period))

mak2 := 1 + l_u.. N_cavity + l_u
theta2_mak2 := theta_cav_mod(mak2, l_u), choice - 2^0      n_mak2,z := ncav_mod(mak2, l_u), choice_z

sub_mak2 := sublayer_cavity_mod(mak2, l_u)      theta_0 := theta

mak3 := 1 + l_c + l_u.. l_t      rows(nwave) = 45      i := 1.. layers_period

nwave2_i,z := [nwave_<choice_z>]_layers_period + 1 - i      sub2_i := sublayer_layers_period + 1 - i
theta2_i := (theta_<choice - 2>)_layers_period + 1 - i^0
n_mak3,z := if(mod(mak3 - l_c, layers_period) == 0, nwave2_layers_period, z, nwave2_mod(mak3 - l_c, layers_period), z)

theta2_mak3 := if(mod(mak3 - l_c, layers_period) == 0, theta2_layers_period, theta2_mod(mak3 - l_c, layers_period))^0

sub_mak3 := if(mod(mak3 - l_c, layers_period) == 0, sub2_layers_period, sub2_mod(mak3 - l_c, layers_period))

rows(n) = 1.988 * 10^3      l_t = 1.987 * 10^3

```

Yeh method from "Optical Waves in layered Media"

$$D(n) := \text{if } \text{Pol} = 0, \frac{1}{n} \begin{pmatrix} \text{adm}(n) & \text{adm}(n) \\ 1 & -1 \end{pmatrix}, \begin{pmatrix} 1 & 1 \\ \text{adm}(n) & -\text{adm}(n) \end{pmatrix}$$

$$P(k_x, d) := \begin{pmatrix} e^{i \cdot k_x \cdot d} & 0 \\ 0 & e^{-i \cdot k_x \cdot d} \end{pmatrix} \quad k(n, \lambda) := \frac{2 \cdot \pi}{\lambda} \cdot (\text{adm}(n))$$

$$i := 0..1 \quad \text{count1} := 1_t - 2..0$$

$$\text{AMP}_{i, 1_t-1} := \begin{pmatrix} 0.001 \\ 0 \end{pmatrix}_i \cdot \frac{\text{volt}}{\text{m}} \quad \text{AMP1}_{i, 1_t-1} := \begin{pmatrix} 0.001 \\ 0 \end{pmatrix}_i \cdot \frac{\text{volt}}{\text{m}}$$

$$\text{use} := 0$$

$$\text{AMP}^{<\text{count1}>} := P[k[n_{\text{count1}, \text{use}}, \lambda(\text{choice}_{\text{use}})], \text{sub}_{\text{count1}}] \cdot D(n_{\text{count1}, \text{use}})^{-1} \cdot D(n_{\text{count1}+1, \text{use}}) \cdot \text{AMP}^{<\text{count1}+1>}$$

$$\text{AMP}^{<0>} := D(n_{0, \text{use}})^{-1} \cdot D(n_{1, \text{use}}) \cdot \text{AMP}^{<1>}$$

$$\text{use} := 2$$

$$\text{AMP1}^{<\text{count1}>} := P[k[n_{\text{count1}, \text{use}}, \lambda(\text{choice}_{\text{use}})], \text{sub}_{\text{count1}}] \cdot D(n_{\text{count1}, \text{use}})^{-1} \cdot D(n_{\text{count1}+1, \text{use}}) \cdot \text{AMP1}^{<\text{count1}+1>}$$

$$\text{AMP1}^{<0>} := D(n_{0, \text{use}})^{-1} \cdot D(n_{1, \text{use}}) \cdot \text{AMP1}^{<1>}$$

$$\text{choice}^T = (75 \ 100 \ 92 \ 60)$$

$$z_{\text{total}} := 1..1_t - 1$$

Calculated E-Fields

$$E_{z_{\text{total}}} := \text{AMP}_{0, z_{\text{total}}} + \text{AMP1}_{1, z_{\text{total}}}$$

$$E1_{z_{\text{total}}} := \text{AMP1}_{0, z_{\text{total}}} + \text{AMP1}_{1, z_{\text{total}}}$$

$$\text{thick}_{z_{\text{total}}} := \text{Re} \left[ \sum_{q=z_{\text{total}}}^{1_t-1} \text{sub}_q \right]$$

Use to reference each sublayer to thickness

$$\text{Intensity}_{z_{\text{total}}, 0} := \frac{1}{2} \cdot n_{z_{\text{total}}, 0} \cdot \Re(E_{z_{\text{total}}} \cdot \overline{E_{z_{\text{total}}}}) \quad \max(\text{Intensity}) = 5.829 \cdot 10^{-5} \cdot \frac{\text{watt}}{\text{m}^2}$$

$$\text{Intensity}_{z_{\text{total}},1} := \frac{1}{2} \cdot n_{z_{\text{total}},3} \cdot \Re \left( E_{1z_{\text{total}}} \cdot \overline{E_{1z_{\text{total}}}} \right) \quad \max(\text{Intensity}^{<1>}) = 3.385 \cdot 10^{-4} \cdot \frac{\text{watt}}{\text{m}^2}$$

$$\text{norm}_f := \max(\text{Intensity})$$

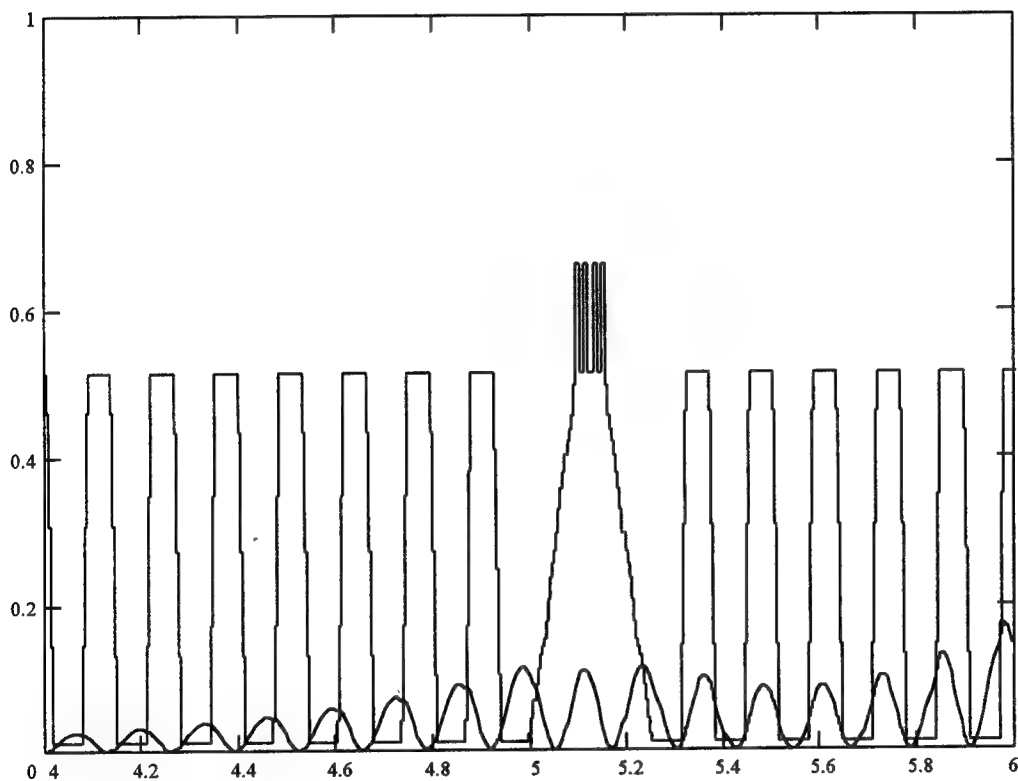
$$V1 := \Re \left( \frac{\overrightarrow{\text{Intensity}}}{\text{norm}_f} \right) \quad \text{use} = 2$$

$$\text{norm}_I := \max(n)$$

$$V2_{z_{\text{total}},0} := n_{z_{\text{total}},\text{use} - 3}$$

$$V2_{z_{\text{total}},1} := n_{z_{\text{total}},0 - 3}$$

WRITEPRN(ELEC5) := OUT<sub>0</sub>



## Appendix C. Quantum Well Energy Level and Gain Calculations

This document calculates the energy levels of rectangular quantum wells in bulk material. The quantum wells are finite and have the confinement energy defined as  $V_0$ .

$$\begin{aligned}
 k_B &= 1.380658 \cdot 10^{-23} \frac{\text{joule}}{\text{K}} & \text{eV} &= \text{joule} \cdot 1.60217733 \cdot 10^{-19} & \text{nm} &= \text{m} \cdot 10^{-9} & \mu\text{m} &= \text{m} \cdot 10^{-6} \\
 \hbar &= \frac{6.6260755 \cdot 10^{-34}}{2 \cdot \pi} \frac{\text{sec}}{\text{joule}} & h &:= \hbar \cdot 2 \cdot \pi & \lambda(E) &:= h \cdot \frac{c}{E} & \epsilon_0 &= 8.854187817 \cdot 10^{-12} \frac{\text{farad}}{\text{m}} \\
 q_e &= 1.60217733 \cdot 10^{-19} \cdot \text{coul} & m_e &= 9.1093897 \cdot 10^{-31} \cdot \text{kg} & c &= 299792458 \cdot \frac{\text{m}}{\text{sec}}
 \end{aligned}$$

The preamble defines all the terms that will be used in the document. User entered parameters follow:

$$\begin{aligned}
 m_{re}(x) &:= 0.067 + 0.083 \cdot x & \text{Relative mass of electron as function of composition } x. \\
 m_{rlh}(x) &:= 0.087 + 0.063 \cdot x & \text{Relative mass of light hole as function of composition } x. \\
 m_{rhh}(x) &:= 0.62 + 0.14 \cdot x & \text{Relative mass of heavy hole as function of composition } x. \\
 x_{\text{well}} &:= 0.0 & \text{Composition factor of Quantum well. Used to calculate conduction and valence band energies} \\
 x_{\text{cav}} &:= 0.15 & \text{Composition factor of cavity} \\
 L &:= 8 \cdot \text{nm} & \text{Thickness of Quantum well in nanometers} \\
 m_{e \text{ well}} &:= m_{re}(x_{\text{well}}) \cdot m_e & \text{Mass of electron inside quantum well} & m_{e \text{ well}} &= 0.067 \cdot m_e \\
 m_{e \text{ cav}} &:= m_{re}(x_{\text{cav}}) \cdot m_e & \text{Mass of electron outside quantum well} & m_{e \text{ cav}} &= 0.079 \cdot m_e \\
 m_{hh \text{ well}} &:= m_{rhh}(x_{\text{well}}) \cdot m_e & \text{Mass of heavy hole inside quantum well} & m_{hh \text{ well}} &= 0.62 \cdot m_e \\
 m_{hh \text{ cav}} &:= m_{rhh}(x_{\text{cav}}) \cdot m_e & \text{Mass of heavy hole outside quantum well} & m_{hh \text{ cav}} &= 0.641 \cdot m_e \\
 m_{lh \text{ well}} &:= m_{rlh}(x_{\text{well}}) \cdot m_e & \text{Mass of light hole inside quantum well} & m_{lh \text{ well}} &= 0.087 \cdot m_e \\
 m_{lh \text{ cav}} &:= m_{rlh}(x_{\text{cav}}) \cdot m_e & \text{Mass of light hole outside quantum well} & m_{lh \text{ cav}} &= 0.096 \cdot m_e
 \end{aligned}$$

For  $\text{Al}_x\text{Ga}_{1-x}\text{As}$



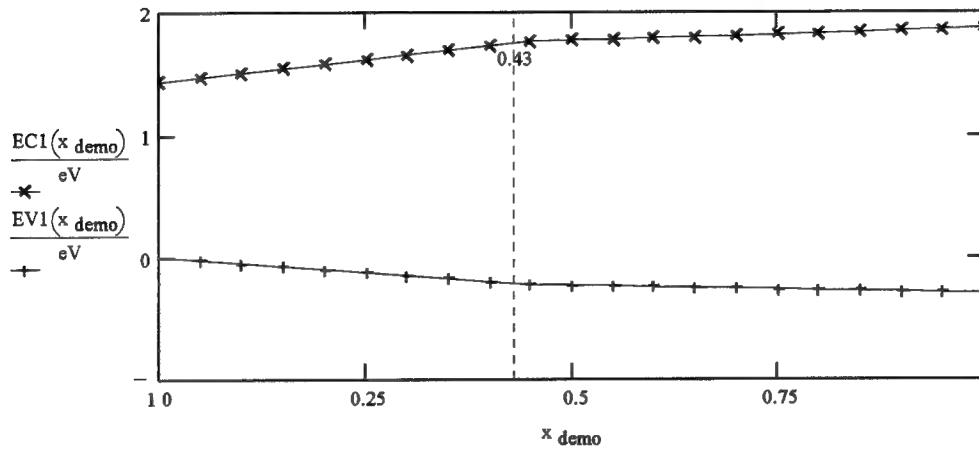
$$E_g(x) := \text{if}(x \leq 0.45, 1.424 + 1.247 \cdot x, 1.9 + 0.125 \cdot x + 0.143 \cdot x^2) \cdot \text{eV}$$

$$EC1(x) := E_g(0) + 0.6 \cdot (E_g(x) - E_g(0)) \quad EV1(x) := -0.4 \cdot (E_g(x) - E_g(0))$$

Used method of Bour to come up with following graph

$$x_{\text{demo}} := 0, 0.05..1 \quad \text{Range used to create a sample graph}$$

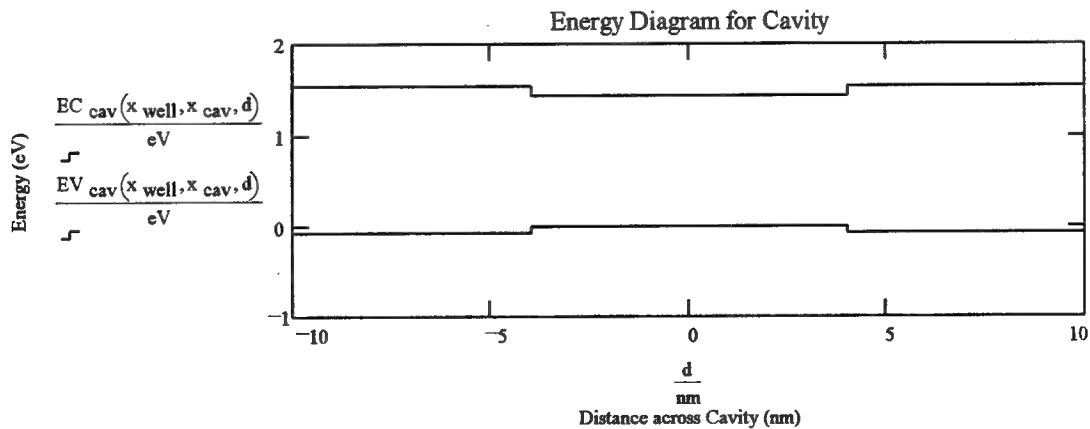
The composition range where the conduction band energy (referenced to the 0 composition zero point) is rising is where the semiconductor is a direct bandgap type. k conservation rules apply here.



I will now define the characteristics of the quantum well using the input parameters above. From the compositional fractions of the well and cavity I will create an energy diagram for the cavity. I am using  $\text{Al}_x\text{Ga}_{1-x}\text{As}$  as the cavity and well material.

$$EC_{\text{cav}}(x1, x2, d) := \text{if}\left(|d| \leq \frac{L}{2}, EC1(x1), EC1(x2)\right) \quad EV_{\text{cav}}(x1, x2, d) := \text{if}\left(|d| \leq \frac{L}{2}, EV1(x1), EV1(x2)\right)$$

$$d := -10 \cdot \text{nm}, -9.91 \cdot \text{nm}..10 \cdot \text{nm}$$



$V_o$  is defined as the difference between the energies of the conduction bands between the quantum well and the cavity.  $V_o$  is zero referenced to the top of the conduction band of the well material. There are three  $V_o$ s defined. One for electron energy levels in the conduction band of the quantum well, and two for the lh and hh energy levels in the valence band.

$$\begin{aligned} V_{o_0} &:= EC1(x_{cav}) - EC1(x_{well}) \quad EC1(x_{cav}) = 1.536 \cdot eV \quad EC1(x_{well}) = 1.424 \cdot eV \\ V_{o_1} &:= EV1(x_{well}) - EV1(x_{cav}) \\ V_{o_2} &:= EV1(x_{well}) - EV1(x_{cav}) \quad V_o^T = (0.112 \quad 0.075 \quad 0.075) \cdot eV \end{aligned}$$

$k_o$  is a constant used in the calculation process. It simplifies the bookkeeping by wrapping up a lot of other numbers into one. It has units of inverse meters.

$$k_{o_0} := \sqrt{\frac{2 \cdot me_{well} \cdot |V_{o_0}|}{\hbar^2 \cdot me_{cav}}} \quad k_{o_1} := \sqrt{\frac{2 \cdot mhh_{well} \cdot |V_{o_1}|}{\hbar^2 \cdot mhh_{cav}}} \quad k_{o_2} := \sqrt{\frac{2 \cdot mlh_{well} \cdot |V_{o_2}|}{\hbar^2 \cdot mlh_{cav}}}$$

$$k_o^T = (0.408 \quad 1.085 \quad 0.393) \cdot nm^{-1}$$

Now I use the secant method to solve the transcendental equation posed by the electron energy levels inside the quantum well. The equation is highlighted and explained in the book by Weisbuch.

$$y1(x) := x \cdot \tan(x) \quad y2(x) := x \cdot \cot(x) \quad y3(x, r) := \sqrt{r^2 - x^2}$$

$$f(x, r) := y1(x) - y3(x, r) \quad g(x, r) := y2(x) + y3(x, r)$$

Because the equation has different forms depending upon whether you are looking for an even or odd quantum level, I must ensure that Mathcad knows which condition to apply.  $r$  is a tidy constant to wrap things up a little and help the form of the equation.  $r$  is dimensionless.

$$r_0 := k_{o_0} \cdot \frac{L}{2} \cdot \frac{me_{well}}{me_{cav}} \quad r_1 := k_{o_1} \cdot \frac{L}{2} \cdot \frac{mhh_{well}}{mhh_{cav}} \quad r_2 := k_{o_2} \cdot \frac{L}{2} \cdot \frac{mlh_{well}}{mlh_{cav}}$$

$$r^T = (1.376 \quad 4.199 \quad 1.416)$$

From  $r$  we get the number of allowed energy levels in the quantum well. Once we know how many we have to solve for, it becomes easier to find them.

$$sol := 1 + \text{floor}\left(\frac{r}{\frac{\pi}{2}}\right) \quad sol = \begin{pmatrix} 1 \\ 3 \\ 1 \end{pmatrix}$$

Now I apply the secant method to solve the equation. I know that there are sol roots so I set the root counter n from 0 to sol -1. The secant method requires two initial guesses. These may be varied as necessary.

	Initial Guess 1	Initial Guess 2
$n := 0..sol_0 - 1$	$xc_{n,0} := \frac{\pi}{2.2} + n \cdot \frac{\pi}{2}$	$xc_{n,1} := \frac{\pi}{2.7} + n \cdot \frac{\pi}{2}$
$q := 0..sol_1 - 1$	$xv_{q,0} := \frac{\pi}{2.2} + q \cdot \frac{\pi}{2}$	$xv_{q,1} := \frac{\pi}{2.7} + q \cdot \frac{\pi}{2}$
$p := 0..sol_2 - 1$	$xvl_{p,0} := \frac{\pi}{2.2} + p \cdot \frac{\pi}{2}$	$xvl_{p,1} := \frac{\pi}{2.7} + p \cdot \frac{\pi}{2}$

N denotes how many iterations to use to converge to a solution. My initial guesses already comprise the first two solution "slots".

$$N := 12 \quad i := 2..N$$

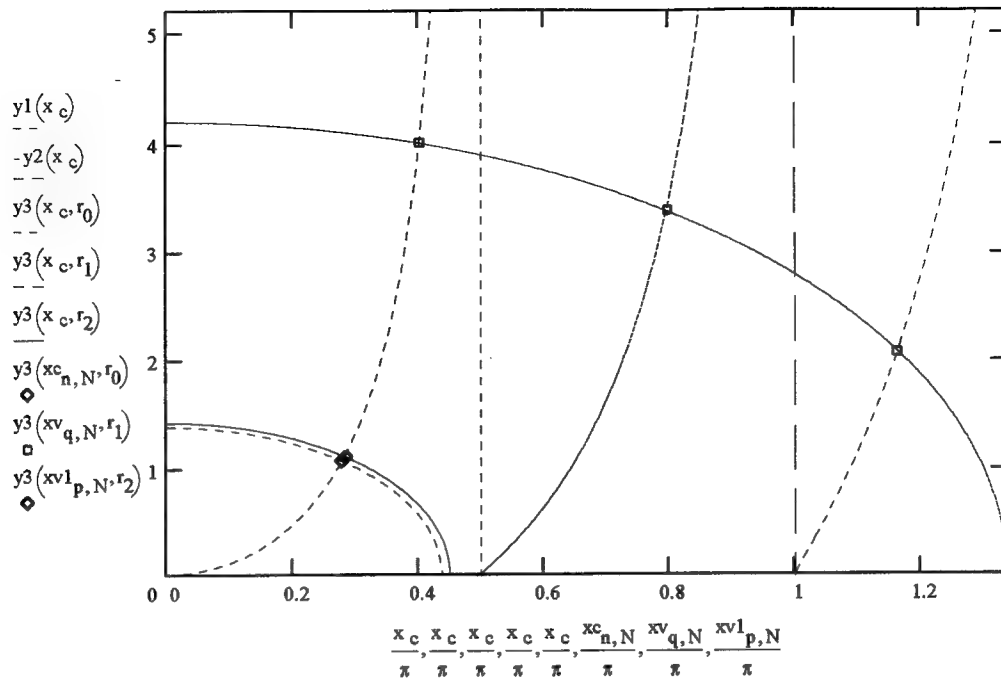
The solution variables change depending upon whether an odd or even solution is being sought. The odd or even solutions to the wave function represent cos or sin wave functions across the well. (Ref Weisbuch)

$$f(x1, x2, r, n) := \left| \text{if} \left( \text{mod}(n, 2) = 0, x1 - \frac{f(x1, r) \cdot (x1 - x2)}{f(x1, r) - f(x2, r)}, x1 - \frac{g(x1, r) \cdot (x1 - x2)}{g(x1, r) - g(x2, r)} \right) \right|$$

$xc_{n,i} := f(xc_{n,i-1}, xc_{n,i-2}, r_0, n)$	Electron Solution	$xc_{\langle N \rangle}^T = 0.878$
$xv_{q,i} := f(xv_{q,i-1}, xv_{q,i-2}, r_1, q)$	Heavy hole solution	$xv_{\langle N \rangle}^T = (1.265 \quad 2.503 \quad 3.656)$
$xvl_{p,i} := f(xvl_{p,i-1}, xvl_{p,i-2}, r_2, p)$	Light hole solution	$xvl_{\langle N \rangle}^T = 0.891$

The following graph plots the calculated points at the intersections of the transcendental equations.

$$x_c := 0.01, 0.02 \dots \max(r)$$



The answer derived before is of the form  $x = kL/2$ . To get the allowed  $k$  from this solution I must use:

$$k_c := \left| \overline{x_c}^{<N>} \right| \cdot \frac{2}{L} \quad k_c^T = 0.22 \cdot \text{nm}^{-1} \quad \text{Electron allowed wavenumbers}$$

$$k_v := \left| \overline{x_v}^{<N>} \right| \cdot \frac{2}{L} \quad k_v^T = (0.316 \quad 0.626 \quad 0.914) \text{nm}^{-1} \quad \text{Heavy hole allowed wavenumbers}$$

$$k_{vl} := \left| \overline{x_{vl}}^{<N>} \right| \cdot \frac{2}{L} \quad k_{vl}^T = 0.223 \cdot \text{nm}^{-1} \quad \text{Light hole allowed wavenumbers}$$

The relationship between  $k$  and Energy for particles is not linear but is related by the particle's momentum  $p$ . The relationship is given by (for the quantum well).

$$E_{K_{\text{well}}}(k, V_o, m_{\text{well}}) := \left( \frac{\hbar^2 \cdot k^2}{2 \cdot m_{\text{well}}} \right)$$

Now I put the  $k$  solutions back into the energy- $k$  equation and solve for the allowed energies. I will then reference them back to the original zero reference defined by Lott.

$$\begin{aligned} EC_{\text{allow}_n} &:= EK_{\text{well}}(kc_n, V_{o_0}, me_{\text{well}}) & EC_{\text{allow}}^T &= 0.027 \cdot \text{eV} \\ EV_{\text{allow}_q} &:= EK_{\text{well}}(kv_q, V_{o_1}, mhh_{\text{well}}) & EV_{\text{allow}}^T &= (0.006 \ 0.024 \ 0.051) \cdot \text{eV} \\ EV1_{\text{allow}_p} &:= EK_{\text{well}}(kv1_p, V_{o_2}, mlh_{\text{well}}) & EV1_{\text{allow}}^T &= 0.022 \cdot \text{eV} \end{aligned}$$

Now I reference these back to the original energy levels

$$\begin{aligned} EC_{\text{orig}} &:= EC1(x_{\text{well}}) + EC_{\text{allow}} & EC_{\text{orig}}^T &= 1.451 \cdot \text{eV} \\ EV_{\text{orig}} &:= EV1(x_{\text{well}}) - EV_{\text{allow}} & EV_{\text{orig}}^T &= (-0.006 \ -0.024 \ -0.051) \cdot \text{eV} \\ EV1_{\text{orig}} &:= EV1(x_{\text{well}}) - EV1_{\text{allow}} & EV1_{\text{orig}}^T &= -0.022 \cdot \text{eV} \\ EVT_{\text{orig}} &:= \text{stack}\left(\frac{EV_{\text{orig}}}{\text{eV}}, \frac{EV1_{\text{orig}}}{\text{eV}}\right) \cdot \text{eV} & EVT_{\text{orig}}^T &= (-0.006 \ -0.024 \ -0.051 \ -0.022) \cdot \text{eV} \end{aligned}$$

Now I have to define the transition energies that are possible. This basically means finding the difference in energy level between every electron level and heavy-hole, light hole level.

$$s := 0..(sol_1 + sol_2) - 1$$

$$E_{\text{trans}_{n,s}} := EC_{\text{orig}_n} - EVT_{\text{orig}_s}$$

$$E_{\text{trans}} = (1.458 \ 1.475 \ 1.503 \ 1.473) \cdot \text{eV}$$

$$E\lambda(E) := \frac{1.24}{E \text{ eV}} \cdot \mu\text{m} \quad \lambda_{\text{trans}} := E\lambda(E_{\text{trans}})$$

$$\lambda_{\text{trans}} = (850.731 \ 840.401 \ 825.151 \ 841.739) \cdot \text{nm} \quad \text{Transition Wavelengths}$$

Now I will apply what I have already done to the Chinn model to calculate the gain and spontaneous emission for a cavity with no mirrors.

$$M = (|M|)^2 \quad \text{From Chinn and Lott notation, this is transition matrix}$$

$$E_g := EC1(x_{\text{well}}) - EV1(x_{\text{well}}) \quad E_g = 1.424 \cdot \text{eV}$$

$$\Delta_o(x) := (0.34 - 0.04 \cdot x) \cdot \text{eV} \quad \Delta_o(0) = 0.34 \cdot \text{eV}$$

$$M := \frac{m_e^2 \cdot E_g \cdot (E_g + \Delta_o(x_{\text{well}}))}{12 \cdot m_{\text{well}} \cdot \left( E_g + 2 \cdot \frac{\Delta_o(x_{\text{well}})}{3} \right)} \quad M = 1.893 \cdot eV \cdot m_e \quad \text{Transition Element Matrix}$$

$$\text{reduced\_mass}(m_1, m_2) := (m_1^{-1} + m_2^{-1})^{-1}$$

$$m_{\text{electron}_n} := m_{\text{well}} \quad m_{\text{electron}}^T = 0.067 \cdot m_e \quad \text{Reduced mass electron}$$

$$m_{\text{hhole}_q} := m_{\text{hh\_well}} \quad m_{\text{hhole}}^T = (0.62 \ 0.62 \ 0.62) \cdot m_e \quad \text{Reduced mass heavy hole}$$

$$m_{\text{hole}_p} := m_{\text{lh\_well}} \quad m_{\text{hole}}^T = 0.087 \cdot m_e \quad \text{Reduced mass light hole}$$

$$m_{\text{hole}} := \text{stack} \left( \frac{m_{\text{hhole}}}{m_e}, \frac{m_{\text{hole}}}{m_e} \right) \cdot m_e \quad m_{\text{hole}}^T = (0.62 \ 0.62 \ 0.62 \ 0.087) \cdot m_e$$

$$m_{\text{trans1}_{n,q}} := \text{reduced\_mass}(m_{\text{electron}_n}, m_{\text{hhole}_q}) \quad m_{\text{trans1}} = (0.06 \ 0.06 \ 0.06) \cdot m_e$$

$$m_{\text{trans2}_{n,p}} := \text{reduced\_mass}(m_{\text{electron}_n}, m_{\text{hole}_p}) \quad m_{\text{trans2}} = 0.038 \cdot m_e$$

$$m_{\text{trans}} := \text{augment}(m_{\text{trans1}}, m_{\text{trans2}})$$

Now that I have defined all of my transition energies and reduced interaction masses, I will define the selection rules. I am initially enforcing rigorous k-selection. Only transitions between like quantum states are allowed. That is, 1 - 1, 2 - 2, etc.

$$C1_{n,q} := \text{if}(n=q, 1, 0) \quad C1 = (1 \ 0 \ 0) \quad \text{C matrix for electron - heavy hole transitions}$$

$$C2_{n,p} := \text{if}(n=p, 0, 0) \quad C2 = 0 \quad \text{C matrix for electron - light hole transitions, however we are only considering electron-heavy hole interactions, therefore this parameter is always zero}$$

$$C := \text{augment}(C1, C2) \quad C = (1 \ 0 \ 0 \ 0) \quad \text{Complete C selection matrix}$$

$$A(E1, E2) := \frac{3}{4} \cdot \left( 1 + \frac{E1}{E2} \right) \quad \text{Anisotropy factor for the transitions, considering only TE radiation for the electron - heavy hole transition}$$

$$f_{\text{cv}}(E, E_f, T) := \frac{1}{\exp \left( \frac{E - E_f}{k_b \cdot T} \right) + 1} \quad \text{Fermi population factor}$$

$$f_{cv}(E, E_f, T) := \frac{1}{\exp\left(\frac{E - E_f}{k_b \cdot T}\right) + 1} \quad \text{Fermi population factor}$$

$H(y) := \text{if}(y \geq 0, 1, 0)$  Heaviside Step Function used to define allowed energy transitions

First I must find the quasi Fermi levels for the concentrations and temperature specified

$$T := 300 \cdot K \quad E_f := 1.4605 \cdot \text{eV} \quad \text{carrier} := (1 \ 1.5 \ 2.0 \ 2.5 \ 3.0 \ 3.5) \cdot T \cdot 10^{18}$$

$$EC_{\text{orig}}^T = 1.451 \cdot \text{eV}$$

Assuming Charge Neutrality  $q := 0..5$

$$\text{CONC}_{\text{electron}}(E_{fc}) := \log \left[ \frac{k_b \cdot T}{hbar^2 \cdot \pi \cdot L} \cdot \sum_n m_{\text{electron}_n} \cdot \ln \left[ 1 + \exp \left[ -\frac{(EC_{\text{orig}_n} - E_{fc})}{k_b \cdot T} \right] \right] \right] \cdot \text{cm}^3$$

$$\text{CONC}_{\text{hole}}(E_{fv}) := \log \left[ \frac{k_b \cdot T}{hbar^2 \cdot \pi \cdot L} \cdot \sum_n m_{\text{hole}_n} \cdot \ln \left[ 1 + \exp \left[ -\frac{(E_{fv} - EVT_{\text{orig}_n})}{k_b \cdot T} \right] \right] \right] \cdot \text{cm}^3 \quad \text{TOL} = 10^{-12}$$

$$\text{conc}_{\text{electron}} := \overrightarrow{\log(\text{carrier})} \quad \text{conc}_{\text{hole}} := \overrightarrow{\log(\text{carrier})}$$

$$\text{guess}_{fc} := 1.51 \cdot \text{eV} \quad \text{guess}_{fv} := 0.001 \cdot \text{eV} \quad \Delta E_g := -3 \cdot 10^{-8} \cdot \text{eV} \cdot \text{carrier}^{\frac{1}{3}}$$

$$E_{fc_q} := \text{root}(\text{CONC}_{\text{electron}}(\text{guess}_{fc}) - \text{conc}_{\text{electron}_q}, \text{guess}_{fc})$$

$$E_{fv_q} := \text{root}(\text{CONC}_{\text{hole}}(\text{guess}_{fv}) - \text{conc}_{\text{hole}_q}, \text{guess}_{fv})$$

$$E_e(E1, m1, m2) := EC1(x_{\text{well}}) + (E1 - E_g) \cdot \frac{m1}{m2} \quad \text{Conduction band energies}$$

$$E_h(E1, m1, m2) := EV1(x_{\text{well}}) - (E1 - E_g) \cdot \frac{m1}{m2} \quad \text{Valence band energies}$$

Finally, put it all together for the gain spectrum.

$$\text{con} := \frac{q \cdot c2 \cdot M}{\epsilon_0 \cdot m_{e2} \cdot c \cdot hbar \cdot 3.6 \cdot L} \quad \text{Constant defined for calculations} \quad \text{con} = 1.06 \cdot 10^{18} \cdot \text{m} \cdot \text{sec}^{-2}$$

$$E_{\text{transl}_q} := E_{\text{trans}_{0,0}} + \Delta E_{g_q}$$

$$E_{\text{transl}}^T = (1.428 \quad 1.423 \quad 1.42 \quad 1.417 \quad 1.414 \quad 1.412) \cdot \text{eV}$$

Fermi Inversion Factor given by

$$f_g(E, z) := f_{\text{cv}}\left(E_e\left(E, m_{\text{trans}_{0,0}}, m_{\text{electron}_0}\right), E_{f_z}, T\right) - f_{\text{cv}}\left(E_h\left(E, m_{\text{trans}_{0,0}}, m_{\text{hole}_0}\right), E_{f_z}, T\right)$$

Probability of Emission given by

$$f_e(E, z) := f_{\text{cv}}\left(E_e\left(E, m_{\text{trans}_{0,0}}, m_{\text{electron}_0}\right), E_{f_z}, T\right) \cdot \left(1 - f_{\text{cv}}\left(E_h\left(E, m_{\text{trans}_{0,0}}, m_{\text{hole}_0}\right), E_{f_z}, T\right)\right)$$

Gain spectrum given by:

$$g(E, z) := \frac{1}{E} \cdot \text{con} \cdot m_{\text{trans}_{0,0}} \cdot A\left(E, E_{\text{transl}_z}\right) \cdot f_g(E, z) \cdot H\left(E - E_{\text{transl}_z}\right)$$

Now convolve the calculated gain with the Lorentzian to account for intra-band scattering

$$i := 0..1023 \quad E_{\text{test}_i} := 1 \cdot \text{eV} + i \cdot 0.002 \cdot \text{eV}$$

$$j := 0..1023 \quad \tau_c := 10^{-13} \cdot \text{sec} \quad \text{Number from Corzine (Zory: Quantum Well Lasers) accounts for Lorentzian broadening}$$

$$g_{\text{test}_{i,q}} := g\left(E_{\text{test}_i}, q\right)$$

$$\text{lor}(E) := \frac{1}{\pi} \cdot \frac{\frac{\hbar}{\tau_c}}{\left(E - \frac{\max(E_{\text{test}}) + 1 \cdot \text{eV}}{2}\right)^2 + \left(\frac{\hbar}{\tau_c}\right)^2} \quad \text{Lorentzian used for intra-band scattering}$$

$$k := 0..511$$

$$\text{Lor}_i := \text{lor}\left(E_{\text{test}_i}\right) \cdot \text{eV} \quad \text{Lor}_1 := \text{Lor} \quad \text{Lor}_k := \text{Lor}_{512+k} \quad \text{Lor}_{512+k} := \text{Lor}_k$$

Now normalize convolved spectra to original spectra and print

$$G_{\text{test}}^{<q>} := \text{ifft}\left(\overline{\left(\text{fft}(\text{Lor}) \cdot \text{fft}(g_{\text{test}}^{<q>})\right)}\right) \quad G_{\text{test}}^{<q>} := G_{\text{test}}^{<q>} \cdot \frac{\sum g_{\text{test}}^{<q>}}{\sum G_{\text{test}}^{<q>}}$$



Energy Normalization done here to make  
sure Lorentzian adds no energy to system

$\sum g_{ltest} \langle q \rangle$

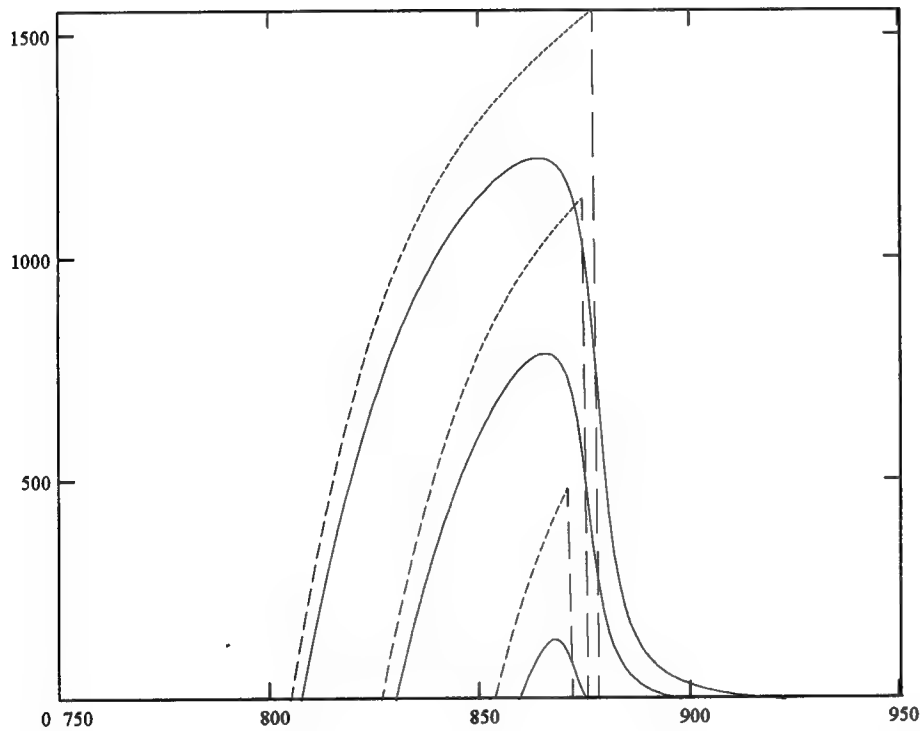
$-2.419 \cdot 10^8 \cdot m^{-1}$
$-2.353 \cdot 10^8 \cdot m^{-1}$
$-2.288 \cdot 10^8 \cdot m^{-1}$
$-2.225 \cdot 10^8 \cdot m^{-1}$
$-2.162 \cdot 10^8 \cdot m^{-1}$
$-2.099 \cdot 10^8 \cdot m^{-1}$

$\sum G_{test} \langle q \rangle$

$-3.764 \cdot 10^9 \cdot m^{-1}$
$-3.662 \cdot 10^9 \cdot m^{-1}$
$-3.561 \cdot 10^9 \cdot m^{-1}$
$-3.462 \cdot 10^9 \cdot m^{-1}$
$-3.364 \cdot 10^9 \cdot m^{-1}$
$-3.267 \cdot 10^9 \cdot m^{-1}$

$\sum G_{ltest} \langle q \rangle$

$-2.419 \cdot 10^8 \cdot m^{-1}$
$-2.353 \cdot 10^8 \cdot m^{-1}$
$-2.288 \cdot 10^8 \cdot m^{-1}$
$-2.225 \cdot 10^8 \cdot m^{-1}$
$-2.162 \cdot 10^8 \cdot m^{-1}$
$-2.099 \cdot 10^8 \cdot m^{-1}$



Now I will calculate the spontaneous emission spectrum for the architecture in question.

$$\text{con1} := \frac{3.6 \cdot q_{c2} \cdot M}{\epsilon_0 \cdot m_{e2} \cdot c^3 \cdot hbar^4 \cdot L}$$

$$R(E, z) := \text{con1} \cdot E \cdot \left( m_{\text{trans}_{0,0}} \cdot f_e(E, z) \cdot H(E - E_{\text{trans}_{l_z}}) \right) \text{psec} := \text{sec} \cdot 10^{-15}$$

Again convolve with Lorentzian and normalize

$$Rs_{i,q} := R(E_{test_i}, q) \quad G2test^{<q>} := \text{iff}(\overline{(\text{fft}(\text{Lor}) \cdot \text{fft}(Rs^{<q>})))} \quad R1test^{<q>} := G2test^{<q>} \cdot \frac{\sum Rs^{<q>}}{\sum G2test^{<q>}}$$

$\sum Rs^{<q>}$

$5.291 \cdot 10^{54} \cdot \text{kg}^{-1} \cdot \text{m}^{-5} \cdot \text{sec}$
$1.086 \cdot 10^{55} \cdot \text{kg}^{-1} \cdot \text{m}^{-5} \cdot \text{sec}$
$1.785 \cdot 10^{55} \cdot \text{kg}^{-1} \cdot \text{m}^{-5} \cdot \text{sec}$
$2.556 \cdot 10^{55} \cdot \text{kg}^{-1} \cdot \text{m}^{-5} \cdot \text{sec}$
$3.414 \cdot 10^{55} \cdot \text{kg}^{-1} \cdot \text{m}^{-5} \cdot \text{sec}$
$4.35 \cdot 10^{55} \cdot \text{kg}^{-1} \cdot \text{m}^{-5} \cdot \text{sec}$

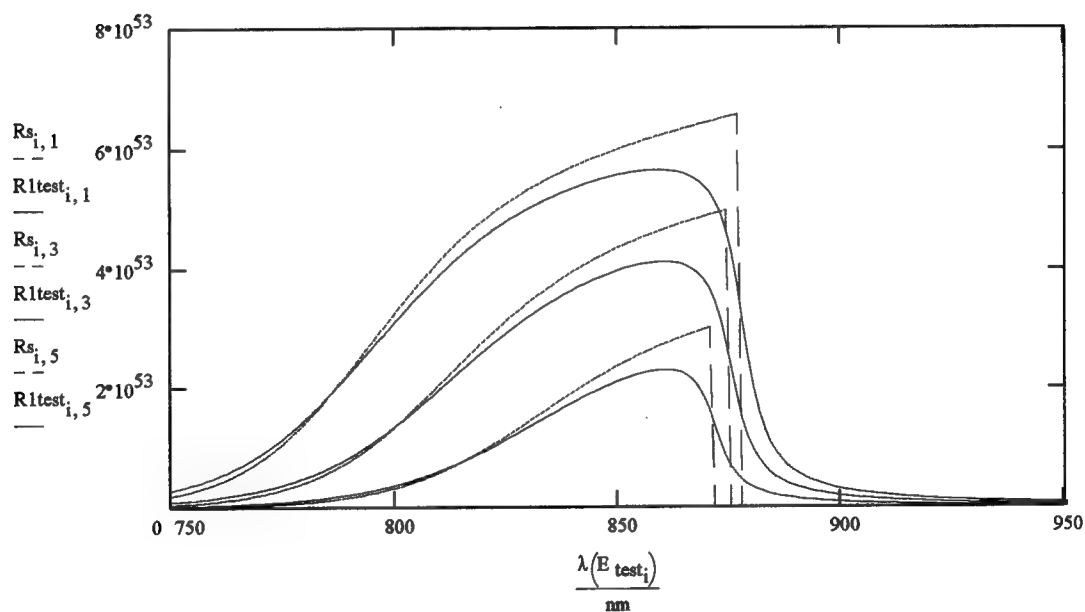
$\sum G2test^{<q>}$

$8.234 \cdot 10^{55} \cdot \text{kg}^{-1} \cdot \text{m}^{-5} \cdot \text{sec}$
$1.69 \cdot 10^{56} \cdot \text{kg}^{-1} \cdot \text{m}^{-5} \cdot \text{sec}$
$2.778 \cdot 10^{56} \cdot \text{kg}^{-1} \cdot \text{m}^{-5} \cdot \text{sec}$
$3.977 \cdot 10^{56} \cdot \text{kg}^{-1} \cdot \text{m}^{-5} \cdot \text{sec}$
$5.313 \cdot 10^{56} \cdot \text{kg}^{-1} \cdot \text{m}^{-5} \cdot \text{sec}$
$6.77 \cdot 10^{56} \cdot \text{kg}^{-1} \cdot \text{m}^{-5} \cdot \text{sec}$

$\sum R1test^{<q>}$

$5.291 \cdot 10^{54} \cdot \text{kg}^{-1} \cdot \text{m}^{-5} \cdot \text{sec}$
$1.086 \cdot 10^{55} \cdot \text{kg}^{-1} \cdot \text{m}^{-5} \cdot \text{sec}$
$1.785 \cdot 10^{55} \cdot \text{kg}^{-1} \cdot \text{m}^{-5} \cdot \text{sec}$
$2.556 \cdot 10^{55} \cdot \text{kg}^{-1} \cdot \text{m}^{-5} \cdot \text{sec}$
$3.414 \cdot 10^{55} \cdot \text{kg}^{-1} \cdot \text{m}^{-5} \cdot \text{sec}$
$4.35 \cdot 10^{55} \cdot \text{kg}^{-1} \cdot \text{m}^{-5} \cdot \text{sec}$

$$\text{carrier}^T = (1 \quad 1.5 \quad 2 \quad 2.5 \quad 3 \quad 3.5) \cdot 10^{18}$$



Next few lines output data to file

$$\text{result}_{i,0} := \frac{\lambda(E_{\text{test}_i})}{\text{nm}}$$

$\text{result}_{i,1} := R1 \text{test}_{i,1} \cdot \text{eV} \cdot \text{cm}^3 \cdot \text{psec}$	$\text{carrier} = 2.5 \times 10^{18}$
$\text{result}_{i,2} := R1 \text{test}_{i,2} \cdot \text{eV} \cdot \text{cm}^3 \cdot \text{psec}$	$\text{carrier} = 3.0 \times 10^{18}$
$\text{result}_{i,3} := R1 \text{test}_{i,3} \cdot \text{eV} \cdot \text{cm}^3 \cdot \text{psec}$	$\text{carrier} = 3.5 \times 10^{18}$
$\text{result}_{i,4} := R1 \text{test}_{i,4} \cdot \text{eV} \cdot \text{cm}^3 \cdot \text{psec}$	$\text{carrier} = 3.0 \times 10^{18}$
$\text{result}_{i,5} := R1 \text{test}_{i,5} \cdot \text{eV} \cdot \text{cm}^3 \cdot \text{psec}$	$\text{carrier} = 4.5 \times 10^{18}$

Put write equation on toggle, so it only writes when you want it to.

$\text{WRITEPRN}(\text{rspon}) := \text{Re}(\text{result})$

## Bibliography

1. Craford, M.G. "LEDs Challenge the Incandescents," *IEEE Spectrum*: 24-29 (September 1992).
2. Gunshor, R.L., N. Otsuka, A.V. Nurmikko. "Blue Lasers on the Horizon," *IEEE Spectrum*: 28-33 (May 1993).
3. Keller, U., G.R. Jacobovitz-Veselka, J.E. Cunningham, W.Y. Yan, B. Tell, and K.F. Brown-Goebeler. "Microcavity Enhanced Vertical-Cavity Light-Emitting Diodes," *Applied Physics Letters*, **62**(24): 3085-3087 (14 June 1993).
4. Werner, K. "Higher Visibility for LEDs," *IEEE Spectrum*: 30-39 (July 1994).
5. Schubert, E.F., Y.-H. Wang, A.Y. Cho, L.-W. Tu, and G.J. Zydzik. "Resonant Cavity Light-Emitting Diode," *Applied Physics Letters*, **60**(8): 921-923 (14 June 1993).
6. Purcell, E.M. *Physics Review*, **69**: 681 (1946).
7. De Martini, F., G. Innocenti, G. R. Jacobovitz, , and P. Mataloni. "Anomalous Spontaneous Emission Time in a Microscopic Optical Cavity," *Physical Review Letters*, **59**: 2955-2958 (28 December 1987).
8. Björk, G. "Modification of Spontaneous Emission Rate in Planar Dielectric Microcavity Structures," *Physical Review A*, **44**: 669-681 (1 July 1991).
9. Lei, C., D. G. Deppe, Z. Huang, and C. C. Lin. "Emission Characteristics From Dipoles With Fixed Positions in Fabry Perot Cavities," *IEEE Journal of Quantum Electronics*, **29**: 1383-1386 (May 1993).
10. Macleod H. A. *Thin-Film Optical Filters*. New York: McGraw Hill Publishing Company, 1989.
11. Drummond, T. J., P. L. Gourley, and T. E. Zipperian. "Quantum-Tailored Solid-State Devices," *IEEE Spectrum*: 33-37 (June 1988).
12. Lei, C., T.J. Rogers, D.G. Deppe, and B.G. Streetman. "ZnSe/CaF<sub>2</sub> Quarter-Wave Bragg Reflector for the Vertical-Cavity Surface-Emitting Laser," *Journal Of Applied Physics*, **69**(11): 7430-7434 (1 June 1991).
13. Kojima, K., R.A. Morgan, T. Mullaly, G.D. Guth, M.W. Focht, R.E. Leibenguth, and M.T. Asom. "Reduction of p-Doped Mirror Electrical Resistance of GaAs/AlGaAs Vertical-Cavity Surface-Emitting Lasers By Delta-Doping," *Electronics Letters*, **29**: 1771-1772 (30 September 1993).
14. Hunt, N. E. J., E. F. Schubert, R. F. Kopf, D. L. Sivco, A. Y. Cho, and G. J. Zydzik. "Increased Fiber Communications Bandwidth from a Resonant Cavity Light-Emitting Diode Emitting at  $\lambda = 940$  nm," *Applied Physics Letters*, **63**(19): 2600-2602 (8 November 1993).

15. Lott, J. A. *Visible Vertical Cavity Surface Emitting Lasers*. PhD dissertation. The University of New Mexico, Albuquerque NM, 1993.
16. Chinn, S. R., P. S. Zory, and A. R. Reisinger. "A Model for GRIN-SCH-SQW Diode Lasers," *IEEE Journal of Quantum Electronics*, **24**: 2191-2214 (November 1988).
17. Lott, J. A., R. P. Schneider Jr., G. A. Vawter, J. C. Zolper, and K. J. Malloy. "Visible (660nm) Resonant Cavity Light-Emitting Diodes," *Electronics Letters*, **29**: 328-329 (18 February 1993).
18. Bae, J. W., and H. Temkin. "Photocurrent Spectroscopy of Bragg Mirrors in Vertical Cavity Surface Emitting Lasers," *Applied Physics Letters*, **64**(4): 400-402 (24 January 1994).
19. Weisbuch, C., and B. Vinter. *Quantum Semiconductor Structures: Fundamentals and Applications*. Academic Press, Boston, 1991.
20. Yeh, Pochi. *Optical Waves In Layered Media*. New York: Wiley Interscience, 1988.
21. Adachi, S. "Refractive Index of  $\text{Al}_x\text{Ga}_{1-x}\text{As}$  Alloys," *Journal Of Applied Physics*, **58**(3): 478-480 (1 August 1985).
22. Aspnes, D. E., S. M. Kelso, R. A. Logan, and R. Bhat. "Optical Properties of  $\text{Al}_x\text{Ga}_{1-x}\text{As}$ ," *Journal of Applied Physics*, **60**(2): 754-767 (15 July 1986).
23. Hecht, E. *Optics, 2nd ed.* Massachusetts: Addison Wesley Publishing Company, 1987.
24. Born, B., and E. Wolf. *Principles of Optics, 6th ed.* New York: Pergamon Press, 1980.
25. Verdeyen, J.T. *Laser Electronics*. New Jersey: Prentice-Hall Inc, 1989.
26. Babic, D.I. and S.W. Corzine. "Analytic Expressions for the Reflection Delay, Penetration Depth, and Absorptance of Quarter-Wave Dielectric Mirrors," *IEEE Journal of Quantum Electronics*, **28**: 514-524 (February 1991).
27. Nishikawa, T., T. Kakimura, Y. Lee, and M. Yamanishi. "Enhanced Transfer Efficiency in AlGaAs asymmetric Planar Microcavities," *Applied Physics Letters*, **65**(14): 1796-1798 (3 October 1994).
28. Saleh, B.E.A. and M.C. Teich. *Fundamentals of Photonics*. New York: Wiley Interscience, 1991.
29. Drummond, T. J., P. L. Gourley, and T. E. Zipperian. "Quantum-Tailored Solid-State Devices," *IEEE Spectrum*: 33-37 (June 1988).
30. Gunshor, R. L., N. Otsuka, and A. V. Nurmikko. "Blue Lasers on the Horizon," *IEEE Spectrum*: 28-33 (May 1993).

31. Corzine, S. W., R.-H. Yan, and L. A. Coldren. "Optical Gain in III-V Bulk and Quantum Well Semiconductors," *Quantum Well Lasers, Edited by P. S. Zory*: 17-96. San Diego CA: Academic Press, Inc, 1993.
32. Corzine, S. W., R. S. Geels, J. W. Scott, R.-H. Yan, and L. A. Coldren. "Design of Fabry-Perot Surface-Emitting Lasers with a Periodic Gain Structure," *IEEE Journal of Quantum Electronics*, **25(6)**: 1513-1524 (June 1989).
33. Blondelle, J., H. De Neve, P. Demeester, P. Van Daele, G. Borghs, and R. Baets. "6% External Quantum Efficiency From InGaAs/(Al)GaAs Single Quantum Well Planar Microcavity LEDs," *Electronics Letters*, **30**: 1787-1789 (13 October 1994).
34. Björk G. "On The Spontaneous Lifetime Change In An Ideal Planar Microcavity - Transition From A Mode Continuum to Quantized Modes," *IEEE Journal of Quantum Electronics*, **30(10)**: 2314-2318 (October 1994).

## *Vita*

Captain Thomas M. Fitzgerald was born on 19 April 1967 in Sacramento, California. He graduated from St. Joseph's Christian Brothers School (CBS), Thurles, County Tipperary, Ireland in 1984. He received a 4-year Air Force Reserve Officer Training Corps (AFROTC) scholarship and attended Manhattan College, Riverdale NY. He graduated Magna Cum Laude with a Bachelor's degree in Electrical Engineering (B.E.E) in 1988. Captain Fitzgerald's first assignment was to serve as a Flight Test Engineer on the AC-130U Gunship as a member of the 6518th Test Squadron at Edwards AFB CA. In December 1991 he was reassigned to Gunter AFB, AL, as a Command and Control Computer Communications Engineer working on the Global Command and Control System (GCCS). His primary duty was the initial design and testing of the worldwide Air Force GCCS. Captain Fitzgerald started AFIT in May 1993.

Captain Fitzgerald is a member of the Tau Beta Pi engineering Society.

### Permanent Address:

3526 Apple Grove Drive

Beavercreek OH 45430